PUB 93 - 113
RALT-170

The Polarisation Of The Tau Lepton Measured From Its Decays Into Two And Three Pion Final States.

Anil Patel B.Sc.(Hons.)

University Of Lancaster

May 1993.

This thesis is submitted in partial fulfilment of the degree of Ph.D. at the University of Lancaster. No part of it has been, or will be, submitted to any other University.

Dedicated to my parents and my family.

Acknowledgments.

This thesis would not have been possible without the help of many people , whom I wish to thank.

My first thanks must go to Professors Arthur Clegg and Terry Sloan for offering me the studentship at Lancaster University. I would like to thank the Science and Engineering Research Council (SERC) for funding the first three years of my work.

Without any data to analyse there would be no thesis, so I would like to thank my colleagues in the ALEPH collaboration and CERN for providing the data and allowing the use of their facilities during my stay there.

I would like to acknowledge the help of many people in the Lancaster HEP department for helping me throughout this undertaking; especially Professor Terry Sloan (my supervisor) for his guidance and concern and Dr Gareth Hughes for his saint-like patience. Many thanks also to Dr Steve Snow who helped me through my analysis and also to Dr's Nigel Keemer and Alex Finch. A big 'ta very much' to Dr Mark Nuttall for paving the way for us Aleph students at Lancaster. (I took you up on your offer!).

My Parents deserve more than a simple thank you for their love and support in everything that I have done.

Of the numerous people in my family, I would like to thank my Uncle and Aunty (Manumama and Champamami) in Preston for providing me with somewhere to stay during the final few months of writing this thesis.

The Polarisation Of The Tau Lepton Measured From Its Decays Into Two And Three Pion Final States.

Anil Patel B.Sc.(Hons.)

May 1993.

Abstract

The average longitudinal polarisation of the tau lepton has been measured from its decays into two and three pion final states, (dominated by the $\rho(770)$ and $a_1(1260)$ resonances respectively).

Approximately 20 pb^{-1} of data collected by the Aleph collaboration up to the end of data taking in 1991 has been analysed. Samples of 4593 $\tau \rightarrow \rho\nu_\tau$ and 2129 $\tau \rightarrow a_1\nu_\tau$ candidates were identified, which were subsequently used for the polarisation measurement. The values obtained were P_τ = -0.098 $\pm$ 0.048 and P_τ = -0.010 $\pm$ 0.175 from the rho and a_1 samples respectively. From these results, the effective weak mixing angle $sin^2\bar{\theta}_W$ of the Standard Electroweak Model has been measured giving values for the ratio of vector to axial vector couplings.

Also studied in this thesis is the polar dependence of the tau polarisation using the $\tau \rightarrow \rho\nu_\tau$ sample. This has resulted in a polarisation value of P_τ = -0.079 $\pm$ 0.036.

All the findings are consistent with the Standard Electroweak Model.

Contents

List of Figures

List of Tables

Chapter 1

Elementary Particle Physics.

1.1 Introduction.

The subject of Elementary Particle Physics aims to determine the ultimate constituents of matter and their interactions. The current theoretical understanding of the processes involved is embodied in what is known as *The Standard Model.* In recent years a lot of effort has been directed towards testing these theoretical ideas experimentally, resulting in the construction of larger and larger acceleration systems to reach the subnuclear dimensions necessary. The largest of these accelerators to date, LEP (see section 2.1) has allowed many stringent tests of the Standard Model to be made.

This thesis describes one such test of the model via a measurement of the average longitudinal polarisation of the tau lepton. The present chapter outlines the Standard Model concentrating on the electroweak aspects relevant to the analysis. The following chapter describes the experimental apparatus used for data collection. Event selection is described in chapter 4 and the methods used for the final measurements are detailed in chapter 5. This is followed by a study of the systematic uncertainties in chapter 6. The thesis ends with a discussion of the implications of the measurements.

1.2 The Standard Model

The model is based on the idea that symmetries of nature give rise to forces. These forces are mediated between particles by quanta known as gauge bosons. The properties of the bosons can be predicted by requiring the theory to be invariant under various transformations, (this is a reasonable requirement as otherwise the theory would consist of an infinite number of arbitrary parameters and nothing could be predicted!) .

Three of the four known forces in nature, i.e. the electromagnetic, the weak nuclear, and the strong nuclear can all be described by quantum field theories. Gravity remains difficult to describe by such methods, but at the scale of the subnuclear interactions its effects are completely negligible.

The current classification of fundamental particles is summarised in table 1.1.

The 'matter' particles sub-divide into *quarks* and *leptons*. Quarks have never been observed as free particles, they are always manifested as bound states. The only two possibilities existing are *baryons*, (a combination of three quarks, or three anti-quarks, but never a combination of quark and anti-quark), and *mesons*, (a quark and anti-quark pair). Rotational or translational/vibrational relative motion of the bound state quark systems gives rise to resonances such as the rho meson, (e.g. $\rho^+ \equiv \pi^+\pi^0 \equiv (u\bar{d})(u\bar{d} \pm d\bar{u})$), with definite quantum numbers and obeying specific selection rules [1].

Quarks interact via all of the three forces listed in table 1.1. However, this is not the case for leptons. These are divided into charged, (electron (e), muon (μ), and tau (τ)) and neutral (ν_e, ν_μ, and ν_τ neutrinos) particles. The charged leptons interact via both the electromagnetic and the weak nuclear forces, but the neutrinos only interact via the weak nuclear force. Also, only 'left-handed' neutrinos (i.e. longitudunally polarised with J_z = -1/2) are observed in nature, whereas the charged leptons can have either left- or right- handed polarisations.

Not listed in table 1.1 but which also exist are the 'matter ' anti-particles, which have identical masses and spins to the corresponding particles, but opposite charges, fermionic quantum numbers and magnetic moments.

In field theory each of the particles in table 1.1 represent the quanta of the

'MATTER' PARTICLES : spin 1/2 Fermions			
Quarks :	u (up)	c (charm)	(t) (top)
	d (down)	s (strange)	b (bottom)
Leptons :	ν_e	ν_μ	ν_τ
	e^-	μ^-	τ^-
	(electron)	(muon)	(tau)

'FORCE' PARTICLES : spin 1 Bosons		
Force mediated :	Particle :	
Electromagnetic	Photon	γ
Weak Nuclear	Charged vector boson.	$W^\pm$
	Neutral vector boson.	Z^0
Strong Nuclear	Gluons	g_i (i=1,..,8)

Table 1.1: Elementary particles within the Standard Model. Also in this model are fermionic anti-particles (not listed). The top quark is yet to be discovered and evidence for the tau neutrino is only indirect.

corresponding particle field. Not all of the particles listed in table 1.1 are present as stable forms making up matter as seen. Thus, it is more meaningful to think of fundamental fields rather than particles.

1.3 Field Theory.

The ideas of classical Lagrangian Mechanics (where the equations of motion of a discrete system can be formulated from considering the relative amounts of kinetic and potential energy i.e. the Lagrangian, [2] of the system), can be readily extended to systems with continuously varying coordinates $\phi(x,t)$ (i.e. *fields*), where the fields themselves at each point in space are the dynamical variables. The classical lagrangian becomes

$$L(q_i, \dot{q}_i, t) \rightarrow \mathcal{L}\left(\phi, \frac{\partial \phi}{\partial x_\mu}, x_\mu\right) \tag{1.1}$$

where q_i are the generalised coordinates for a discrete classical system of i particles, with $\dot{q}_i = dq_i/dt$, and the field ϕ is a function of the continuous parameters, $x_\mu \equiv (t, x)$. In terms of these four-vectors the theory can be made manifestly relativistic.

The Euler-Lagrange equations become

$$\frac{\partial}{\partial x_\mu}\left(\frac{\partial \mathcal{L}}{\partial(\partial\phi/\partial x_\mu)}\right) - \frac{\partial \mathcal{L}}{\partial \phi} = 0 \tag{1.2}$$

These are the equations of motion of the fields. Here $\mathcal{L}$ is the *lagrangian density*, such that

$$L = \int \mathcal{L} d^3x \tag{1.3}$$

where the integration is over all space and time. (In the rest of this thesis, a common convention will be adopted and $\mathcal{L}$ itself will be refered to as the lagrangian.)

Quantisation of this (still classical!) theory proceeds via the introduction of the Hamiltonian (representing the total energy of the system) and generalised momentum conjugate variables to the generalised coordinates, ϕ. The field $\phi(t, x)$ still has an infinite number of degrees of freedom. Thus, it is in the first instance analysed in terms of discrete cells of equal volume δx and then ultimately extended to the continuum limit. This naturally leads to the introduction of the lagrangian density and a Hamiltonian density. Interpretation of the generalised coordinates of the discrete approximation as quantum mechanical operators and subjecting them to commutation relations then yields a quantised field theory.

1.4 Gauge Invariance and Conserved Quantities.

For any theory to be useful it must be capable of predicting phenomena which can be verified experimentally. This of course requires the theory to be invariant under transformations. In the discussions which follow it will become apparent how imposing such an invariance (i.e. symmetry) leads to the conservation of various quantities (and conservation laws). These ideas are best studied within the framework of lagrangian field theory, where a correct lagrangian formulation leads to the equations of motion of the fields.

1.4.1 Global Gauge Invariance.

The Dirac equation follows from substituting the lagrangian

$$\mathcal{L} = i\bar{\psi}\gamma_\mu\partial^\mu\psi - m\bar{\psi}\psi \tag{1.4}$$

into the Euler-Lagrange equation 1.2. Here ∂^μ is the differential operator, γ_μ are the Dirac gamma matrices [3], and ψ is a complex field representing any fermion. This lagrangian thus describes spin 1/2 particles such as the electron. It is trivial to show that this lagrangian is invariant under the global transformation

$$\psi(x) \rightarrow e^{i\alpha}\psi(x) \tag{1.5}$$

(note, this is a global transformation since the phase factor α is independent of x).

A closer examination in terms of an infinitesimal transformation, i.e.

$$\psi(x) \rightarrow (1 + i\alpha)\psi(x) \tag{1.6}$$

followed by the requirement $\delta\mathcal{L} = 0$, reveals a conserved current of the form

$$\partial_\mu j^\mu = 0 \tag{1.7}$$

where

$$j^\mu = \frac{ie}{2}\left(\frac{\partial\mathcal{L}}{\partial(\partial_\mu\psi)}\psi - \bar{\psi}\frac{\partial\mathcal{L}}{\partial(\partial_\mu\bar{\psi})}\right) \tag{1.8}$$

$$= -e\bar{\psi}\gamma^\mu\psi \tag{1.9}$$

and 2α has been identified with the charge of an electron, e by choice. Then from equation 1.7 it immediately follows that

$$Q = \int j^0 d^3x \tag{1.10}$$

(the total charge), must be a conserved quantity, directly because of the required global invariance.

The group of all transformations $U(\alpha) \equiv e^{i\alpha}$ i.e. for all α, form a *unitary* group and since this group is commutative it is called a unitary *abelian* group. The lagrangian of equation 1.4 is then said to be $U(1)$ phase (or gauge) invariant.

1.4.2 Quantum Electrodynamics (QED).

The global gauge invariance described in the previous section is not the most general symmetry that can be imposed. If the phase factor in the transformation of equation 1.5 now has an explicit spatial dependence i.e. $\alpha \equiv \alpha(x)$, then the lagrangian is no longer trivially invariant. This is immediately apparent from substituting

$$\psi(x) \rightarrow e^{i\alpha(x)}\psi(x) \tag{1.11}$$

into the lagrangian (equation 1.4). The complication arises from the derivative term, where

$$\partial_\mu\psi(x) \rightarrow e^{i\alpha(x)}\partial_\mu\psi(x) + \psi(x)ie^{i\alpha(x)}\partial_\mu\alpha(x) \tag{1.12}$$

$$\neq e^{i\alpha(x)}\partial_\mu\psi(x) \tag{1.13}$$

Here the differential dependence of the phase factor breaks the lagrangian symmetry. This complication is overcome by modifying the derivative operator, ∂_μ so that it too transforms under the local phase transformations, i.e. like ψ itself. To do this, it is necessary to introduce an additional vector field A_μ with transformation properties such that the extra term in equation 1.12 is cancelled. Thus, the *covariant derivative* is formed such that

$$D_\mu \equiv \partial_\mu - ieA_\mu \tag{1.14}$$

where A_μ transforms as

$$A_\mu \rightarrow A_\mu + \frac{1}{e}\partial_\mu\alpha \tag{1.15}$$

So, finally, invariance of the lagrangian under local gauge transformations can be regained if ∂_μ is replaced by the covariant derivative, D_μ, i.e.

$$\mathcal{L} = \bar{\psi}(i\gamma^\mu \partial_\mu - m)\psi + e\bar{\psi}\gamma^\mu \psi A_\mu \tag{1.16}$$

The second term in this modified lagrangian indicates that the new *GAUGE FIELD*, A_μ couples to the Dirac particle. If this field is to be regarded as the physical photon field then a kinetic energy term must be introduced into the lagrangian. Since, the kinetic energy term must remain invariant under the transformation of the gauge field it can only be expressed in terms of the field tensor, $F_{\mu\nu}$ i.e.

$$F_{\mu\nu} = \partial_\mu A_\nu - \partial_\nu A_\mu \tag{1.17}$$

The complete QED lagrangian then becomes

$$\mathcal{L}_{QED} = \bar{\psi}(i\gamma^\mu \partial_\mu - m)\psi - e j_\mu^{em} A_\mu - \frac{1}{4} F_{\mu\nu} F^{\mu\nu} \tag{1.18}$$

where the electromagnetic current (equation 1.9) has been substituted.

Inspection of $\mathcal{L}_{QED}$ indicates that there is no mass term associated with the gauge field, A_μ. Any arbitrary inclusion of such a term would break the symmetry of the lagrangian. This implies that the gauge boson associated with the gauge field is massless, as indeed the photon is.

It is clear from the above that the imposition of a local gauge invariance on the free fermion lagrangian has led to an interacting field theory of QED. Extending the field theory to QCD and electroweak unification is based on analogy with this theory of QED.

1.4.3 Quantum Chromodynamics (QCD).

The ideas of local gauge invariance which led to an interacting theory of QED in the previous section can be used to infer the structure of QCD. (This discussion is also useful when unifying the electromagnetic and weak interactions (see section 1.5), therefore the theory is described in relative detail). The added complication when considering transformations of quark fields is that a quark can be in any one of three colour states. If these are denoted by q_j with j =1,2,3 then the free quark lagrangian (for just one quark flavour) can be written

$$\mathcal{L}_o = \bar{q}_j(i\gamma^\mu\partial_\mu - m)q_j \tag{1.19}$$

(c.f. Dirac lagrangian equation 1.4). In order to consider the most general transformation, the fields q_j must be manipulated as a triplet of states. Mathematically the transformations are produced by eight linearly independent, traceless, 3x3 matrices. Thus the U(1) gauge group of QED is replaced by an SU(3) group of phase transformations. So, the local phase transformation which needs to be applied to the quark fields takes the form

$$q(x) \rightarrow Uq(x) \equiv e^{i\alpha_a(x)T_a}q(x) \tag{1.20}$$

where the summation over the repeated index a is implied, T_a (with a = 1,2,...,8) are the set of linearly independent, traceless, 3x3 matrices and $\alpha_a(x)$ are the group parameters (i. e. they give the magnitude of the transformation about each base state labelled by a). Explicit forms of the T_a matrices involve the Pauli spin matrices [3, 4]. It should be noted that not all the matrices, T_a commute and the relationship between matrices is expressed by the group algebra :

$$[T_a, T_b] = if_{abc}T_c \tag{1.21}$$

where f_{abc} are real constants termed the structure constants of the group. These are antisymmetric under interchange of any pair of indices. This non-commutation of transformation matrices implies that the theory is $non-abelian$.

In order to observe the effects of the local gauge invariance, it is sufficient to consider an infinitesimal transformation in 'the neighbourhood of the identity'. i.e.

$$q(x) \rightarrow (1 + i\alpha_a(x)T_a)q(x) \tag{1.22}$$

Substitution then again shows that the problem arises from the derivative term in the lagrangian

$$\partial_\mu q \rightarrow (1 + i\alpha_a(x)T_a)\partial_\mu q(x) + iT_a q\partial_\mu \alpha_a \tag{1.23}$$

the second term breaks the symmetry of $\mathcal{L}_o$. Thus, it appears that the formalism may proceed in exactly the same way as for QED, i.e. introduce gauge fields G^a_μ (eight in this case) each transforming as A_μ i.e.

$$D_\mu = \partial_\mu + igT_a G^a_\mu \tag{1.24}$$

(c.f. equation 1.15). Introducing these into $\mathcal{L}_o$ results in

$$\mathcal{L}_{QCD} = \bar{q}(i\gamma^\mu\partial_\mu - m)q - g(\bar{q}\gamma^\mu T_a q)G^a_\mu \tag{1.25}$$

(c.f. equation 1.16). However, this still has not produced a gauge invariant lagrangian, as substitution of equation 1.22 into the last term of $\mathcal{L}_{QCD}$ will show. The non-Abelian nature of the T_a matrices means that

$$(\bar{q}\gamma^{\mu}T_{a}q) \rightarrow (\bar{q}\gamma^{\mu}T_{a}q) - f_{abc}\alpha_{b}(\bar{q}\gamma^{\mu}T_{c}q) \tag{1.26}$$

where the group algebra of equation 1.21 has been used to produce the last term. It appears that another term is now present which needs to be absorbed so as to restore invariance. This is done by requiring the gauge field G^{a}_{μ} to transform as

$$G^{a}_{\mu} \rightarrow G^{a}_{\mu} - \frac{1}{g}\partial_{\mu}\alpha_{a} - f_{abc}\alpha_{b}G^{c}_{\mu} \tag{1.27}$$

Now all that remains is the introduction of a kinetic energy term associated with the gauge fields. Then the final QCD lagrangian reads

$$\mathcal{L}_{QCD} = \bar{q}(i\gamma^{\mu}\partial_{\mu} - m)q - g(\bar{q}\gamma^{\mu}T_{a}q) - \frac{1}{4}G^{a}_{\mu\nu}G^{\mu\nu}_{a} \tag{1.28}$$

where the field tensor $G^{a}_{\mu\nu}$ is given by

$$G^{a}_{\mu\nu} = \partial_{\mu}G^{a}_{\nu} - \partial_{\nu}G^{a}_{\mu} - gf_{abc}G^{b}_{\mu}G^{c}_{\nu} \tag{1.29}$$

As in the case of the QED lagrangian, $\mathcal{L}_{QCD}$ has no mass term associated to the gauge fields. Thus, the gauge particles attributed to the fields (gluons) are massless. The difference in the field tensor, $G^{a}_{\mu\nu}$, compared to the QED analogue has important implications. Substitution into $\mathcal{L}_{QCD}$ shows that there are self-interaction terms between the gluons, and indeed predicts the presence of three and four gluon vertices. These self-interaction terms are entirely due to the non-Abelian character of the SU(3) gauge group.

1.5 The Weak Interaction.

So far, only the electromagnetic and strong forces have been considered. Observation of events such as the decay of pions and muons via

$$\pi^- \rightarrow \mu^- \bar{\nu}_\mu \tag{1.30}$$

$$\mu^- \rightarrow e^- \bar{\nu}_e \nu_\mu \tag{1.31}$$

with lifetimes of 2.6×10^{-8} secs and 2.2×10^{-6} secs [3] respectively implied the presence of an interaction other than the strong and electromagnetic; since these typically have decay times of the order 10^{-23} secs and 10^{-16} secs respectively.

This weak interaction is also responsible for the β-decay of atomic nuclei, which involves the transformation of a proton to a neutron (or vice versa). The decay reactions can be written

$$p \rightarrow n e^+ \nu_e \tag{1.32}$$

$$n \rightarrow p e^- \bar{\nu}_e \tag{1.33}$$

The proton decay is only possible in the presence of a nucleus , but free neutron decay is possible and is entirely due to the weak interaction (otherwise the neutron would be as stable as the proton with a lifetime of $> 10^{30}$ years).

The continuous energy spectra of the β-decay products was the original observation which led Fermi to infer the presence of the (anti) neutrino. These neutrinos only interact via the weak interaction, are colourless, electrically neutral and within experimental limits also massless.

Early theories aiming to account for this interaction were based on analogy with the electromagnetic interaction. Fermi proposed a vector- vector current interaction with the current structure of a form similar to equation 1.9 [5]. This method had its successes, but failed to account for non-conservation of parity in decays such as

$$K \rightarrow 2\pi, 3\pi \tag{1.34}$$

in which the two final states have opposite parities. The assertion that the weak interaction did not conserve parity was verified experimentally in studies of β-transitions of polarised cobalt nuclei [3]:

$$^{60}Co \rightarrow ^{60} Ni^{*} + e^{-} + \bar{\nu}_{e} \tag{1.35}$$

The observed asymmetry in the direction of the emitted electrons and the correlation between the ^{60}Co nuclear spin and electron momentum is explained if the antineutrino has a right-handed helicity and the electron a left-handed helicity. Further experiments have indeed shown that only right-handed antineutrinos and left-handed neutrinos are involved in weak interactions. The absence of right(left)-handed (anti)neutrinos is a clear violation of invariance under parity, P. Weak interactions also violate invariance under charge conjugation, C, since under this operation a left-handed neutrino is transformed into a left-handed antineutrino. However, the combined CP operation does produce invariance. The form of the current which reproduces these observations is known as 'V-A', since the current, J^{μ} can be written as the difference

$$J^{\mu} = J^{\mu}_{V} - J^{\mu}_{A} \tag{1.36}$$

where J^{μ}_{V} is the parity conserving vector current:

$$J^{\mu}_{V} = \bar{\psi}_{l}\gamma^{\mu}\psi_{\nu_{l}} \tag{1.37}$$

and J^{μ}_{A} is the parity violating axial vector current:

$$J^{\mu}_{A} = \bar{\psi}_{l}\gamma^{\mu}\gamma_{5}\psi_{\nu_{l}} \tag{1.38}$$

Thus,

$$J^{\mu} = \bar{\psi}_l \gamma^{\mu}(1 - \gamma_5)\psi_{\nu_l} \tag{1.39}$$

It should be noted that the factor in between the particle fields in equation 1.39 automatically selects left-handed neutrinos (or right-handed antineutrinos) since $1/2(1 - \gamma_5)$ is the projection operator which does precisely that.

1.5.1 The Weak Intermediate Vector Boson.

Fermi's original formalism of weak interactions assumed a point interaction with the coupling between the currents given by a constant, G_F. In completing the analogy with QED it becomes apparent that G_F essentially replaces the photon propagator and thus, in contrast to the dimensionless coupling, e, G_F must have dimensions of GeV^{-2}. This, in conjunction with the observation that the weak interaction must have a short range, leads to the requirement of massive vector bosons mediating the weak process. These are the analogues of the photon for the electromagnetic force and the gluons for the colour force. The interaction then no longer occurs at a point (especially at high energies). However, this limit is regained when the momentum of the weak boson is much smaller than its mass.

The need for a massive vector boson creates a complication when attempting to produce a gauge theory which is to incorporate the weak interaction. In the formalisms for QED and QCD local gauge invariance resulted in massless gauge bosons, which was fine for describing the photon and gluons. Any arbitrary introduction of mass terms immediately breaks the symmetry of the lagrangian.

It will be explained that mass terms can be introduced by breaking the lagrangian symmetry in a more subtle manner, i.e. *spontaneous symmetry breaking* and the *Higgs Mechanism*. Before this, the next section describes how the weak interaction is incorporated in electroweak unification.

1.6 Electroweak Unification.

It has already been mentioned in the previous section how only left- handed neutrinos have been observed. Therefore, any consistent description of the weak interaction must take this into account, i.e it must be a *chiral* theory which treats left- and right- handed components in different ways. Also, mentioned in the previous section is how the factor $a_L = 1/2(1 - \gamma_5)$ acts as a projection operator which selects left-handed components.

The electromagnetic current, (see equation 1.9) can be re-written in terms of its chiral components as:

$$-j_\mu^{em} = \bar{\psi}_L \gamma_\mu \psi_L + \bar{\psi}_R \gamma_\mu \psi_R \tag{1.40}$$

where the L,R subscripts to the fields refer to left- and right- chiral components respectively. Indeed, re-writing the QED lagrangian in terms of chiral components and then applying the QED gauge transformation of equation 1.11 leaves it invariant, with the left- and right- handed components being treated in exactly the same manner (i.e. QED is a non-chiral theory). This expansion will be of use later, when the weak current will be expressed in chiral components.

1.6.1 Glashow's Model.

Consider the leptonic current

$$L_\mu = \bar{e}\gamma_\mu(1 - \gamma_5)\nu_e + \bar{\mu}\gamma_\mu(1 - \gamma_5)\nu_\mu + \bar{\tau}\gamma_\mu(1 - \gamma_5)\nu_\tau \tag{1.41}$$

where the particle names have been used to replace the fields. Since each lepton component in L_μ should behave similarly (i.e. assume lepton universality), the formalism is further developed in terms of just the electronic part. Then ;

$$\frac{1}{2}L_e = \bar{e}\gamma_\mu a_L \nu_e \tag{1.42}$$

$$= \bar{e}_L \gamma_\mu \nu_{eL} \tag{1.43}$$

where the projection operator a_L has been used. Thus only the left-handed components appear. To try and re-cast this current into a form similar to the electromagnetic current it is convenient to introduce a left-chiral doublet of the form :

$$E_L = \begin{pmatrix} \nu_{eL} \\ e_L \end{pmatrix} \tag{1.44}$$

To construct a current in terms of this doublet which remains invariant under transformations, it is necessary to re-introduce the three Pauli matrices, τ_i which satisfy the commutation relations :

$$[\tau_i, \tau_j] = 2i\varepsilon_{ijk}\tau_k \tag{1.45}$$

where ε_{ijk} is a completely antisymmetric tensor. Using these matrices it is possible to construct the three *weak isospin* currents :

$$T^{(i)}_{L\mu} = \bar{E}_L \gamma_\mu \frac{1}{2} \tau^{(i)} E_L \qquad (i = 1, 2, 3) \tag{1.46}$$

which then give

$$\frac{1}{2} L_\mu(e) = T^{(1)}_{L\mu} - iT^{(2)}_{L\mu} \equiv T^{-}_{L\mu} \tag{1.47}$$

$$\frac{1}{2} L^\dagger_\mu(e) = T^{(1)}_{L\mu} + iT^{(2)}_{L\mu} \equiv T^{+}_{L\mu} \tag{1.48}$$

for the electronic current and its hermitian conjugate. The charges corresponding to these currents are

$$q^{(i)} = \int T^{(i)}(x) d^3x \tag{1.49}$$

It should be noted that since the weak isospin currents are expressed in terms of the 2x2 matrices τ_i, the same matrices must comprise the generators of the transformations under which the theory must remain invariant. (This is in accordance with Noether's theorem). Now, since the 2x2 τ_i matrices all have a determinant of one, the formalism is an SU(2) theory.

A direct consequence of writing the weak isospin current as in equation 1.46 is that there will also be a third isospin current ;

$$\vdots$$

$$T^{(3)}_{L\mu} = \bar{E}_L \gamma_\mu \frac{1}{2} \tau^{(3)} E_L \tag{1.50}$$

$$= \frac{1}{2}(\bar{\nu}_{eL} \gamma_\mu \nu_{eL} - \bar{e}_L \gamma_\mu e_L) \tag{1.51}$$

This can be compared with the electromagnetic current, equation 1.40 (re-written in the notation of equation 1.51)

$$j_\mu(e) = -\bar{e}_L \gamma_\mu e_L - \bar{e}_R \gamma_\mu e_R \tag{1.52}$$

Both these currents are neutral (since they both couple either electrically neutral leptons or electrically charged leptons), and it can be seen that $T^{(3)}_{L\mu}$ contains half of the electromagnetic current , i.e. the $-\bar{e}_L \gamma_\mu e_L$ term is common to both. It is apparent that both $T^{(3)}_{L\mu}$ and $j_\mu(e)$ neutral currents will break any SU(2) symmetry made up of the τ_i matrices (clear from the non-abelian nature of the τ_i - see section 1.3.3). The idea then is to construct a combination which on the one hand has definite transformations under SU(2) and completes the weak isospin triplet and on the other hand contains a part which remains unchanged under SU(2) and completes the electromagnetic current. Thus the theory begins to take on both an

electromagnetic and a weak element. All this is achieved by introducing the *weak hypercharge current*, Y_μ, so that

$$j_\mu(e) = T^{(3)}_{L\mu} + Y_\mu \tag{1.53}$$

i.e.

$$Y_\mu = -\frac{1}{2}\bar{E}_L\gamma_\mu E_L - \bar{e}_R\gamma_\mu e_R \tag{1.54}$$

The weak hypercharge, Y is given by;

$$Q = T^{(3)} + \frac{Y}{2} \tag{1.55}$$

where Q is the electromagnetic charge and $T^{(3)}$ is the third weak isospin charge. Since both these quantities are conserved, it implies that Y is also conserved. From Noether's theorem this means that Y is the generator of the $U(1)_Y$ symmetry group. Now, the hypercharge current, Y_μ is a combination in terms of a doublet E_L with hypercharge, $|1/2|$ and a singlet, e_R with hypercharge -1. This exhibits the chiral construction of the theory, i.e. the left- (E_L) and right- (e_R) handed components are treated differently . The resulting theory therefore cannot be described by a single gauge group but a more complicated $SU(2)\times U(1)$ group.

The construction of the electroweak lagrangian then proceeds in analogy with the steps leading to the QED lagrangian, $\mathcal{L}_{QED}$ (equation 1.18). There, the electromagnetic current, j^{em}_μ couples to the $U(1)_{em}$ gauge field, A_μ with a coupling e. Carrying this over to the electroweak theory then requires three fields, W^i_μ coupling to the three weak isospin currents with coupling g, and a fourth field, B_μ which couples to the weak hypercharge with strength g'. The lagrangian can then be written as :

$$\mathcal{L} = \sum_l \mathcal{L}(l) + \mathcal{L}(W) + \mathcal{L}(B) \tag{1.56}$$

where the summation is over the three lepton types.

For the lagrangian to be invariant under local SU(2)×U(1) gauge transformations, it is necessary to introduce the covariant derivative

$$D_\mu = \partial_\mu + \frac{i}{2} g \tau_i W_i^\mu + i g' Y_\mu B^\mu \tag{1.57}$$

and for the fields to transform non-trivially as

$$\vec{W}_\mu \rightarrow \vec{W}'_\mu = \vec{W}_\mu + g\vec{\Lambda} \times \vec{W}_\mu + \partial_\mu \vec{\Lambda} \tag{1.58}$$

$$B_\mu \rightarrow B'_\mu = B_\mu + \partial_\mu \Lambda \tag{1.59}$$

$$L_L \rightarrow L'_L = (1 - \frac{i}{2}\vec{\tau}.\vec{\Lambda} + \frac{i}{2} g' \Lambda) L_L \tag{1.60}$$

$$l_R \rightarrow l'_R = (1 + i g' \Lambda) l_R \tag{1.61}$$

where Λ are the group parameters. The leptonic component of the lagrangian then reads

$$\mathcal{L}(l) = \bar{L}_L \gamma_\mu (i\partial_\mu - \frac{g}{2}\tau^i W_\mu^i - g'(-\frac{1}{2}) B_\mu) L_L + \bar{l}_R \gamma_\mu (i\partial_\mu - g'(-1) B_\mu) l_R \tag{1.62}$$

where l is a lepton spinor and L_L the doublet

$$L_L = \begin{pmatrix} \nu_{lL} \\ l_L \end{pmatrix} \tag{1.63}$$

The $\mathcal{L}(W)$ and $\mathcal{L}(B)$ terms in equation 1.56 are the kinetic energy terms associated with the gauge fields. i.e.

$$\mathcal{L}(W) = -\frac{1}{4} W_{\mu\nu} W^{\mu\nu} \tag{1.64}$$

$$\mathcal{L}(B) = -\frac{1}{4} B_{\mu\nu} B^{\mu\nu} \tag{1.65}$$

where $W_{\mu\nu}$ is the Yang-Mills-Shaw field [6];

$$W_{\mu\nu} = \partial_\mu W_\nu - \partial_\nu W_\mu - gW_\mu \times W_\nu \tag{1.66}$$

and

$$B_{\mu\nu} = \partial_\mu B_\nu - \partial_\nu B_\mu \tag{1.67}$$

The last term in $W_{\mu\nu}$ is a direct result of the non- Abelian nature of the SU(2) group (see equation 1.26). It describes the self-interactions of the gauge bosons. There is no extra term in the $B_{\mu\nu}$ expression since this relates the Abelian U(1) group.

A further examination of the lagrangian given by equation 1.62 shows that there are no mass terms for either the leptons or the gauge bosons; an obvious deficiency of the theory so far. Indeed, there can be no leptonic mass terms as the left- and right- handed chiral components transform differently (see equations 1.58 - 1.61). Thus the inclusion of any mass term such as $-m\psi\bar{\psi}$ (as in the QED case) would break the symmetry of the lagrangian. Similarly, the gauge field transformations would also break the lagrangian symmetry.

1.6.2 Electroweak Couplings.

In order to determine the vertex couplings between the gauge bosons and the leptons the leptonic lagrangian of equation 1.62 must be re-written into gauge boson - leptonic field interaction and non-interaction terms i.e. $\mathcal{L}_I$ and $\mathcal{L}_{NI}$ respectively. Considering only the electronic part :

$$\mathcal{L}(e) = \mathcal{L}_I + \mathcal{L}_{NI} \tag{1.68}$$

where

$$\mathcal{L}_{NI} = i\bar{E}_L\gamma_\mu\partial_\mu E_L + i\bar{e}_R\gamma_\mu\partial_\mu e_R \tag{1.69}$$

$$\mathcal{L}_I = \bar{E}_L\gamma_\mu[-\frac{g}{2}\tau^i W^i_\mu + \frac{g'}{2}B_\mu]E_L + \bar{e}_R\gamma_\mu g' B_\mu e_R \tag{1.70}$$

It is the interaction lagrangian, $\mathcal{L}_I$ which includes the vertex couplings of interest. This component can be further separated in terms of only couplings involving the charged current, (CC) and couplings involving the neutral current, (NC). Thus

$$\mathcal{L}_I = \mathcal{L}_{CC} + \mathcal{L}_{NC} \tag{1.71}$$

where

$$\mathcal{L}_{CC} = -\bar{E}_L \gamma_\mu \frac{g}{2} \sum_{i=1,2} \tau^i W^i_\mu E_L \tag{1.72}$$

$$= \bar{\nu}_{eL}[-\frac{g}{2\sqrt{2}}\gamma_\mu(1-\gamma_5)]eW^{+\mu} + \bar{e}[-\frac{g}{2\sqrt{2}}\gamma_\mu(1-\gamma_5)]\nu_{eL}W^{-\mu} \tag{1.73}$$

where

$$W^\pm_\mu = \frac{1}{\sqrt{2}}(W^{(1)}_\mu \mp iW^{(2)}_\mu) \tag{1.74}$$

(c.f. equations 1.47 - 1.48). The expressions in the square brackets then give the coupling at the neutrino-electron-charged gauge boson, i.e . $eW\bar{\nu}_{eL}$ vertex.

The neutral component, $\mathcal{L}_{NC}$ is given by

$$-\mathcal{L}_{NC} = \bar{E}_L \gamma_\mu (g W^{(3)}_\mu \frac{1}{2}\tau^3 - \frac{1}{2}g' B_\mu) E_L - \bar{e}_R \gamma_\mu g' B_\mu e_R \tag{1.75}$$

$$= g T^{(3)}_{L\mu} W^{(3)\mu} + g' Y_\mu B^\mu \tag{1.76}$$

where equations 1.51 and 1.54 have been used in the last step. Now, for the theory to be consistent with QED, it is necessary for the electromagnetic field, A_μ to couple to the electromagnetic current, $j_\mu(e)$ given by equation 1.52. To do this the *Glashow angle* θ_W is introduced and linear combinations of $W^{(3)}_\mu$ and B_μ are taken. Thus, the neutral gauge fields are re-written as

$$W^{(3)}_\mu = cos\theta_W Z_\mu + sin\theta_W A_\mu \tag{1.77}$$

$$B_\mu = -sin\theta_W Z_\mu + cos\theta_W A_\mu \tag{1.78}$$

where A_μ is the usual electromagnetic field of QED and Z_μ is an additional neutral gauge field. Substituting these into equation 1.76 gives

$$-\mathcal{L}_{NC} = (gT^{(3)}_{L\mu}cos\theta_W - g'Y_\mu sin\theta_W)Z_\mu + (gT^{(3)}_{L\mu}sin\theta_W + g'Y_\mu cos\theta_W)A_\mu \quad (1.79)$$

To ensure that the electromagnetic field, A_μ is coupled to the current with strength, e (see equation 1.16), one requires

$$gsin\theta_W = g'cos\theta_W = e \quad (1.80)$$

Thus eliminating g', $\mathcal{L}_{NC}$ becomes

$$-\mathcal{L}_{NC} = ej_\mu A_\mu + \frac{g}{cos\theta_W}[T^{(3)}_{L\mu} - sin^2\theta_W j_\mu]Z_\mu \quad (1.81)$$

Finally, substituting for the currents into the above current lagrangian gives the vertex couplings listed in table 1.2. The charged current couplings are also listed.

Table 1.2 is not an exhaustive list of vertex couplings, indeed the self-interactions of the gauge bosons have not been included [7].

Hence, constructing a lagrangian in terms of the weak isospin and hypercharge currents, and requiring it to be invariant under local SU(2)×U(1) gauge transformations has produced a theory which describes both the electromagnetic and weak interactions. In doing so it has been necessary to introduce charged vector bosons, $W^\pm$ which mediate the charged weak current (i.e. the quanta of the $W^\pm$ fields). Also, in requiring the electromagnetic current to be coupled to the electromagnetic field, an unavoidable additional neutral current coupled to another neutral vector boson, the Z^0 has resulted, with the couplings being dependent on an extra parameter of the theory, i.e. $sin^2\theta_W$, which has to be determined by experiment.

vertex	current type	coupling
$e\nu_e W^{\pm}$	charged	$-\frac{ig}{2\sqrt{2}}\gamma_\mu(1-\gamma_5)$
$ee\gamma$	neutral	$ie\gamma_\mu$
$\nu_e\nu_e Z$	neutral	$\frac{ig}{4cos\theta_W}\gamma_\mu(1-\gamma_5)$
eeZ	neutral	$\frac{ig}{2cos\theta_W}(g_V^e - g_A^e\gamma_5)$
		where $g_V^e = \frac{1}{2} - 2sin^2\theta_W$
		$g_A^e = \frac{1}{2}$

Table 1.2: Vertex coupling factors.

It in fact is the purpose of this thesis to provide an experimental measurement of $sin^2\theta_W$ which then gives an indication of the relative strength of the vector and axial-vector coupling strengths via

$$\frac{g_V}{g_A} = 1 - 4sin^2\theta_W \tag{1.82}$$

Although this expression was derived considering only the electronic component of the leptonic lagrangian, assuming lepton universality will validate it for the other leptons, i.e. $g_{V/A}^e = g_{V/A}^\mu = g_{V/A}^\tau$. This will not be true for quark production.

It is interesting to note that with an experimentally measured value of 0.2325 ± 0.0008 for $sin^2\theta_W$ [8], the neutral current associated with the massive neutral vector boson Z^0 is not pure V-A and is closer to being purely axial.

1.7 The Goldstone Model and Spontaneous Symmetry Breaking.

In producing a locally gauge invariant lagrangian in the previous sections, all particles were manifestly required to be massless. Although this is fine for photons and gluons, it is obviously incorrect for other particles. Thus, mass terms need to be introduced into the lagrangian in a more subtle way, i.e. the method known as *spontaneous symmetry breaking*. After introducing this procedure it will be included into the gauge invariant lagrangians derived so far, leading to massive gauge bosons and then finally to massive leptons.

1.7.1 The Goldstone Model.

This is based on the fact that a theory that is exactly invariant under a symmetry can have a ground state which does not exhibit this symmetry. To elucidate on this idea, consider a system whose lagrangian, $\mathcal{L}$ is invariant under a particular symmetry. In determining the ground state of the system, essentially two possibilities can occur. Firstly, the ground state can be non-degenerate so that it is uniquely defined. It will then possess the symmetry of the lagrangian. Secondly, the ground state can be degenerate, so that there is no unique minimum. However, one of these degenerate states can be arbitrarily chosen to be the ground state; it will then no longer have the symmetry of the lagrangian. This method of obtaining an asymmetric ground state is known as *spontaneous symmetry breaking*. The asymmetry does not arise from the addition of a non-invariant term to the lagrangian, but from an arbitrary choice of one of the degenerate ground states.

In field theory, particles arise when the field is expanded about some constant value for which the potential (and thus the energy) has an absolute minimum. For the lagrangians considered so far the potential terms have possessed trivial minima at the point where $\phi(x) = 0$, and this has given rise to massless particles. It will be seen in the discussion that follows how expansion about a non-trivial minimum (i.e. $\phi(x) \neq 0$) will result in massive particles. This of course requires the ground state (i.e. the vacuum state) to have a definite (but degenerate!) expectation

value.

To examine these ideas further, consider the lagrangian

$$\mathcal{L} = (\partial_\mu \phi)^*(\partial^\mu \phi) - \mu^2 \phi^* \phi - \lambda(\phi^* \phi)^2 \tag{1.83}$$

where $\phi(x)$ is a complex, scalar field which can be expressed as

$$\phi(x) = \frac{1}{\sqrt{2}}(\phi_1(x) + i\phi_2(x)) \tag{1.84}$$

and the lagrangian 1.83 then becomes

$$\mathcal{L} = \frac{1}{2}(\partial_\mu \phi_1)^2 + \frac{1}{2}(\partial_\mu \phi_2)^2 - \frac{1}{2}\mu^2(\phi_1^2 + \phi_2^2) - \frac{1}{4}\lambda(\phi_1^2 + \phi_2^2)^2 \tag{1.85}$$

This lagrangian is invariant under the U(1) global phase transformation, $\phi \rightarrow e^{i\alpha}\phi$. Of interest in this lagrangian are the potential energy terms

$$V(\phi) = \mu^2|\phi|^2 + \lambda|\phi|^4 \tag{1.86}$$

where μ^2 and λ are arbitrary real parameters. For the energy of the field to possess a minimum, λ must be positive. The Hamiltonian of the system (i.e. the sum of the kinetic and potential energy) has a kinetic term which is positive definite and which vanishes for a constant value of the field $\phi(x)$. Thus, the Hamiltonian and hence the total energy of the field has a minimum at the constant value of $\phi(x)$ which minimises $V(\phi)$. This will be the ground state of the system.

Now, two possibilities arise depending on the relative sign of μ^2. (i) If $\mu^2 > 0$, then the potential is positive definite, possessing a trivial minimum at $\phi(x)=0$. As explained earlier, this results in the generation of massless particles. (ii) If $\mu^2 < 0$, then the potential shape is shown in figure 1.1

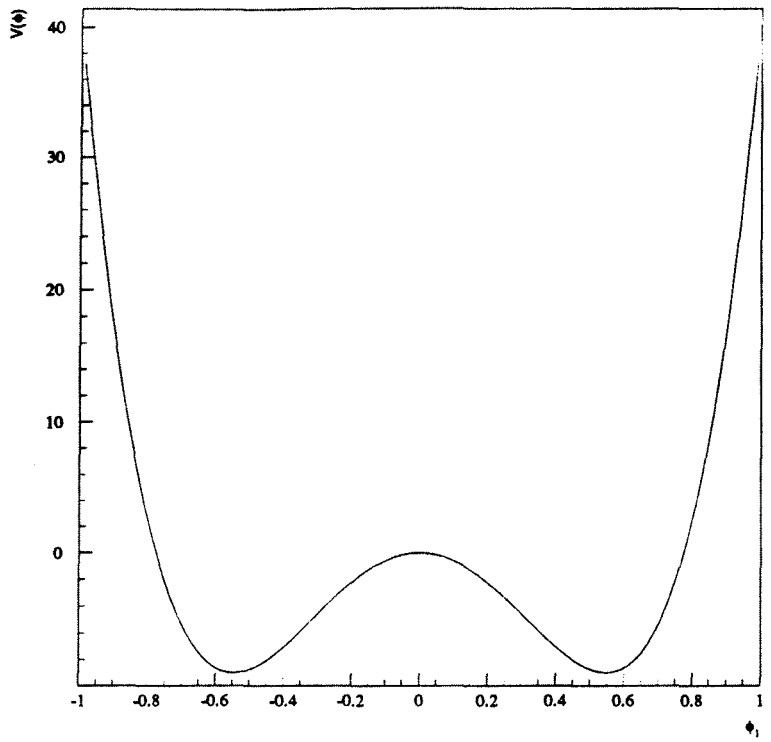

Figure 1.1: Example of a scalar field potential with non-trivial minima permitting spontaneous symmetry breaking. Projection shown is for ϕ_2=0.

This potential now has a whole circle of minima at

$$\phi_1^2 + \phi_2^2 = v \tag{1.87}$$

with $v^2 = \mu^2/\lambda$. This ground state degeneracy is spontaneously broken by selecting $\phi_1(x) = v$ and $\phi_2(x) = 0$. Thus the vacuum now has an expectation value about which the field is expanded. This is done in terms of the fields η and ζ by substituting

$$\phi(x) = \frac{1}{\sqrt{2}}(v + \eta(x) + i\zeta(x)) \tag{1.88}$$

into the lagrangian 1.83 giving

$$\mathcal{L}' = \frac{1}{2}(\partial_\mu \zeta)^2 + \frac{1}{2}(\partial_\mu \eta)^2 + \mu^2\eta^2 + constant + \mathcal{O}(\eta^3) + \mathcal{O}(\zeta^3) + ... \tag{1.89}$$

The third term (quadratic in the $\eta(x)$ field) has the form of a mass term associated with the $\eta(x)$ field. Thus, the η mass is $m_\eta = \sqrt{-2\mu^2}$. For the $\zeta(x)$ field there is a kinetic energy term present (the first term) in $\mathcal{L}'$, but there is no term quadratic in $\zeta(x)$ which could be associated to be the mass term. The mass of the particle associated with this field is therefore zero. The higher order terms represent interactions of the two fields.

The fields $\eta(x)$ and $\zeta(x)$ represent the fluctuations of the field $\phi(x)$ about the vacuum. Thus, it is apparent that spontaneous symmetry breaking results in massless as well as massive gauge bosons. This is a direct consequence of the ground state degeneracy i.e. there is one direction in which the potential remains constant when expanding about the minimum, which therefore offers no resistance to excitations. This is an example of Goldstones Theorem which states that to every generator of the symmetry group that is spontaneously broken there corresponds a massless particle, the Goldstone boson.

It appears that in generating massive particles the theory becomes plagued by massless scalar Goldstone bosons which need to be eliminated. In the extension to this theorem (see section 1.8) it will become apparent how imposing local gauge invariance can achieve the objective (so far only global gauge invariance has been considered).

1.8 The Higgs Mechanism.

Extending the ideas of the Goldstone Model to a U(1) locally gauge invariant theory, requires replacing the derivatives, ∂_μ by covariant derivatives, $D_\mu = \partial_\mu + iqA_\mu$, the introduction of a gauge field A_μ which transforms as $A_\mu \rightarrow A_\mu + 1/e\partial_\mu\alpha$ (where α is the group parameter), and a kinetic energy term in the form of the field tensor $F_{\mu\nu}$ (see section 1.4.2). The lagrangian reads

$$\mathcal{L} = (D^\mu\phi)^*(D^\mu\phi) - \mu^2(\phi^*\phi) - \lambda(\phi^*\phi)^2 - \frac{1}{4}F_{\mu\nu}F^{\mu\nu} \tag{1.90}$$

Again, the potential is required to be such that $\lambda > 0$ and $\mu^2 < 0$, corresponding to a degenerate ground state. This degeneracy can be broken by choosing a point on the circle of minima as in equation 1.87, i.e. the vacuum now has a finite expectation value, v . The next step is crucial in the final interpretation of the lagrangian . Instead of considering fluctuations of the field $\phi(x)$ about v in terms of fields $\eta(x)$ and $\zeta(x)$ as in equation 1.88, it is done in 'polar coordinates' as

$$\phi(x) = \frac{1}{\sqrt{2}}(v + \eta(x))e^{-i\zeta(x)/v} \tag{1.91}$$

where $\eta(x)$ represents the field fluctuations in the radial direction and $\zeta(x)$ the fluctuations in the angular direction about the vacuum expectation value, $v = \mu/\sqrt{\lambda}$. Substituting the expansion 1.91 into the lagrangian 1.90, results in a rather lengthy and complicated expression [7], the essence of which can be related by simply considering the substitution of 1.91 into the covariant derivative,D_μ. This gives

$$D_\mu\phi(x) = (\partial_\mu - ie[A_\mu + \frac{1}{e}\partial_\mu(\zeta/v)])\frac{1}{\sqrt{2}}e^{-i\zeta/v}(\eta + v) \tag{1.92}$$

A careful look at this expression reveals that the term in the square brackets is precisely the condition the gauge field A_μ must satisfy when the lagrangian is subjected to a U(1) gauge transformation i.e

$$\phi(x) \rightarrow \phi'(x) = e^{-i\zeta/v}\phi(x) \tag{1.93}$$

(see section 1.3.2). Thus, the term in the square brackets may be replaced by a gauge transformed field A'_μ. It becomes apparent that on completing the substitution into the lagrangian 1.90, all terms in the field $\zeta(x)$ disappear. In the last section (1.6.1) it was this field which gave rise to the massless Goldstone bosons.

The fields that remain are $\eta(x)$ and A'_μ both with massive gauge bosons. The field $\eta(x)$ is the Higgs field and its corresponding scalar particle is the Higgs boson. Thus in requiring local gauge invariance, the gauge bosons attain a mass, but for this to happen additional scalar particles, i.e. the Higgs bosons must also be present.

1.9 The Standard Electroweak Theory.

The Higgs Mechanism is now applied to the electroweak theory developed in section 1.5 to produce massive gauge bosons, $W^\pm$ and Z^0.

Since now an SU(2) symmetry must be broken, the Higgs field is written as a weak isospin doublet

$$\phi(x) = \begin{pmatrix} \phi_1(x) \\ \phi_2(x) \end{pmatrix} \tag{1.94}$$

The transformation laws of this doublet under SU(2) gauge transformations are the same as those for the isospin doublet L_L (1.63) and similarly the transformation properties under U(1) are as given in equations 1.61. (Note, however, that the weak hypercharge, Y, has not yet been determined for the Higgs doublet).

The Higgs component to the electroweak lagrangian can be written as

$$\mathcal{L}_H = (D_\mu\phi)^*(D_\mu\phi) - \mu^2\phi^*\phi - \lambda(\phi^*\phi)^2 \tag{1.95}$$

The covariant derivative is given by

$$D^\mu\phi(x) = (\partial_\mu + \frac{i}{2}g\tau_i W_i^\mu + ig'YB^\mu(x))\phi(x) \tag{1.96}$$

(c.f. equation 1.57). Now, following the derivation of the previous section (1.7), for $\lambda > 0$ and $\mu^2 < 0$ the potential term has a minimum for a constant Higgs field value of

$$\phi_1^2 + \phi_2^2 = -\frac{\mu^2}{2\lambda} = \frac{v^2}{2} \tag{1.97}$$

Then, the symmetry can be spontaneously broken by choosing a vacuum expectation value such that

$$\phi_0 = \begin{pmatrix} 0 \\ v/\sqrt{2} \end{pmatrix} \tag{1.98}$$

Now, expanding about this point requires substituting

$$\phi_0 = \begin{pmatrix} 0 \\ \frac{1}{\sqrt{2}}(v + \eta(x)) \end{pmatrix} \tag{1.99}$$

into the Higgs lagrangian 1.95 . Here, only the radial field $\eta(x)$ enters explicitly since the angular expansion can be 'gauged ' away (see section (1.7)). Carrying out this substitution, with the weak hypercharge value, $Y = 1/2$ [4] results in

$$\mathcal{L}_H = \frac{1}{2}(\partial^\mu \eta)(\partial_\mu \eta) - \frac{\mu^2}{2}\eta^2 + \frac{g^2}{4}v^2 W_\mu^+ W_\mu^- + \frac{v^2}{8}(gW_3^\mu - g'B^\mu)^2 + ... \tag{1.100}$$

From this lagrangian a Higgs scalar, η with mass μ can be identified. Also, the intermediate vector bosons, $W^\pm$ get masses of

$$M_W = \frac{gv}{2} \tag{1.101}$$

The last term in $\mathcal{L}_H$ gives one linear combination of the two neutral fields, W_3^μ and B^μ. The other orthogonal combination does not appear. Thus, if the combination present is written as (see equations 1.77 - 1.78)

(1.102)

$$Z^{\mu} = W_3^{\mu} cos\theta_W - B^{\mu} sin\theta_W$$

and its orthogonal combination

$$A^{\mu} = W_3^{\mu} sin\theta_W - B^{\mu} cos\theta_W \tag{1.103}$$

the weak vector boson, Z^0 attains a mass

$$M_Z = \frac{vg}{2cos\theta_W} = \frac{M_W}{cos\theta_W} \tag{1.104}$$

while the photon associated with A^{μ} remains massless.

1.9.1 Lepton and Quark Masses.

To complete the formalism to the point where the leptons themselves attain mass requires the addition of yet another term to the overall lagrangian. The same Higg's doublet (1.94) which was used to generate $W^{\pm}$ and Z^0 masses can be used to generate lepton masses. The fields are coupled by a Yukawa coupling, thus the addition to the lagrangian can be written :

$$\mathcal{L}_Y = -G_l(\bar{L}_L \phi l_R + \bar{l}_R \phi^* L_L) \tag{1.105}$$

where G_l is the Yukawa coupling term for lepton, l, L_L and l_R are the lepton left-handed doublet and right-handed singlet respectively. Spontaneous symmetry breaking in the now usual manner requires replacing the Higg's field, ϕ by (1.99), yielding:

$$m_l = \frac{1}{\sqrt{2}} G_l v \tag{1.106}$$

for the lepton masses. Since, G_l are arbitrary for each lepton type, the actual lepton masses are not predicted by the theory, but remain as parameters to be determined by experiment.

Quark masses can be generated in a similar manner. The only difference now of course is that both members of a quark doublet must attain a mass . Consequently another Higgs doublet, behaving exactly as (1.94) must be introduced. Now, the symmetry is spontaneously broken by giving the upper component of the new Higgs doublet a vacuum expectation value. Another complication with quarks is the experimental observation of quark mixing between quark doublets. This means the quark doublets entering the lagrangian for mass generation must be expressed in terms of 'rotated' quark eigenstates, i.e. a linear combination of the pure eigenstates related by the Cabibbo angle, θ_C [3].

Summarising the lagrangian formulation, the overall lagrangian for the Minimal Standard Electroweak Model, $\mathcal{L}_{MSEM}$ becomes :

$$\mathcal{L}_{MSEM} = \sum_l \mathcal{L}_l + \mathcal{L}_W + \mathcal{L}_B + \mathcal{L}_H + \mathcal{L}_Y \tag{1.107}$$

representing interactions of leptons, gauge bosons and the Higgs boson, with the masses of the gauge bosons, leptons and the fine structure constant remaining as parameters to be determined by experiment.

1.10 Higher Order Diagrams and Renormalisation.

So far the theory has been described only at the lowest order, i.e. at the 'tree-level'. There has been no mention of higher order corrections such as the vacuum polarisation and self-energy diagrams shown in figure 1.2

The Feynman graph of figure 1.2(a) shows a photon materialising into a fermion-antifermion pair, before mutual annihilation back into a photon, and figure 1.2(b) shows a fermion emitting a photon which it then reabsorbs. Further diagrams can be constructed to higher orders of complexity. All these combinations contribute

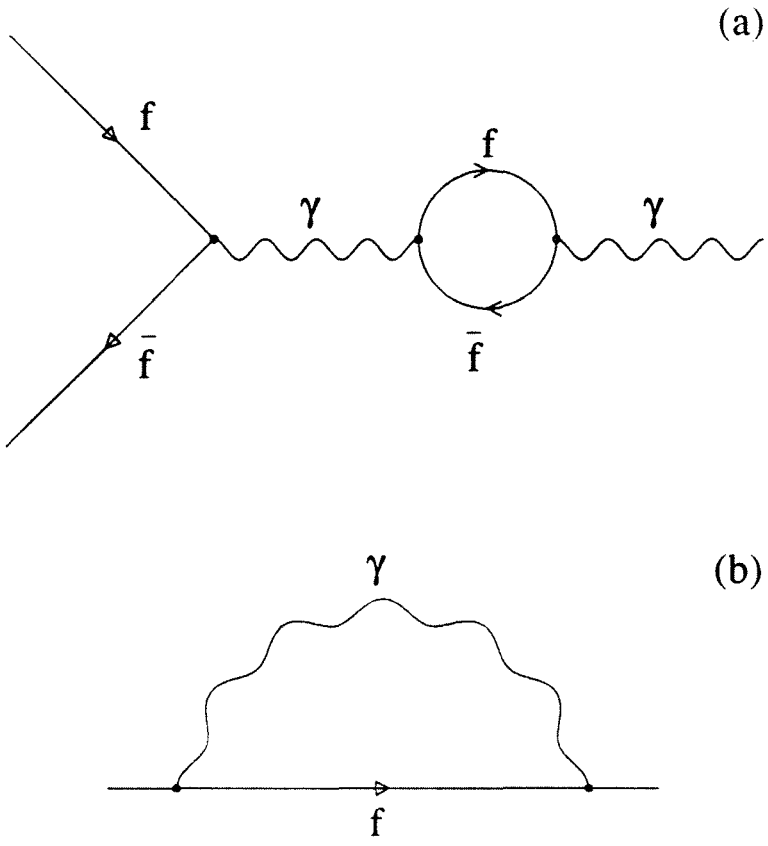

Figure 1.2: (a) Vacuum polarisation loop in the photon propagator. (b) An example of a virtual photon self-energy higher order correction. In both cases f represents any fermion.

to the overall observables measured in experiments, such as the fermion masses, electronic charge etc.

In analysing these complications, Feynman rules developed for tree level diagrams can be used after modification where necessary [3] . Thus, for the vacuum polarisation diagram of figure 1.2(a), where the fermion is an electron, the $ee\gamma$ vertex factor listed in table 1.2 will enter in the matrix element calculation three times. However, explicit analysis shows that this results in divergent integrals destroying the predictability of the theory. The divergences can be understood by considering the momentum in the fermion-antifermion loop. Although it must be conserved at each vertex, there is no restriction on the momentum circulating inside the loop, and since it is not observable, it must be integrated over. It is this sort of integration which leads to infinities in the theory. These divergent

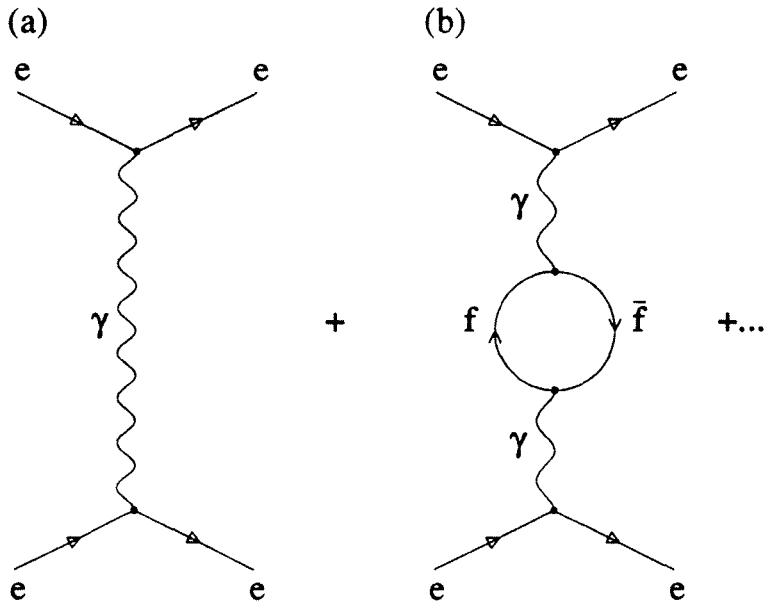

Figure 1.3: Electron scattering feynman diagrams, (a) at the lowest or tree level, (b) correction diagram due to vacuum polarisation in the photon propagator.

quantities appear in all QED processes (electroweak processes are saved to some extent by the massive vector bosons mediating them [3]), and can be compensated for by a redefinition of the electronic charge and mass.

It appears that the coupling constant, e referred to so far is not in fact equivalent to the electronic charge measured by experiment. It is referred to as the *bare* charge, e_0. Similarly the bare mass of the electron differs from that measured experimentally.

Consider further the coupling, e_0. This bare charge is modified by vacuum polarisation loops in the photon propagator as shown in figure 1.2(a), to produce the experimentally observed charge. Explicit calculation shows the relation between e_0 and the measured charge, e to be of the form [3]

$$e = e_0 \left(1 - \frac{e_0^2}{12\pi^2} ln \frac{M^2}{m^2}\right)^{1/2} + \mathcal{O}(e_0^4) + ... \tag{1.108}$$

where m is the mass of the electron and M is a cut-off parameter introduced to handle the divergence.

In order to see how this helps in eliminating the divergences mentioned earlier,

consider the scattering of electrons. The two lowest order Feynman diagrams are shown in figure 1.3. The matrix element of this process, to the order shown can be calculated using the Feynman vertex factor listed in table 1.2 in terms of e_0. This, as already mentioned, will result in a divergence associated with the loop. Now, the bare charge, e_0 is not a physical observable, thus for the matrix element to lead to an observable, it must be rewritten in terms of the measurable charge, e. The relation between the two charges is given by equation 1.108. Since, e is the charge the experimentalist measures, equation 1.108 must be specified at the particular value of the virtual photons momentum appropriate to the experiment, e.g. $Q^2 = \mu^2$. Thus inverting equation 1.108 to give e_0 in terms of e and then substituting for e_0 in the matrix element calculation will result in the splitting of the factor associated to the vacuum polarisation into two terms; one containing a loop at Q^2 and the other a loop at $Q^2 = \mu^2$. These two terms enter with opposite signs which leads to the cancellation of the divergence. This reparametrisation of the electronic charge is an example of *Renormalisation*. The difference of the two terms is such that the arbitrary cut-off parameter, M introduced in 1.108 is replaced by the parameter μ with dimensions of mass (known as the *renormalisation mass*). Of course μ is still arbitrary and different choices will lead to different expansions of the matrix element. Thus, although the matrix element is now finite, it must be independent of the value chosen for μ to be meaningful. Hence the matrix element dependence on μ must be cancelled by the μ-dependence of the charge, $e(\mu^2)$.

The single loop considered so far will be repeated in higher orders. The Feynman diagrams associated with these must all be summed in order to get an exact calculation. This leads to a geometric series in terms of the single loop calculation whose sum can be expressed (in the large Q^2 limit) as:

$$\alpha(Q^2) = \frac{\alpha(\mu^2)}{1 - \frac{\alpha(\mu^2)}{3\pi} ln\left(\frac{Q^2}{\mu^2}\right)} \tag{1.109}$$

where the coupling constant e has been expressed in terms of the commonly used fine structure constant, $\alpha(Q^2) \equiv e^2(Q^2)/4\pi$. Equation 1.109 describes the effect of

charge screening and $\alpha(Q^2)$ is referred to as the *running coupling constant.*

Higher order corrections play an important role in experimental analyses , particularly initial state radiation from the e^+e^- pair. The consequence of these is discussed in section 1.12.

1.11 Experimental Verification of Theory : Physics at LEP.

The theory discussed so far remains academic without experimental verification. The long established method of performing a scattering experiment is still the method used to do this. In modern experiments advances in accelerator technology have allowed much higher beam energies to be attained with a correspondingly better resolving power. This has been further aided with the advent of storage ring colliders in the 1960's (as opposed to a beam incident on a fixed target), where all the energy of both incident beams is available for particle production and where the centre-of-mass frame is the same as the laboratory frame of reference. The particle beams used as probes in these accelerators has varied from hadrons (i.e. pp, $p\bar{p}$) to leptons (i.e. e^-e^-, e^+e^-). Hadronic beams can facilitate large centre-of-mass energies, but the disadvantage here is that the collisions occur between constituent quarks in the opposing beams, thus the energy of the collision is only a fraction of the beam energy making it difficult to determine. Also collisions between 'spectator' quarks and gluons within the hadrons produces a very complex distribution of particles in the final state from which it is difficult to distinguish the primary interaction. Leptonic beams on the other hand produce relatively 'clean' final state particle distributions, due to their point-like nature. However, here the energy attainable in a circular storage ring is limited by synchrotron radiation, requiring the need for boosters to maintain the beam energy. This is especially true at LEP energies where the centre-of-mass energy is limited to 105 GeV [9].

For electron-positron beams, the beam particles annihilate into quantum states of well defined angular momentum. These correspond to the photon and the Z^0, which can decay into combinations of fermion and anti-fermion pairs. These may

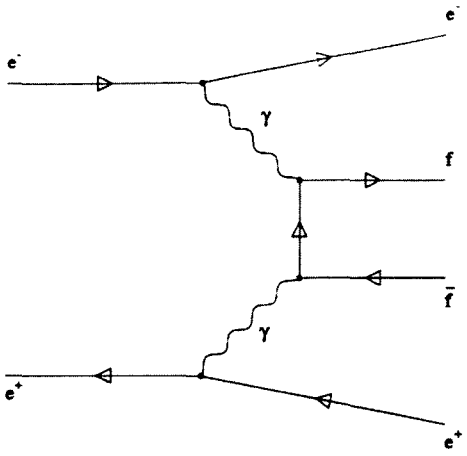

Figure 1.4: A two-photon event, where the beam particles radiate photons which combine to produce a fermion/antifermion pair in the final state.

be leptons or quarks; the latter being manifest by jets of hadrons in the final state. It is then possible to study, in a rather clean way, electroweak properties of the leptons and also processes such as fragmentation by which quarks materialise into hadrons.

Annihilation of e^+e^- beams is also accompanied by background processes such as e^+e^- scattering via t-channel photon exchange at low angles (i.e. Bhabha scattering) and two photon processes where photons radiated by the incident beams combine to produce fermionic final states (see figures 1.3 (a) and 1.4). The latter needs to be studied and corrected for in final analyses, but the t-channel scattering can be utilised since the process is theoretically well understood. Such events allow the determination of the beam luminosity and is in fact the method preferred by the ALEPH collaboration [10] (see section 2.10).

At LEP energies the annihilation cross-section is dominated by the Z^0 resonance, thus QED processes can be neglected. This allows precision studies of the Z^0 resonance and more generally the properties of the Standard Electroweak Model.

The high statistics already collected by the experiments at the LEP collider have allowed many aspects of the theory to be analysed. The mass, and width of the Z^0, and partial decay widths to quarks and leptons have all been well measured by LEP experiments [11]. It is also, now well established that the number of

neutrino species appears to be limited to three [1, 28]. Further analyses have included studies of QCD in hadronic Z^0 decay, and of heavy quarks, (in particular the b quark) and also searches for the elusive top quark and Higgs boson, along with more exotic particles such as those predicted by supersymmetric theories. Although nothing unexpected i.e. not accommodated by the Standard Model has been observed, various limits on phenomena have been established.

LEP itself is presently undergoing an energy upgrade which should take the available energy in excess of the W^+W^- pair production threshold of 160 GeV. This stage of LEP known as LEP200 will allow detailed study of the W gauge boson and vertices such a $W^+W^-Z^0$, in addition to searching for new physics.

1.12 The Physics of the Tau Lepton.

Since its discovery in 1975 at the SPEAR collider [12], it has been established that the tau is a sequential lepton making up the third generation of leptonic fundamental particles. However, its properties are still being investigated at various particle colliders throughout the world. The importance of the tau as a laboratory for precision tests of the Standard Electroweak Model is due to its large mass, ($1784.1^{+2.7}_{-3.6}$ MeV [8, 13]; a property unique over the other leptons. This permits the tau to decay via many modes, both leptonic and semi-leptonic. Indeed the large mass means that it has a very short lifetime [8] and thus the tau can only be reconstructed from its decay products.

A summary of the branching ratios to the main decay modes is given in appendix A. Here lies an intriguing puzzle causing much concern amongst physicists. It has been reported [14, 15, 19, 41] that for tau decays into one charged particle (i.e. 'one prong') with unobserved neutrals, the sum of the exclusive branching ratios is smaller than the inclusive topological one prong branching ratio. There has been much debate regarding this so called 'one prong problem' and whether the problem exists at all. Several collaborations suggest there is no problem [16, 17, 54], whereas others disagree [18].

Other properties of the tau also give insight into the present understanding of particle physics. For example, the assumption of lepton universality can be

examined by measuring the lifetime of the tau [62] and comparing it with that of the muon. The ratio of the lifetimes is related to the ratio of the couplings of the tau and muon to the $W^{\pm}$ vector boson, and their corresponding neutrinos, given by equation 1.110

$$\left(\frac{g_\tau}{g_\mu}\right)^2 = \left(\frac{m_\mu}{m_\tau}\right)^5 \frac{B_\tau^e}{B_\mu^e}\frac{\tau_\mu}{\tau_\tau} \tag{1.110}$$

where g_τ and g_μ are the couplings at the $\tau\nu_\tau W$ and $\mu\nu_\mu W$ vertices respectively, m_μ, m_τ, τ_μ and τ_τ are the masses and lifetimes of the muon and tau respectively. B_τ^e and B_μ^e are the branching fractions for the decays $\tau \rightarrow e\nu_\tau\bar{\nu}_e$ and $\mu \rightarrow e\nu_\mu\bar{\nu}_e$ respectively. Under the assumption of lepton universality both the tau and the muon must have the same coupling to the charged weak current. Substituting the Particle Data Group averages [8] into equation 1.110 yields a ratio which is several standard deviations from unity, disagreeing with lepton universality. The muon parameters entering equation 1.110 are well measured. Thus, the room for improvement lies with the tau properties. Indeed a more accurate measurement of the tau mass reported by collaborators at the Beijing Electron Positron Collider [13] (i.e. $1776.9^{+0.4}_{-0.5}$ MeV) reduces the number of standard deviations from unity, but still is not conclusive in verifying lepton universality.

The tau neutrino has never been directly observed, its presence is inferred from missing energy in the tau decay products. However, attempts have been made to measure its mass [19, 63, 64]. A non- zero tau neutrino mass has many theoretical implications relating neutrino oscillations and could provide explanations for problems such as 'dark matter' and the 'solar neutrino flux'. The best limits are obtained by studying the hadronic mass spectra of high multiplicity tau decays. The limit on the tau neutrino mass is then set by taking the difference between the tau mass and the end-point of the hadronic mass spectrum. Since the mass of the tau is known with relatively high precision [8], the accuracy in the neutrino mass is limited by the resolution of the effective mass determination. The value quoted by the Particle Data Group as measured by the ARGUS collaboration [20] of m_{ν_τ} <35 MeV at 95% CL will be reduced by the recent measurement of the tau

mass by the Beijing collaboration [13].

The tau permits tests of the Standard Electroweak Model. Although a lot of information may be gained from the asymmetries arising from the chiral nature of the weak interaction (see section 1.11.1 for further details), the current structure of the $\tau\nu_\tau W$ vertex can be tested by studying the momentum distributions of the final charged lepton in the leptonic decay modes of the tau. These spectra are parametrised by the Michel ρ parameter [21] which is dependent on the coupling at the $\tau\nu_\tau W$ vertex. Current measurements are in good agreement with the Standard Model value of 0.75 [22] with the V-A hypothesis.

1.12.1 Electroweak Interference Effects in Tau Production.

The cross-section for the production of $\tau^+\tau^-$ events from e^+e^- annihilations can be readily calculated at the lowest level (also known as the Born or Tree level), in terms of the leptonic current (1.39) and vertex factors developed in field theory (see table 1.2). For unpolarised e^+e^- beams, (i.e. averaging over e^+e^- helicities) and neglecting fermion masses (reasonable assumption at LEP energies) the cross-section reads [23]:

$$\frac{d\sigma}{dcos\theta} = (F_0 + P_\tau F_2)(1 + cos^2\theta) + 2(F_1 + P_\tau F_3)cos\theta \qquad (1.111)$$

where θ is the angle between the τ^- and the e^- beam directions, P_τ is the longitudinal polarisation of the τ^-, and the four form-factors are given by :

$$F_0(s) = \frac{\pi\alpha^2}{2s}(q_e^2q_\tau^2 + 2Re\{\chi_0(s)\}q_eq_\tau v_ev_\tau + |\chi_0(s)|^2(v_e^2 + a_e^2)(v_\tau^2 + a_\tau^2) \qquad (1.112)$$

$$F_1(s) = \frac{\pi\alpha^2}{2s}(2Re\{\chi_0(s)\}q_eq_\tau a_ea_\tau + |\chi_0(s)|^2 2v_ea_e2v_\tau a_\tau) \qquad (1.113)$$

$$F_2(s) = \frac{\pi\alpha^2}{2s}(2Re\{\chi_0(s)\}q_eq_\tau v_ea_\tau + |\chi_0(s)|^2(v_e^2 + a_e^2)2v_\tau a_\tau) \qquad (1.114)$$

$$F_3(s) = \frac{\pi\alpha^2}{2s}(2Re\{\chi_0(s)\}q_eq_\tau a_ev_\tau + |\chi_0(s)|^2 2v_ea_e(v_\tau^2 + a_\tau^2) \qquad (1.115)$$

and :

$$\chi_0(s) = \frac{s}{s - M_Z^2 + is\Gamma_Z^0/M_Z} \tag{1.116}$$

Here, $\sqrt{s}$ is the centre-of-mass energy of the e^+e^- beams, α the fine-structure constant, M_Z the mass of the Z^0 and Γ_Z^0 its linewidth. The q_e, v_e, a_e, q_τ, v_τ, a_τ are the charges and Z^0 coupling constants of the electron and τ respectively. The $\chi_0(s)$ term describes the Z^0 resonance in the lowest order Breit-Wigner approximation. (These terms will be modified at higher orders - see section 1.13).

The overall cross-section given by equation 1.111 can be factored into terms expressing the contributions from the different exchange processes , i.e. in terms of a pure QED cross-section, a pure weak cross-section and the interference term between the two. The lowest order QED cross- section is completely symmetric with respect to the τ production angle, θ, i.e. it contributes only terms in $(1+cos^2\theta)$ to equation 1.111. The symmetry of the cross-section is destroyed by the weak interaction and the interference term introducing a linear dependence on $cos\theta$. This is of course due to the chiral nature of the weak interaction and the reason why parameters of the Standard Electroweak Model can be tested experimentally, i.e. by observing the asymmetry in decay product distributions.

The forward-backward asymmetry is defined by :

$$A_{FB} = \frac{\sigma_F - \sigma_B}{\sigma_F + \sigma_B} = \frac{3F_1}{4F_0} \tag{1.117}$$

where σ_F and σ_B are the cross-sections in the forward and backward hemispheres respectively. The polarisation asymmetry is defined as :

$$A_{pol}^{FB} = -\frac{(1 + cos^2\theta)F_2 + 2cos\theta F_3}{(1 + cos^2\theta)F_0 + 2cos\theta F_1} \tag{1.118}$$

Here the polarisation asymmetry is combined with the forward-backward

asymmetry. Integrating 1.118 over all τ production angles results in the average longitudinal polarisation asymmetry :

$$A_{pol} = -\frac{F_2}{F_0} \equiv -P_\tau \tag{1.119}$$

At the Z^0 resonance, weak interaction effects dominate, thus pure QED and interference terms in the form-factors F_0,..,F_3 (equations 1.112 - 1.115) can be neglected. The asymmetries can then be expressed in terms of the vector (v_l) and axial-vector (a_l) couplings of the electron and tau to the Z^0. i.e. (assuming $a_l >> v_l$):

$$A_{FB} \simeq \frac{3}{4}\frac{2v_e a_e}{(v_e^2+a_e^2)}\frac{2v_\tau a_\tau}{(v_\tau^2+a_\tau^2)} \simeq 3\left(\frac{v_e}{a_e}\right)\left(\frac{v_\tau}{a_\tau}\right) \simeq 3(1-4sin^2\theta_W)^2 \tag{1.120}$$

and

$$A_{pol} \simeq \frac{-2v_\tau a_\tau}{v_\tau^2+a_\tau^2} \simeq -2\left(\frac{v_\tau}{a_\tau}\right) \simeq -2(1-4sin^2\theta_W) \tag{1.121}$$

where the ratio of the coupling vectors :

$$\frac{v}{a} = 1 - 4sin^2\theta_W \tag{1.122}$$

derived in section 1.6.2 has been used and lepton universality assumed in the case for the forward-backward asymmetry. From these relations it is apparent that although A_{FB} is easier to measure experimentally its usefulness to determine the vector/axial-vector coupling ratio is compromised by its quadratic dependence reducing the sensitivity of the asymmetry. Similarly, the polarisation asymmetry only has a linear dependence on the coupling ratio and therefore provides a more

sensitive measurement. However here the complication arises in explicit tau particle identification.

In analogy to the previous discussion, if the polarisation of particle, l is defined as :

$$P_l = \frac{2v_l a_l}{(v_l^2 + a_l^2)} \simeq 2(1 - 4sin^2\theta_W) \tag{1.123}$$

then the angular dependence of the τ polarisation asymmetry, equation 1.118 can be expressed as :

$$A_{pol}(cos\theta) = -\frac{P_\tau + \frac{2cos\theta}{1+cos^2\theta} P_e}{1 + \frac{2cos\theta}{1+cos^2\theta} P_e P_\tau} \tag{1.124}$$

Thus, provided sufficiently large amounts of data are available, information can be gained regarding the electron and tau couplings to the Z^0 (P_e and P_τ respectively.) independent of the lepton universality assumption.

1.13 Radiative Corrections.

As mentioned in section 1.10, radiative effects play an important role in analyses. The Born cross-section of equation 1.111 is not sufficient for the accuracies attainable at LEP energies. Thus, effects due to initial- state photon, final-state photon and final-state gluon radiation and vertex and propagator corrections need to be considered. Of these, the initial-state radiation produces the largest effect, since this process carries away energy, leaving the annihilation centre-of-mass energy below the nominal value [24]. As vertex corrections to the initial state and vacuum polarisation diagrams do not change the overall kinematics, their corrections enter as overall factors to change the scale of the cross-section. In the leading-logarithm approximation the vacuum polarisation diagrams can be easily summed to all orders as explained in section 1.9, but the vertex calculations are much more complicated [25]. On the other hand final state radiation effects can be summed

over since they have no effect on the centre-of-mass annihilation energy . This produces a correction of $1 + 3\alpha Q^2/4\pi$ to the overall cross-section.

The dominant effects of these corrections can be compensated for by replacing parameters by *running* or *effective* parameters as in the case of the fine-structure constant of equation 1.109. This then results in an *Improved Born Approximation.*

Thus, in terms of the fine-structure constant, $\alpha(s = 0)$, the Fermi- coupling, G_F, and the mass of the Z^0, M_Z (which are all well measured [8]), it is possible to express the weak mixing angle θ_W as [23] :

$$sin^2\theta_W = \frac{1}{2}\left(1 - \sqrt{1 - \frac{4A_0^2}{M_Z^2}}\right) \tag{1.125}$$

where

$$A_0 = \left(\frac{\pi\alpha}{\sqrt{2}G_F}\right)^2 \tag{1.126}$$

The leading order radiative corrections are then incorporated by making the replacements :

$$\alpha(M_Z^2) = \frac{\alpha}{1 - \Delta\alpha} \tag{1.127}$$

where $\Delta\alpha$ includes effects due to the leading order vacuum polarisation diagrams in the photon propagator (see equation 1.109) [24, 25].

Also, the normalisation of the ratio of the weak neutral current to the weak charged current, ρ becomes modified to :

$$\rho = \frac{1}{1 - \Delta\rho} \tag{1.128}$$

where the leading order term in $\Delta\rho$ is :

$$\Delta\rho = \frac{3G_F m_t^2}{8\pi^2\sqrt{2}} \tag{1.129}$$

and shows how the mass of the yet undiscovered top quark, m_t enters the theory. Thus, $sin^2\theta_W$ becomes redefined as the *effective* $sin^2\theta_W$ (i.e. $sin^2\bar{\theta}_W$), which now has an explicit dependence on the centre-of-mass energy, i.e.

$$sin^2\bar{\theta}_W = \frac{1}{2}\left(1 - \sqrt{1 - \frac{4A_0^2}{\rho M_Z^2}\frac{1}{(1-\Delta\alpha)}}\right) \tag{1.130}$$

and

$$\frac{M_W^2}{M_Z^2} = \rho cos^2\bar{\theta}_W \tag{1.131}$$

(c.f. equation 1.104), where the Born level mixing angle is related to the effective angle by :

$$sin^2\bar{\theta}_W = sin^2\theta_W + \Delta\rho cos^2\theta_W \tag{1.132}$$

Thus, an experimental measurement of the effective weak mixing angle, $sin^2\bar{\theta}_W$ allows constraints to be put on the masses of the Higgs boson and top quark.

Vertex corrections are summarised in terms of s-dependent vector and axial vector form factors. Thus, the cross-section for tau pair production becomes modified by replacing the lowest order Z^0 Breit- Wigner resonance by :

$$\chi_0(s) \rightarrow \chi(s) = \frac{1}{4sin^2\theta_W cos^2\theta_W}\left(\frac{s}{s - M_Z^2 + is\Gamma_Z/M_Z}\right) \tag{1.133}$$

Chapter 2

The Aleph Detector.

2.1 The Large Electron - Positron Collider (LEP).

The Large Electron - Positron Collider was constructed to operate in conjunction with existing facilities at the European Centre for Particle Physics (CERN), near Geneva, Switzerland. It was designed to produce collisions of electrons and positrons at energies upto a maximum of 110 GeV in the first instance, (this stage is known as LEP100), later to be upgraded to a maximum energy of 200 GeV in the mid-1990's (stage known as LEP200). Thus, the initial energy limit will concentrate on the neutral weak intermediate vector boson, Z^0 production threshold and thus act as a Z^0 factory.

The LEP 'ring' is not quite circular, comprising of eight straight sections to minimise synchrotron radiation. At four symmetrically opposite points along these straight sections are positioned the interaction points and detection apparatus, called ALEPH, DELPHI, OPAL and L3. The whole of the collider is situated under the earth's surface, inclined by 1.42% for geological reasons. It has a diameter of 4m and a nominal circumference of approximately 27km, straddling the France -Switzerland border.

The electron and positron beams are systematically accumulated upto the required beam energy via smaller, already existing, accelerator and storage systems. The beams are produced by a linear accelerator from which they are fed in turn into the Proton Synchrotron and Super Proton Synchrotron storage rings before

eventual injection into LEP.

LEP has an initial design luminosity of $1.6 \times 10^{31} cm^{-2} s^{-1}$, to be achieved by operating the beams with four bunches of electrons and positrons each. Attempts to increase the luminosity by using eight bunch beams have been made during operation in 1992, along with attempts to produce polarised beams, but with limited success [27].

LEP commenced operation in August 1989; a total integrated luminosity of about $20 pb^{-1}$ having been measured by ALEPH by the end of data taking in 1991. This corresponds to approximately half a million Z^0 decays, produced over a range of beam energies scanning the Z^0 resonance [28].

The ALEPH detector is situated in a cavern at interaction point 4 near the town of Echenevex in France. This huge hall housing the detector is 70m long in the radial direction of LEP, 21.4m wide in the beam direction and 16m high. The floor of the hall is some 143m below the earth's surface and 6m below the LEP beam line.

The ALEPH collaboration comprises of 30 institutes from Europe, America and Asia.

2.2 The ALEPH Detector Overall.

Aleph is a hermetic detector with an overall cylindrical symmetry of dimensions 12m diameter x 11m length when fully closed and ready for data taking. Two cross-sections through the centre of the detector are shown in figure 2.1.

The lower figure is along the length of the beam-pipe and the upper is perpendicular to the beam. The details of each sub- component are described in the sections that follow.

The main detector can be sub-divided into two component types; tracking devices encountered first by particles emerging from the interaction point, surrounded by calorimeters. Of the trackers, closest to the beam-pipe is a Minivertex Detector (VDET) made of silicon microstrips, measuring the position of charged tracks to a precision of $10 \mu m$. Surrounding the VDET is a conventional drift chamber with axial wires (running along the z-direction), called the Inner Tracking Chamber

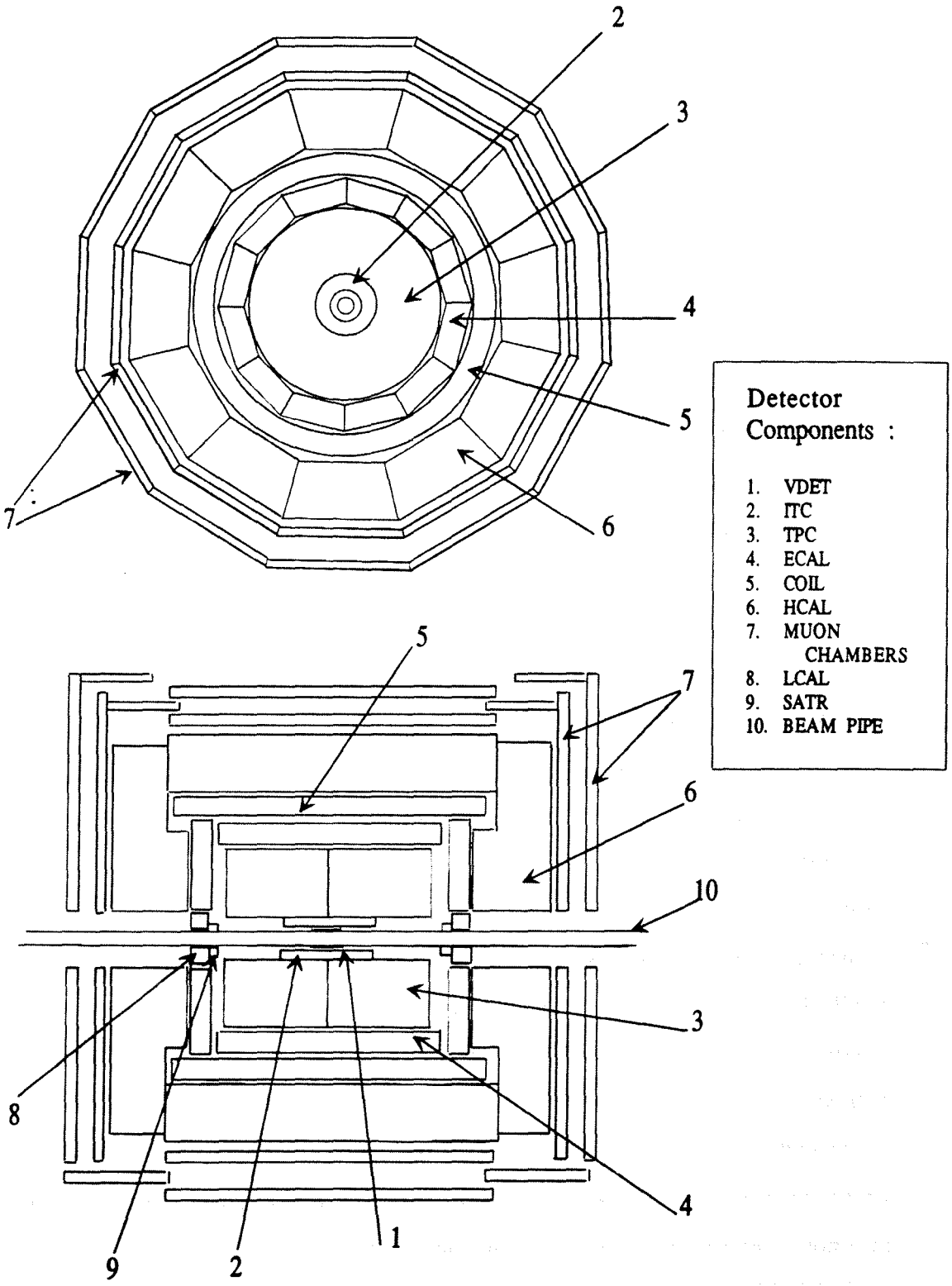

Figure 2.1: Cross-sections through the ALEPH detector.

(ITC). The ITC covers a radial region from 13cm to 29cm and extends over 1m either side of the interaction point. Up to 8 coordinates per track are provided with an accuracy of 100μm. This sub-component in turn is surrounded by the main tracking device, namely the Time Projection Chamber (TPC) with an overall diameter of 3.6m and 4.4m length. The TPC provides three-dimensional coordinates for each charged track segment, giving a precise measurement of the transverse momentum of a charged particle. It also contributes to particle identification through measurements of energy loss (dE/dx).

Beyond the TPC is the first of the calorimeters; the Electromagnetic Calorimeter (ECAL), designed to detect mainly electrons and photons via their interactions with lead sampling layers interleaved with layers of proportional tubes. The ECAL has a highly segmented projective tower structure, designed to optimise resolution in polar and azimuthal angles, θ and ϕ. (The resolution is approximately 1^0 in both these angles). The ECAL has a nominal thickness of 22 radiation lengths, and comprises of a central dodecagonal barrel closed at both ends by end -caps.

The 1.5T magnetic field used to bend charged particle trajectories is provided by a superconducting solenoid surrounding the ECAL barrel. The magnetic field is shaped by the iron layer components of the hadron calorimeter (HCAL), the next sub-component radially outwards. Strongly interacting particles are detected by limited streamer tubes interleaved with the iron layers. The HCAL also has a projective tower structure arranged into a central barrel closed by end-caps. The digital output of the tubes allows identification of muons due to their characteristically high penetration. A double layer of limited streamer tube chambers placed outside the HCAL and comprising the outermost detector components , further aids the measurement of the position and angle of these muons.

In addition to the detector components designed to detect the e^+e^- annihilation products, described above, are detector elements whose purpose is to measure the luminosity at the Aleph interaction point. This is done via the detection of small angle Bhabha scatterings. Collectively these elements are known as the Luminosity Monitors. They consist of a calorimeter very similar in design to the ECAL (known as the LCAL), a Small-Angle Tracker (SATR) made of layers of drift-tube chambers and a very small angle calorimeter (the BCAL). A combination of one LCAL,

SATR and BCAL, representing one half of the main luminosity monitor is situated along the beam-pipe on either side of the interaction point at a distance of $z \simeq \pm 2.7$m.

2.2.1 The Beam-Pipe.

For the 1989 and 1990 running periods, the beam-pipe was made of an aluminium (96%), magnesium (3.2%) alloy. It had a diameter of 156mm and a thickness of 0.5mm. In 1991 this was replaced by a smaller diameter (105mm) beryllium pipe allowing the VDET to be instaled closer to the interaction point.

2.3 The Electromagnetic Calorimeter.

Any attempt to accurately detect electromagnetically interacting particles such as electrons and photons requires a detector which combines good spatial and energy resolution while covering as much of the solid angle around the interaction as possible. Obviously ideal calorimeters can be imagined but in practice a compromise between the various contributing factors has to be found. Such factors include mechanical construction and geometrical design restrictions. Also, for any project with a finite budget cost plays an important role.

To this end the Aleph collaboration has opted for a lead/wire-chamber sampling device with an essentially cylindrical design, comprising of a central barrel surrounding the TPC, (but within the solenoid), closed at both ends by end-caps. The calorimeter has a nominal thickness of 22 radiation lengths (X_o), and covers 3.9π sr of the solid angle. Resolution is obtained by segmenting the calorimeter into small (approximately 30x30 sq.mm) cathode pads, connected internally to form 'towers'. These towers have a projective geometry, so that each one points to the interaction point, and signals are read-out in three depth sections ('storeys'), equivalent to the first 4, the middle 9, and the last 9 radiation lengths (as measured from the interaction point). In this way an energy resolution $\Delta E/E$ of $18\%/\sqrt{E}$ + 1.7% is obtained.

The overall dimensions of the calorimeter mean that it is mechanically diffi-

cult to construct it as three whole sub-components (i.e. barrel and two end-caps). Therefore, each sub-component is further divided into twelve modules, subtending an azimuthal angle, ϕ of 30°. When these modules and sub-components are put together to make up the overall calorimeter, regions where they join (termed 'cracks') will allow particles to pass through undetected reducing the efficiency of the detector. The modules in the end-caps are rotated by 15° in ϕ with respect to the modules in the barrel to prevent overlapping of the crack regions, but cracks still represent 2% of the overall barrel surface and 6% of the end-cap surfaces.

2.3.1 The Sampling Calorimeter

Radially the ECAL comprises of 45 layers of lead/proportional wire- chamber. The wire-chamber layers are made up of open-sided aluminium extrusions with $25\mu m$ diameter gold-plated tungsten wires running along the centre. The open faces are closed by copper cathode pads behind a resistive graphite coated Mylar 'window'.

When a high energy electron or positron incident on the lead layers interacts, the dominant energy loss is due to bremsstrahlung. For incident photons the dominant absorption process is pair production. Thus, the initial particle will, via these two processes, lead to a cascade of $e^{\pm}$ pairs and photons. The resulting 'shower' will be predominantly in the longitudinal direction, but will be subject to some transverse spreading due to multiple coulomb scattering and the transverse momentum of the produced particles. Before the cascade terminates the secondary $e^{\pm}$ pairs enter the proportional wire- chamber where the electrons drift towards the anode wires thereby gaining energy. If this gain exceeds the ionisation energy of the gas, then further ions are produced and a chain of such processes leads to an avalanche of electrons and positive ions. The electrons induce negative pulses on the anode wires while the positive ions induce pulses on the cathode pads.

In the ALEPH ECAL the pads from consecutive layers are connected to form 'towers' and the measured signals are summed in three depth sections; the first 10 layers of 2mm lead sampling ($\simeq 4X_o$, known as the 'first storey' of an individual tower or the 'first stack' of a module), the next 23 layers of 2mm lead sampling ($\simeq 9X_o$, the second storey/stack) and finally the remaining 12 layers of 4mm lead

sampling ($\simeq 9X_o$, the third storey/stack).

In addition to signals measured by the cathode pads, within a module the signals measured by each anode wire plane is also read out. Consequently , along with the good angular granularity provided by the cathode pads (essential for rsolving overlapping showers from several particles), the ECAL facilitates good longitudinal sampling of showers which is particularly useful for discriminating between electromagnetic and hadronic particle clusters, as the latter tend to deposit energy closer to exiting the ECAL rather than within the first two stacks as is the case for electromagnetic particles.

2.3.2 Ecal Sub-components.

The Barrel.

Each of the twelve modules weighs 10.4 tonnes and is sub-divided into 32 x 128 i.e. 4096 towers. In each of the 45 cathode layers, the segmentation is constant in ϕ (i.e. 32 rows), but the width in θ increases with increasing distance from the centre of the barrel, ensuring the transverse width of the towers match the shower size. Thus, the face presented by each tower to the interaction point has dimensions of $\Delta\phi = 0.94^0$ in azimuth and $\Delta\theta = 0.93^0 x sin\theta$ in the polar direction.Towers at the ends of the modules nearest the end-caps are 'cut-off' due to their projective design, as the remainder of these towers are in the end-caps.

Since read-out is in three storeys there is a total of 12288 channels per module from the cathode pads and 45 channels per module from the anode wire planes.

The End-caps.

These modules each weigh 2.6 tonnes. There are 1024 towers per module and therefore 3072 cathode pad channels in addition to the 45 wire plane channels.

The geometrical shape of the petal modules necessitates a non-trivial cathode pad segmentation [10]. In θ segmentation is designed so that the projected length of a pad onto the normal to the line joining the centre of the pad to the interaction point is the same for all pads. The projected size is such that end-cap pads in the overlap regions coincide with those equivalent pads in the barrel allowing a con-

tinuous tower structure. Pad rows are orthogonal to the petal sides, consequently there is a 30^0 bend on the centre line of each module. There is equal segmentation in ϕ with the number of pads across the petal increasing with increasing θ.

2.3.3 The Ecal Gas.

The wire-chamber layers in both the barrel and end-caps, are filled with a mixture of 80% Xenon + 20% CO_2, which is maintained at 60mbar above atmospheric pressure. It is important to maintain the purity of the gas in order to provide a constant gain. Each barrel module and every second end-cap module therefore has a small single-wire chamber (3.5x20.0 mm^3) containing a ^{55}Fe source to monitor the purity of the gas. (These wire-chambers are also known as 'platines'). The characteristic 6keV X-ray from the ^{55}Fe source is measured by the wire, and thus allows the overall gas gain to be monitored. The gas system (which controls the mixing, distribution, circulation and purification), keeps the fractional content of the Xenon gas to 80 $\pm$ 1%.

2.3.4 Ecal Calibration.

The primary aim of the calibration was to determine the relationship between the energy deposited and the charge collected by the front-end electronics. This could only be done experimentally. During data taking it is important to monitor the calibration for variation with time and to correct for any malfunctioning channels.

The procedures adopted was to determine the electromagnetic energy deposited from primary electrons and photons; a different set of calibration constants apply to energies deposited by hadrons or muons.

The methods used sub-divide as follows:

(i) Absolute calibration using test beams of electrons and photons of known energy. This was carried out prior to commisioning of ALEPH on several (but not all) of the ECAL sub-components. The beams were directed within a pre-defined fiducial region on each module. Within this region the response of the 10x10 pad towers immediately around the beam impact point (i.e. 300 channels) was measured by fitting the observed energy spectra (corrected for all pedestals

etc.) with a gaussian to determine the mean energies.

(ii) Relative calibration between modules. This calibration was also principally used before the start of LEP. The technique involved temporarily injecting radioactive ^{83}Kr gas into the Xe/CO_2 gas mixture of each module. The ^{83}Kr emitts characteristic 9.4keV X-rays. Parameterising the decay spectra measured by the wire planes allowed the response of each module to be quantified. Before an accurate comparison of parameters between modules could be performed, corrections for differences in gas gain and high voltage were applied (see section 2.3.3). This technique was also used to check the uniformity of response over the surface of a module.

Factors Influencing Calibration Accuracies

Of course all the modules do not have identical gas gains or applied high voltages. These potential sources of systematic uncertainty were compensated for by using the inter-calibrated ^{55}Fe test cells (platines). The essential factor governing the variation of gas gain with density, i.e. the ratio of the pressure to the temperature, p/T, is the exponent of this ratio. A similar exponent characterises the gain dependence of the common high voltage applied to the platines and the anode wire layers. The experimental determination of these exponents for each module and its corresponding platine allowed correction factors to be applied.

Another factor which required careful consideration (not only during calibration, but also during data taking) was the absorption of the Xe/CO_2 gas into the graphite layers of the modules, resulting in a gradual fall in gas density. Studies have shown [10] that over a typical LEP fill period of $\sim$6 hours the density drift is typically $\leq$0.6% for modules with gas filled for more than one week. The platines can monitor deviations of up to 10% in gain. The gain drifts are corrected by injecting small amounts ($\simeq$1mb per day per module) of fresh Xe/CO_2 gas. Tests have also shown that a gain stability of $\pm$1% can be achieved over a 10 day period.

Finally, factors which also effect calibration accuracies are mechanical construction details (minimised during manufacture) and gains in the electronics involved in the read-out system.

Calibration after Installation in LEP and Resolution.

After commisioning the initial operating conditions were determined using the ^{83}Kr gas technique and the energy scales were set using the modules from the test beam measurements. Once data taking was underway and a suitable sample of wide-angle e^+e^- Bhabha events were available, this sample was used to check the energy calibrations performed prior to commissioning. It was found that for the electrons from these events (with mean energy of 45.6 GeV) the spread was $\pm$5.5 % compared with a Monte-Carlo prediction of $\pm$3.0%. These bhabha events were also used to fine tune the relative calibration constants.

The test beams used for the absolute calibration of modules (see section 2.3.4) also deduced the resolution available in both energy and space coordinates. The energy resolutions (i.e. $\pm\Delta$E/E) obtained after all corrections were $16\% + 1.7\%/\sqrt{E}$ for the wires and $17\% + 1.9\%/\sqrt{E}$ for the pads. The electron energy deposits, from the test beam, in the four leading towers were used to determine the θ and ϕ coordinates of the shower barycentre. By comparing these coordinates with the hit coordinates of the incident particles and fitting a gaussian to the resulting distribution, a spatial resolution of $6.8\text{mmGeV}/\sqrt{E}$ was determined.

2.4 The Time Projection Chamber.

The detector sub-component central to the reconstruction of charged tracks is the Time Projection Chamber (TPC). This is a drift chamber that provides spatial information in three dimensions, as well as measurements of energy loss via ionisation (i.e. dE/dX) for particle identification.

The essential feature of a TPC is that the electric field in the chamber is parallel to the magnetic field. This arrangement reduces diffusion of electrons in the gas because the magnetic field forces the drifting electrons to wind around the field lines. As a consequence, the electrons can drift over a long distance and still provide good spatial resolution.

The Aleph TPC has a cylindrical geometry being composed of an inner field cage of diameter 0.6m and an outer field cage of diameter 3.6m; the overall length

being 4.4m. The two coaxial cylinders are closed at both ends by end-caps incorporating drift chambers, and divided in two by a central membrane. A charged track emerging from the interaction point has its trajectory spiralled by the 1.5T magnetic field applied parallel to the z-axis. The central volume (known as the 'active volume') between the two end-caps contains a non-explosive gas mixture of 91% argon and 9% methane, it contains no sense wires. The central membrane is held at a potential of -27kV and the two-caps are held at ground potential, consequently the electric field is directed in opposite directions along the z-axis in the two halves of the chamber. The uniformity of the electric field is maintained by applying potentials to electrode bands covering the curved surfaces of the field cages.

Electrons produced by ionisation of the gas in the active volume by a traversing charged particle are drifted to one end-cap where they encounter three layers of wires; first a gating grid, secondly a layer of cathode wires and finally a sense/field wire layer. It is necessary to carefully shape the electrostatic field in order to eliminate track distortions. Thus, the cathode wires focus the drifting electrons towards the sense wires and the field wires located between the sense wires improve the uniformity of the electrostatic field by reducing 'cross-talk' among neighbouring sense wires due to the motion of positive ions.

The ionisation avalanches induced by the drifting electrons around the sense wires result in the formation of positive ions which migrate towards the central high-voltage electrode. Thus, the purpose of the gating grid is to block the passage of positive ions into the drift volume, while also being capable of allowing drifting electrons to pass through. This is achieved by operating the gating grid in one of two modes; 'open' or 'closed'. In the open state the same negative potential is applied to all the gate wires, thus rendering it transparent to charged particles. By applying a higher potential to alternate wires in this grid, dipole fields can be set up across the wire plane, thus making it opaque to the passage of charged particles. So, switching this grid between the 'open' and 'closed' states, synchronous with the bunch crossing, reduces effects from space charges in the drift volume.

2.4.1 Measuring the Track Kinematics and Particle Identification Capabilities.

The trajectory of a charged particle can be reconstructed by using the distribution of sense wire hits, the drift times to the sense wires, and the charge distribution on cathode pads capacitively coupled to the sense wires. The Aleph TPC pads have dimensions of 6.2mm x 30mm in the $\delta(r.\phi)$ x δr directions respectively with an azimuthal pitch of 6.7mm. The outer 12 sectors in each end-cap have 12 pad rows while the inner sectors have 9 pad rows arranged in concentric circles around the z-axis. In between these rows are long, circular 'trigger' pads, on which the second-level trigger is based (see section 2.4).

Measurement of the drift time, along with the known drift velocity allows easy calculation of the z-coordinate. The $r\phi$ coordinate is calculated from the signals induced on the precisely located cathode pads and the radial positions of these pads immediately gives the r coordinate. Consequently, for tracks passing through both the inner and outer field cages, the TPC is capable of providing 21 three dimensional points.

The sagitta of the arc projected onto an end-plate from he helix of a track from the interaction point, allows the radius of curvature of the arc to be calculated. This information, combined with the known magnetic field producing thetrack curvature, then gives the component of the track momentum perpendicular to the magnetic field.

Particle identification is achieved by measurements of enrgy loss, i.e. dE/dX, from the signals induced on each sense wire and cathode pad by a track. the measured mean ionisation is compared to that theoretically expected for various hypotheses of particle type. The hypothesis resulting in the lowest χ^2 value is then assigned to the track.

2.4.2 Calibration.

A system of lasers and beam splitters is used to calibrate the TPC. Two lasers placed above the Aleph detector have their beams guided to the outside of the inner TPC field cage where a system of splitters create 30 straight ionisation

tracks. The level of gas contamintion present in the argon-methane mixture is sufficient to produce these ionisation tracks. The tracks are arranged to originate approximately from the interaction point at differing polar angles. The measured curvature of these tracks (ideally they should have no curvature!) is used to correct the sagitta of real particle tracks, thus eliminating any systematic effects from field inhomogeneities contributing to the momentum resolution. The drift velocity is determined from the reconstructed polar angles of the thirty tracks.

2.4.3 Resolution.

The resolution in the transverse momentum component is proportional to the resolution in the measurement of the sagitta, which is governed by the accuracies involved in determining the track coordinates. Contributing factors include the angles of the track segment with respect to the wires and pads (the 'angular wire/pad effects'), the magnetic field, diffusion effects, electronic noise, digitisation and errors in the calibration.

The performance of the Aleph TPC was studied extensively using a scaled test model of 90cm diameter and 130cm drift length [29] . From these studies an $r\phi$ spatial resolution of 160 μm at 0^0 pad crossing angle and 400μm at 10^0 pad crossing angle; and a resolution of $\simeq$1 - 2mm in z was measured. These, then translate into a momentum resolution of $\Delta p/p^2 \simeq 1.2 \text{ x } 10^{-3}$ (Gev/c)$^{-1}$.

For a charged track crossing 280 wires, the dE/dX resolution was determined to be 4.5%.

An important point to note is that the error on the transverse momentum is dependent on the polar angle of the track, since a track at large $|cos\theta|$ is measured with less points and a smaller lever arm is available to determine the sagitta.

2.5 The Inner Tracking Chamber.

The Aleph Inner Tracking Chamber (ITC) is a conventional multiwire drift chamber consisting of sense and field wires strung parallel to the z- axis (also the beam direction). In addition to providing information for track reconstruction, it also

provides tracking information for the Level1 trigger.

The cylindrical ITC has an inner radius of 12.8cm and an outer radius of 28.8cm with an overall active length of 2m. The wires are strung between aluminium end-plates in concentric layers. There are 8 layers (a total of 960 wires) separated into two sets of four; the inner layers each comprising of 96 sense wires and 144 wires making up each of the outer layers. Each pair of layers is separated by a layer of guard wires. Individual sense wires are surrounded by six field wires arranged in a hexagonal drift cel; four of the wires being shared by neighbouring drift cells on either side. One of the field wires in each cell is insulated from the end-plates. this allows a calibration pulse to be injected into the chamber. The sense wires are operated at a positive potential in the range 1.8 - 2.5 kV and the field wires are kept at ground potential.

To eliminate 'left-right' amgiguities in track fitting each consecutive drift cell layer is off-set by one half cell, so that the cell configuration , when viewed from the end-plates has a 'close packed' structure.

The wire load is taken by the outer cylinder made of carbon fibre. The thin (2mm) inner cylinder is made of polystyrene. Both cylinders are coated with thin layers of aluminium foil on the inner and outer surfaces. This provides electrical screening against RF interference, with the added advantage of making the boundaries of the chamber into an equipotential surface, thus improving the uniformity of the electric field inside the ITC.

The ITC is capable of operation with either of two gas mixtures; 50% argon and 50% ethane or 80% argon and 20% carbon dioxide.

Track Information.

The ITC can accurately provide upto eight points in $r\phi$ coordinates for tracking. These coordinates are determined by measuring the drift time taken by the electrons liberated in the ionisation of the gas mixture by the passage of a charged track. The z coordinate is determined from the difference in time-of-arrival of pulses at the two ends of the sense wires. From test beam data the efficiency in the $r\phi$ coordinate was found to be 98.2% at a sense wire voltage of 2.3 kV and

98.0% at 2.2 kV; these efficiencies both being independent of the distance from the sense wire. The z coordinate efficiency exhibited a much stronger voltage dependence, it being in the range 95.6% - 97.6% at 2.3 kV and between 86.3% and 97.9% at 2.2 kV.

The resolutions of the coordinates measured in the same test beam showed a variation as a function of distance from a sense wire in $r\phi$ and distance along a wire in z. However, the average values were approximately 100μm in $r\phi$ and 3cm in z.

In order to use ITC information for the Level 1 trigger a rapid decision needs to be made on what is detected. The decision speed is partly determined by the maximum drift time taken. Consequently, the drift cells were kept small; the discontinuity between the four inner and four outer layers meant that the first layer of the outer set has the smallest drift cells, whilst the last layer of the inner set has the largest cells.

Two processors provide tracking information in either the $r\phi$ projection or in all three $r - \phi - z$ dimensions, for the Level 1 trigger in less than 3μs.

The momentum resolution obtained when the ITC is used in conjunction with the TPC is $\Delta p/p^2 \simeq 0.8$ x 10^{-3} (Gev/c)$^{-1}$.

2.6 The Hadron Calorimeter.

This sub-component of the Aleph detector was designed to serve two essential purposes; the first to act as a calorimeter for the passage of hadrons and the second to act as the return yoke for the magnetic field produced by the superconducting coil. Since it encloses the superconducting coil and all the other sub-components of Aleph closer to the interaction point, it also serves as the main structural support.

To this end the basic structure makes use of layers of iron interleaved with layers of streamer tubes. the overall geometry is similar to that of the electromagnetic calorimeter (ECAL, see section 2.3) in that it comprises of a barrel and two end-caps, arranged in an overall dodecagonal shape.

The twelve modules of the barrel are each sub-divided into two mirror halves. In depth each module has 22, 5cm thick, iron slabs, plus an outer slab of 10cm.

To maintain the rigidity of the structure iron bars are welded along the edges of each iron slab. The 22 layers of gaps produced in this way are filled with streamer tubes, with one extra layer of tubes being placed in front of the first layer. Thus, the total thickness of iron is 1.2m, which represents 7.16 interaction lengths for a perpendicular incident hadron. The overall length of a barrel module is 7.24m, but small sections of the iron slabs are cut away at both ends to allow cables from the inner detector sub-components to pass through. Also, there is an additional hole in the uppermost module to allow for the plumbing necessary for the superconducting coil.

The streamer tubes are made of PVC extrusions, comprising of eight cells per tube, with the inner surface painted with graphite and a 100μm diameter wire running along the centre. The gas used is a mixture of argon (12.5%), carbon dioxide (56.5%) and isobutane (30%). The streamer tube cells are closed by copper pads connected to form projective towers as in the ECAL (see section 2.3). Each half module in the barrel has a width ranging four towers of equal angular dimension in azimuth. The lengths of the towers in the polar direction are kept constant by making them proportional to $1/(cos^2(90^0 - \theta_{polar}))$. Thus, there are 2688 towers fully contained within the barrel and 768 are in the overlap regions. On the whole the tower arrangement matches that of the ECAL with one HCAL tower corresponding to about 14 ECAL towers.

On the flat side of each PVC streamer tube extrusion (i.e. the face opposite to the cathode pads) is placed an aluminium strip, 4mm wide and running the length of the tube. This is used to provide a signal to indicate whether a streamer tube has been fired. This information along with the signals induced on the cathode pads allows a two-dimensional picture of the hadronic shower to be built up. This is crucial to allow discrimination between hadrons and muons. Unlike the ECAL, there is no direct signal readout from the anode wires.

The end-caps of the HCAL each have six petals, with an overall dodecagonal shape. Since these have a flush fitting with the barrel, they have a fewer number of iron slabs in the overlap regions than in the region closer to the beam pipe. Thus, in the overlap regions there are 16 iron layers (15 x 5cm + 1 x 10cm) and 23 layers (22 x 5cm + 1 x 10cm) in the central region of each petal. Since the end-

caps experience huge magnetic forces (which also pull both end-caps in towards the interaction point) and also to keep the spacing between iron layers at 22mm for the streamer tubes, five iron bars are welded across each layer parallel to one straight edge of the petal. Streamer tubes are fitted in the four sections produced in this way. As with the ECAL end-caps, the tower structure is such that there is correct projection of towers from the barrel into the end-caps in the overlap regions.

2.7 The Magnet System.

The magnetic field required by the tracking detectors is produced by a superconducting solenoid placed in between the electromagnetic and hadron calorimeters at a mean radius of 2.65m. The passive iron layers of the HCAL (see section 2.6) serve as the return yoke of the field. The superconducting coil is suspended fron the barrel of the HCAL and itself carries the weight of the ECAL and TPC.

2.7.1 Superconducting Coil.

The solenoid was designed so as to minimise the radial space occupied by the coil and cryostat system and also to minimise the radiation thickness of materials presented to particles passing through.

The solenoid consists of a main coil made of a single layer of NbTi superconductor wound uniformly over the whole length of the barrel section of Aleph (i.e. 1712 turns over 6.4m). At each end of the main coil is a compensating coil made of two short sections (each 18.8cm long) of superconductor winding. The main coil is operated at a nominal current of 5000A and the compensating coils each at 1000A. Both the main and compensating coils are tightly bonded to a common, thick aluminium alloy cylinder; the main coil being bonded to the inside surface of the cylinder and the compensating coils on the outside surface.

This overall solenoid construction is cooled by means of a double array of circular pipes welded onto the outside surface of the aluminium alloy support cylinder and connected in parallel to manifolds for liquid helium distribution and

circulation. This coil assembly is mounted in a cryostat, essentially comprising of an annular vacuum tank made of two circular aluminium alloy shells, connected at both ends to thick stainless steel flanges. A thermal shield cooled at a temperature of 70K surrounds the coil within the vacuum tank. Superinsulation is placed between the shield and the walls at room temperature.

2.7.2 Field Characteristics.

The combined arrangement of superconducting solenoid and iron return yoke produces a magnetic field of 1.5T at optimum operating conditions. The energy stored in this state is 140MJ.

Careful measurement of the magnetic field using an assembly of Hall plates and nuclear magnetic resonance probes was performed prior to commissioning [30]. It was found that the main field component (i.e . in the z direction) had a uniformity t6o the level of 0.2%. However , some variations in the transverse field components in radius and azimuth were observed. These were such that the distortions induced in the sagitta of a track measured by the TPC are less than 0.2mm. But, these distortions are not severe as they can be compensated for using the TPC calibration system (see section 2.4.2).

2.8 The Muon Chambers.

The muon chambers are essentially two double layers of streamer tubes positioned outside the HCAL components (and hence are the outermost sub- components of the Aleph detector). The chambers are divided into modules which follow the dodecagonal arrangement of the barrel region. The end- cap muon chambers are subdivided into four irregular quadrants, which when combined around the beam pipe produce the dodecagonal shape of the HCAL end-caps. In the region between the barrel and end-cap layers (due to the thickness of the HCAL) there are middle-angle chambers to cover the overlap region.

Signals induced by passing muons are read out from strips positioned on both sides of each streamer tube layer. On one side the strips, 4mm wide at a pitch of

10mm, run parallel to the anode wires (the x-strips), and on the other side, strips with a width of 10mm and 12mm pitch run orthogonal to the wires (y-strips). The two tube planes in a double layer are staggered such that the x-strips are off-set by 5mm and the y- strips by 6mm, thus allowing full detection efficiency and improving spatial resolution.

The muon chambers merely serve the purpose of tracking charged particles without any measurements of energy. Thus there is no calorimetric read- out via cathode pads as in the case of the HCAL.

The two double layers are separated by 50cm in the barrel region and 40cm in the end-caps. This arrangement allows track directions to be determined with an accuracy of 10-15 mrads.

2.9 The Minivertex Detector.

During data taking in 1989 and 1990 the minivertex detector (VDET) was not operating. Prototypes were tested during this period before successful commissioning and operation during 1991. However, since in 1991, Aleph also had a new beam pipe installed with differing dimensions (i.e. a reduction in diameter from 15.6cm to 10.5cm), the VDET also had to be redesigned to fit closer to the interaction point. Of course this was to the advantage of the VDET's performance, in that a better spatial resolution could be obtained.

The VDET consists of two concentric layers of silicon wafers surrounding a 20cm length section of the beam pipe. The inner layer, at a radius of 6.3cm, comprises of 9 modules (i.e. 9 flat sections arranged around the beam pipe, with overlap between neighbouring modules) and the outer layer consists of 15 modules at a radius of 11.0 cm. The solid angles covered by the inner and outer layers are $|cos\theta| < 0.85$ and $|cos\theta| < 0.65$ respectively. Each silicon module has readout strips on both surfaces; on one side the strips run parallel to the z direction (the 'z side') and on the other side they run perpendicular to the beam (the 'ϕ side'). These strips have dimensions such that there is an overall pitch of 25μm on both sides. However, every second strip on the z side collects electrons which produce no ionisation ('blocking strips'), thus effectively making the pitch on this side to

be 50μm. The readout pitch is 100μm so that there are approximately 72000 channels.

The point resolution obtained is 10μm in $r\phi$ and 13μm in z. The impact parameter resolution obtained from dimuon events ($Z^0 \rightarrow \mu^+\mu^-$), using all three tracking sub- components (i.e. TPC, ITC and VDET) has been measured to be 28μm in $r\phi$ and 34μm in z. The inclusion of VDET has improved the charged track momentum resolution to $\Delta p/p^2 = 0.0006 GeV^{-1}$.

2.10 The Luminosity Monitors.

The luminosity is measured from the rate of detected bhabha events with small scattering angles. This requires precise measurement of the polar scattering angles and good determination of the energy of each electron and positron pair. These criteria are achieved via a combination of a luminosity calorimeter (LCAL) and a small angle tracking device (SATR). A pair of these detector components are positioned either side of the interaction point, at $z \simeq \pm 2.7$m. Tracks within a polar range of 40 and 90 mrads are detected by the SATR, while the LCAL covers a range from 45 to 155 mrads; the overlap between the two being from 45 to 90 mrads.

2.10.1 The Small-Angle Tracking Device (SATR).

On either side of the interaction point the SATR consists of 9 layers of drift-tube chambers. Each layer is divided into 45^0 sectors, hence each layer has an overall octagonal shape. Consecutive layers are rotated by 15^0 in order to avoid overlapping dead regions. The individual drift cells are manufactured from brass and operated with a gas mixture of Argon ($\simeq$90%), carbon dioxide ($\simeq$10%) and a small admixture of isopropanol.

The position resolution of one drift tube is 320$\pm$20μm, which leads to an angular resolution of 0.08mrads for a whole chamber. the overall track reconstruction efficiency is 99%.

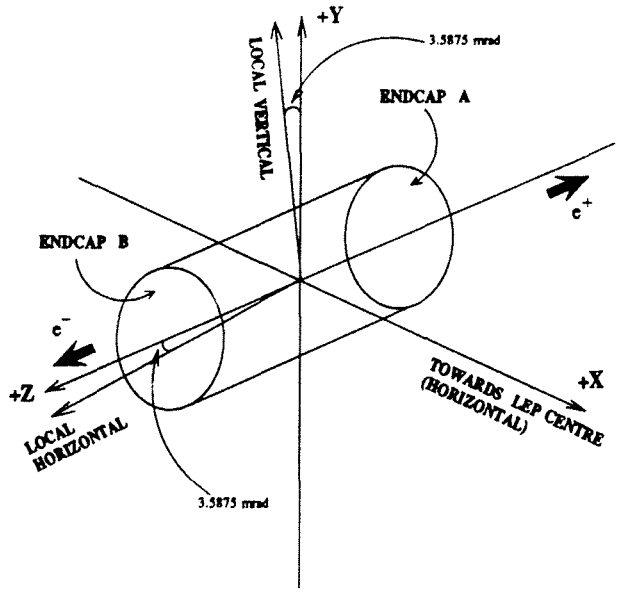

Figure 2.2: The ALEPH coordinate system.

2.10.2 The Luminosity Calorimeter (LCAL).

The essential mechanics of the LCAL are identical to those of the electromagnetic calorimeter, (see section 2.3), i.e. the use of lead/wire sampling layers; cathode pad segmentation with internal connection into three depth sections; the same gas mixture supplied by the ECAL gas system; and the same calibration methods. The obvious difference is in geometry. The LCAL consists of four semi-cylindrical modules, with an outer radius of 52cm, an inner radius of 10cm, and an overall length of 45cm. Two modules are positioned immediately behind each SATR (as viewed from the interaction point) on either side of the primary collision point.

2.11 The ALEPH Coordinate System

The Aleph coordinate system shown in figure 2.2 has its origin at the theoretical beam crossing point, defined to be the mid-point of the straight section between the two nearest LEP quadrupoles.

The positive z-axis is along the nominal e^- beam direction, which makes an angle of +3.5875 mrads (upwards) with the local horizontal. The positive x-axis points horizontally toweards a vertical line passing through the centre of the LEP

ring. (Note in this direction the LEP ring is inclined by 1.42%). The y-direction is orthogonal to the x and z- axes. The precise location of the ALEPH detector is given in terms of 32 survey marks on the walls of the experimental hall.

In this reference system, spherical polar coordinates (r, θ, ϕ) are defined by :

$$\begin{aligned} x &= r sin\theta cos\phi \\ y &= r sin\theta sin\phi \\ z &= r cos\theta \end{aligned} \tag{2.1}$$

and cylindrical coordinate (ρ, Φ, z) are given by :

$$\begin{aligned} x &= \rho cos\Phi \\ y &= \rho sin\Phi \\ z &= z \end{aligned} \tag{2.2}$$

2.12 The Trigger System.

A well designed trigger system must efficiently select the events under study without permitting the data collection systems to become swamped with background events. Hence the Aleph trigger system was designed to accept all e^+e^- events, with a flexibility such that varying background conditions (which depend on each LEP fill) can be facilitated. The main backgrounds which can cause false triggers are from beam-gas interactions and off-beam electrons/positrons colliding with the edges of the collimators or the vacuum chamber.

The basic Aleph philosophy in designing the trigger system was that the individual triggers must be sensitive to single particles or single jets , without looking for specific event types, whilst minimising dead-times in data acquisition. the Aleph trigger is divided into three levels of increasing refinement. Levels 1 and 2 being based on signals induced in various detector sub-components, while level-3 is an semi-off-line process involving overall event reconstruction. These are described in detail in following sections.

2.12.1 Detector Segmentation for Level-1 and Level-2 Triggers and Physics Trigger Design.

Level-1 and level-2 trigger decisions are based on information from the four main detector sub-components; the ITC, TPC, ECAL and HCAL, covering a large proportion of the total solid angle. from the calorimeters both the information from the wires and projective towers can be utilised.

The size of the Aleph detector and hence the number of electronic channels read out, does not permit a simple addition of all signals from all detector calorimeters to be used for efficient triggering purposes; particularly if sensitivity to small energy deposits dictated by physics requirements is to be maintained. This is simply due to the domination of electronic noise.

Thus, Aleph have opted for a segmented signal read-out structure whereby detector sub-components are grouped into 60 logical trigger segments. The segmentation closely resembles the module structure of the calorimeters; in particular the barrel region retains the 12 module division of 30^0 in azimuth. The end-caps of both calorimeters are divided into six segments of 60^0. The segmentation in polar angle, θ is more complicated, the segment size decreasing closer to the beam-pipe. In order to preserve the projective nature of the calorimeter, tower signals from different modules have to be mixed.

To monitor the luminosity, the LCAL (see section 2.10.2) tower signals are used to trigger on forward Bhabha events. Each half of the LCAL is divided into 12 segments in azimuth, hence the LCAL tower signals are divided into 24 trigger segments. However, in order to establish a trigger signal, the analogue signals of two adjacent segments are summed to form a supersegment.

The multitude of analogue signals arriving from the calorimeters are summed by the trigger electronics to obtain the segment signals. Each segment signal is sent to four discriminators which have remotely adjustable threshold levels, so as to yield four YES/NO signals. The resulting digital signals are ordered into 60 bit arrays and are available for combination into 'physics' triggers.

Varying combinations of detector sub-components allows differing degrees of 'coarseness' for triggering purposes, i.e. individual segment signals or grouped seg-

ment signals can be used. the source signals from the different detector components available for the formation of 'physics' triggers are as follows :

- HCAL towers : 60 segments;
- HCAL wires : 24 direct module signals; or mapped onto 60 segments;
- ECAL towers : 60 segments;
- ECAL wires : 36 direct module signals; or mapped onto 60 segments;
- ITC pattern : track candidates in 60 ϕ segments;
- TPC pattern : track candidates in 60 $\theta - \phi$ segments;
- LCAL towers : 2x12 overlapping segments.

By establishing the trigger condition in each segment and then logically 'OR'ing the segments, the requirements of a particular physics trigger can be imposed. Up to 32 such combinations and hence physics triggers can be defined [10]. By logically 'OR'ing all physics triggers a global YES/NO decision for the whole 'event' at the relevant trigger level can be made.

2.12.2 The Level-1 Trigger.

The first trigger decision is made within 5μs of the beam crossing. This is a fast decision (especially when compared to the 22.5μs between beam crossings), made using information from the ITC,ECAL and HCAL, and commences the event digitisation. The rate of triggering at this level needs to be maintained at a level of a few hundred hertz so as to keep the space-charge effects in the TPC small (see section on 2.4). A typical level-1 trigger is :

- Single Charged Electromagnetic Energy Trigger - a coincidence between the ITC and ECAL, requiring a track in the ITC (at least 5 out of 8 planes fired) and an energy of at least 1.3GeV in an ECAL module in the same azimuthal region.

2.12.3 The Level-2 Trigger.

Here, the tracking information from the ITC in the level-1 decision is refined using the TPC. A decision at this level is made within approximately 50μs (dominated by the drift time within the TPC), and the trigger rate is kept below 10Hz.

This trigger checks for charged tracks in the r-z plane, originating from the primary vertex using hard-wired processors. Signals for this trigger are provided by the 1152 'trigger' pads situated between the rows of standard pads in the TPC end-caps (see section 2.4) and analysed by the standard TPC devices. If tracks are identified within the TPC, then the ITC signal configuration is replaced by the TPC signal configuration in the combination of physics triggers defined at level-1. If the second level trigger cannot confirm the level-1 decision the readout process must be stopped and the experiment must be ready to accept the third bunch crossing after the initial trigger i.e. within 67 .5μs of the first trigger decision. The TPC drift-time and ECAL clearing time amounts to 61μs, therefore, within 6μs of the end of the TPC drift time, all parts of the detector must be reset. To achieve this the data are analysed as they arrive during the drift-time period. Therefore, by using 24 processors to search independently for tracks in six-ϕ sectors and in two radial zones of each end-plate, processing of most events is complete before the end of drift.

2.12.4 The Level-3 Trigger.

Once an event has satisfied both the level-1 and level-2 criteria, the event digitisations are passed to the level-3 trigger. The main purpose at this level is to reduce the trigger rate to a manageable 1-2 Hz, suitable for recording on the various storage media. This is achieved by means of an analysis process running within the data acquisition (DAQ) (see section 2.14) prior to recording the events. In order to cope with the event output rate from the level-2 trigger several copies of the analysis process run concurrently on a set set of independent computers (together these computers comprise the 'ALEPH event processor'). The analysis program design is such that there is emphasis on high pattern recognition efficiency whilst keeping the computer CPU time as low as possible, rather than on the precision

of event reconstruction. In this way the need for high-level calibration of analogue signals is avoided. Also, reconstruction of events is only performed in regions of the detector where the first and second level triggers have shown activity, and it only continues until sufficient information on the good quality of a trigger is obtained.

2.13 Trigger Efficiencies.

A possible draw-back of the segmented trigger method used at levels 1 and 2, would be that inefficiencies could arise when jets or particles deposit their energy in two adjacent segments, which remains below threshold in both parts. This was studied using events simulations, grouping segments to form overlapping super-segments and comparing the resulting trigger efficiency. The study showed that supersegments were not necessary.

Since events are generally triggered by more than one of the 'physics' triggers the overall efficiency was found to be 100% for hadronic Z^0 decays, $\simeq$100% for leptonic Z^0 decays and 99.7$\pm$0.2% for Bhabha events [10].

2.14 Data Acquisition (DAQ) and Event Reconstruction.

The data acquisition is responsible for ensuring that all relevant information of an event is correctly recorded onto disk or cartridge, suitable for off-line physics analysis. The ALEPH system of processors used to access the information from the different sub-detectors has a flexible, tree-like structure suitable for autonomous operation of individual detector components (see figure 2.3) (this is known as 'partitioning').

In a cycle of triggering, data recording and re-initialisation of sub-detector components between beam crossings, the data acquisition starts at the individual sub-detectors. Information about the LEP timing of beam crossings is fed to a Main Trigger Supervisor (MTS), which synchronises the readout electronics of each sub -detector. These in return inform the MTS when a suitable trigger has

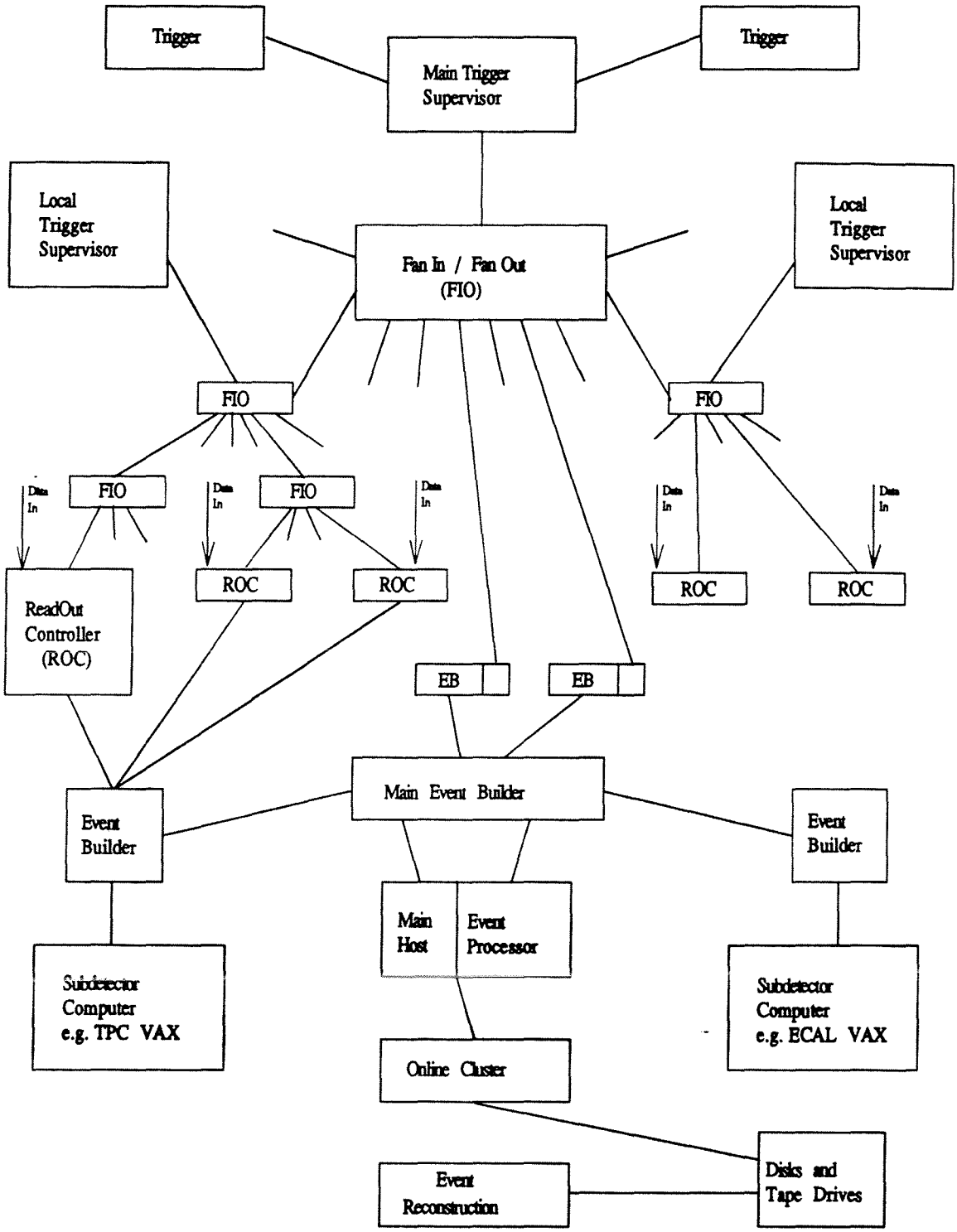

Figure 2.3: 'Partitioning' of the ALEPH Data Acquisition system. The diagram also shows the flow of data from triggering to event reconstruction.

occurred. The MTS then conveys the availability of data via Fan In/Out (FIO) units to the ReadOut Controller (ROC) of each sub-detector, synchronising the ROC's and measuring the amount of dead-time in the experiment. Apart from 'fanning-out' the trigger and timing information to the ROC's, the FIO's also confirm the BUSY state of a ROC (i.e. that it is collecting information about the event) and expects an acknowledgement signal (ACK) in return. On receiving triggering and timing signals, the ROC's initialise the front-end electronics, read-out the information and format the data into a manageable system of banks (BOS banks [31]. A further duty of the ROC's is to perform the initial calibrations of the various sub-detectors.

The partitioned structure of the DAQ system is particularly useful during calibration runs and for debugging both sub-detector hardware and software faults. Any configuration of sub-detector components is achieved by programming the FIO units so that trigger signals are only sent to those ROC's which are within the partition at the time of triggering.

Processing of information by the ROC's is followed by Event Builders (EB 's) using the data to recreate the event configuration, called a 'subevent', for that particular sub-detector. Any further formatting necessary is also done at this stage. Although these subevents still require refinement before eventual storage on various media, they are suitable for checking the quality of information recorded by each sub- detector. Thus they provide on-line 'spy-events'. A Main Event Builder (MEB) collects the subevents from each sub-detector EB to recreate the overall event. At this point in the data acquisition the level-3 trigger is implemented (see section 2.12.4). Transferring the surviving data to the Main Host computer allows storage on various media and also provides data for on-line analysis and event displays. The Main Host also provides the services which are common to all the sub-detector computers . If a particular sub-detector is out of the partition, then the sub- detector computer acts as the 'main machine' for that sub-detector.

The time period of data taking is given naturally by different LEP fills . However, shorter time periods are needed for the detector, taking into account problems or varying conditions. Hence, data is recorded in 'runs ', i.e. continuous periods of data taking. At the end of a run, the raw data files written to disk by the DAQ are

available to the ALEPH Event Reconstruction Facility (FALCON) for 'quasi-on-line' event reconstruction. The Aleph Event Reconstruction program, JULIA [32] , creates the kinematic four-vectors for the various particles in each event, from the raw data and calibration constants accessed from a database. Since each event in a run is independent from the next, subsets of events are reconstructed in each of 12 processors running in parallel. The results are written to separate disk files where they are recombined into a single file with the original order of events. These files are called Production Output Tapes (POT's), from which further information compression (i.e. selecting only the essential information about particular events) can be performed to produce Data Summary Tapes (DST's).

An event is unambiguously identified by its event and run numbers. Thus by creating Event Directories (EDIR's) which contain the record number of each event in a run, sub-samples of the original event set can be selected, without the need to access all the events. This has the great advantage of reducing CPU time spent on running physics analysis routines, and also facilitates selection of individual data sets specific to a particular analysis.

2.15 The Aleph Physics Analysis Package (ALPHA).

Measured kinematic variables such as energies and track momenta are required by the majority of physics analyses. Although these quantities can be accessed with a knowledge of the structure of BOS banks storing this information, repeated acces can be time consuming (especially in terms of CPU time). Thus the Aleph collaboration has devised a package within which FORTRAN analysis code can be easily written. This is the Aleph Physics Analysis package (ALPHA) [33]. Within the framework of ALPHA all kinematic variables can be easily accessed without specific knowledge about the data bank structure.

ALPHA is capable of analysing both Monte-Carlo simulated and real data. It also allows analysis of simulated data before reconstruction by JULIA , i.e. allows easy access to the Monte-Carlo generated data.

2.16 Detector and Data Simulation.

Monte-Carlo techniques prove to be powerful tools in analysing data when analytical methods become too complex to manage. This is the case when studying the production and decay processes of the tau lepton, as it may decay into several final state particles. If Monte-Carlo simulation is to be used for measuring any physical quantity, then accurate representation of the real data is essential. It is not only necessary to have correct simulation of the decay mode required for further analysis, all background modes also need to be understood.

In some circumstances real data can be used to check the quality of the Monte-Carlo and also to determine selection efficiences and the level of backgrounds. For example, in attempting to isolate a clean sample of $\tau^{\pm} \rightarrow \pi^{\pm}\nu_{\tau}$ events the penetration of a charged track into the latter few layers of the HCAL can be used (see section 4.2.2). But, in this situation a possible source of misidentification is with tracks left by muons. A check on the selection efficiency of a pion identification algorithm, independent of the Monte- Carlo, can be performed by using charged tracks from rho events, where the sample of rho's is tagged using the π^0. Requiring a fully reconstructed π^0, i.e. where both photons are resolved, essentially demands the charged track to be a pion. Here there is added advantage since the tagging particle is identified using the ECAL, which is totally independent of the sub-detector used for the charged pion identification; namely the HCAL. Conversely, a rho sample can be used to determine the amount of pion background accepted by a muon identification algorithm.

Use of real data as described above allows backgrounds, acceptances etc. to be determined independent of parameters such as branching ratios which need to be inserted into any Monte-Carlo method and which may not be accurately known.

Of course crucial to the discussion above is the availability of an independent real data sample. For the rho data a clean sample of π^0's and charged pions can only be obtained from the rho's themselves. For the a_1 sample the charged track multiplicity means that it is difficult to isolate a tau decay mode with a sufficiently large branching ratio for any independent checks on the Monte-Carlo. In principle the mode $\tau^{\pm} \rightarrow 3\pi^{\pm}\pi^0\nu_{\tau}$ could be isolated by tagging the π^0, but this proves to

be difficult within the highly collimated jet environment, (as indeed can be seen from table 2 which indicates that the largest background to the a_1 sample is from $3\pi^{\pm}\pi^0$ decays of the tau).

Consequently the present analysis was entirely dependent on the Monte- Carlo sample, and discrepancies with the real data were quantified into a systematic uncertainty.

The response of the Aleph detector is modelled by a simulation program based on the GEANT [34] algorithm for tracking particles through various detector media. The version specific to Aleph is called GALEPH [35] which includes detector resolution effects. (This eliminates any need to fold any resolution functions into theoretical descriptions of physics processes studied).

The various physics processes expected at LEP are simulated by various event generators available, e.g. [36] and KORALZ [37] Monte-Carlo for $e^+e^- \rightarrow \mu^+\mu^-$ and $e^+e^- \rightarrow \tau^-\tau^-$ events. (These generators are all based on the modulation of a generated random number, by the current theoretical understanding of the process.) The particle four-vectors emerging from such a generation process can be passed through the detector simulation, GALEPH, to produce events expected in the real data . Storing these Monte-Carlo events in the same BOS bank structure as the real data then allows them to be treated as if they were actually observed. Reconstruction by JULIA and treatment by any analysis program then allows comparison between what is expected/understood and what is eventually observed.

2.16.1 The Tau Lepton Simulator, KORALZ.

The simulated $\tau^+\tau^-$ events analysed in this thesis were produced by the KORALZ program of generators, version KORL03 and KORL04 [38]. The KORALZ program simulates fermion pair production, where the fermion is either a lepton or a quark (except the top quark). The simulation takes into account the following important effects :

- Multiple QED hard initial state bremsstrahlung and single photon bremsstrahlung from the final state.
- $O(\alpha)$ radiative corrections from the standard electroweak model.

- Inclusion of the most frequent tau decays, including multipion events with up to 6 π^0's.
- Spin polarisation effects in the tau decays (except for the multipion modes).
- longitudinal spin polarisation of the beams.
- Single bremsstrahlung in the $e^{\pm}$, $\mu^{\pm}$, $\pi^{\pm}$, $\rho^{\pm}$, $K_1^{\pm}$ and $K^{*\pm}$ decays of the tau.

Chapter 3

The Polarisation of the Tau Lepton.

By convention the average longitudinal polarisation asymmetry of the tau , P_τ, is taken to be that of the τ^- which is defined by:

$$P_\tau \equiv P_{\tau^-} = \frac{\sigma_R - \sigma_L}{\sigma_R + \sigma_L} \tag{3.1}$$

where $\sigma_{R/L}$ is the cross-section for the production of a right/left handed τ^- respectively. Assuming CP invariance [39] the polarisation asymmetry for a positive tau, τ^+, is simply related to equation 3.1 by $P_{\tau^+} = -P_{\tau^-}$, and consequently both τ^+ and τ^- events can be used to determine P_τ.

If the decay of the tau is assumed to proceed via a V-A current structure (where V $\equiv$ vector coupling and A $\equiv$ axial-vector coupling), then the general decay distribution of the tau has the following form : [39, 40, 42]

$$W_\tau = g(\underline{a}) + P_\tau f(\underline{a}) \tag{3.2}$$

where $\underline{a}$ is the set of observables used in the measurement. The P_τ dependence of equation 3.2 is a direct consequence of parity violation in the tau decay.

The decay spectra described by equation 3.2 have their simplest forms in the rest frame of the tau. However, since every tau decay results in the production of at least one (anti)neutrino which goes undetected by the ALEPH detector, it is not possible to reconstruct the tau rest frame. All decay distributions must therefore be boosted into the laboratory frame, thus relating the decay spectra to the actual observables measured.

It is widely known [19, 41] that due to its mass, the tau has many semi-hadronic decay modes as well as decaying purely leptonically. For the decays $\tau \rightarrow \nu_\tau l \overline{\nu_l}$, with $l = e, \mu$, equation 3.2 has the form :

$$W_l = \frac{1}{3}[(5 - 9x^2 + 4x^3) + P_\tau(1 - 9x^2 + 8x^3)] \tag{3.3}$$

where $x = E_{lepton}/E_{beam}$, E_{lepton} is the energy of the decay lepton in the laboratory frame and E_{beam} is the beam energy used to approximate the energy of the tau. In determining expression 3.3 the Standard Model values for the Michel parameters ($\rho = \delta = 3/4$ and $\xi = 1$) [21, 42] are assumed and also $m_{lepton} << m_\tau$ and $m_\tau << m_{Z^0}$, where m_{lepton}, m_τ and m_{Z^0} are the masses of the decay electron/muon, the tau and the Z^0 boson respectively.

For semi-hadronic tau decays, the quantum numbers of the final state hadron have a significant effect on the decay distributions. Within the Standard Model these quantum numbers are fixed such that assuming V and A couplings, the spin of the hadronic system is either J=0 or J=1. [39]. The simplest of these decays is $\tau \rightarrow \nu_\tau \pi$, the pion having J=0. This is a two body decay with only one undetected (anti)neutrino, thus the pion spectrum is exactly calculable and has the form :

$$W_\pi = \frac{dN_\tau}{dcos\theta} = \frac{1}{2}[1 + P_\tau cos\theta] \tag{3.4}$$

Here, θ is the decay angle of the hadron in the tau rest frame relative to the tau line of flight in the laboratory. (This direction is approximated by the direction of the hadron in the laboratory frame).

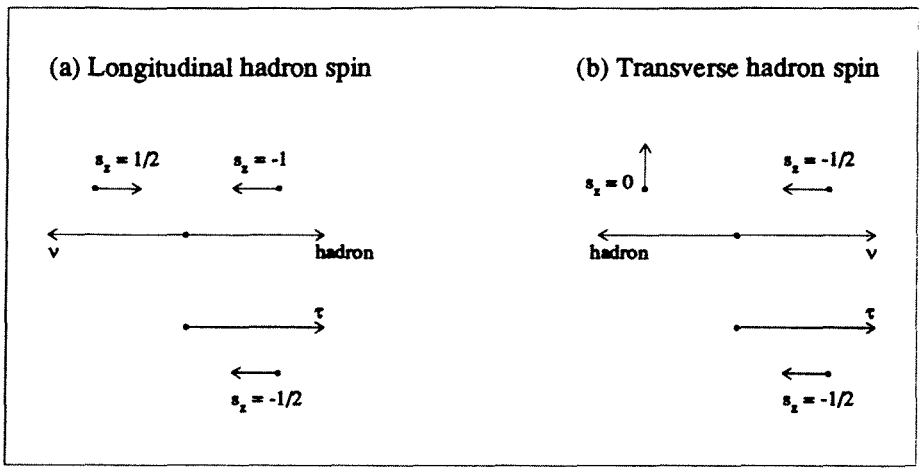

Figure 3.1: Allowed spin configurations for a spin 1 daughter particle from a tau decay

For any semi-hadronic two-body tau decay, $cos\theta$ is related to the observable $x = E_{hadron}/E_{beam}$ by :

$$cos\theta \simeq \frac{2x - 1 - (m_h/m_\tau)^2}{1 - (m_h/m_\tau)^2} \tag{3.5}$$

where m_h is the mass of the hadron and equation 3.5 is derived in the colinear limit i.e. $E_\tau/m_\tau >> 1$.

For spin 1 hadrons produced in decays such as :

$$\tau \rightarrow \nu_\tau \rho \qquad J^P = 1^- \tag{3.6}$$

$$\tau \rightarrow \nu_\tau a_1 \qquad J^P = 1^+ \tag{3.7}$$

complications arise from the orientation of the hadronic spin; the hadron can either be transversely or longitudinally polarised (see figure 3.1).

Figure 3.1 shows that transversely polarised hadrons in the tau rest frame are preferentially produced in the direction of the tau spin and longitudinally polarised hadrons are preferentially produced in the direction opposite to the tau spin. Thus, one can expect the decay spectrum for a transversely polarised hadron to be similar

to that for $\tau \rightarrow \nu_\tau \pi$. The expression for longitudinally polarised hadrons is of a similar form, except P_τ appears with the opposite sign [40] Thus, if the spin state of the hadron is not distinguished, the longitudinal and transverse hadron distributions must be averaged resulting in :

$$dN_\tau = \frac{1}{2}(1 + \alpha P_\tau cos\theta) \tag{3.8}$$

where α is given by :

$$\alpha = \frac{m_\tau^2 - 2m_h^2}{m_\tau^2 + 2m_h^2} \tag{3.9}$$

So, for $\tau \rightarrow \nu_\tau \rho$ decays $\alpha_\rho \simeq 0.46$ and for $\tau \rightarrow \nu_\tau a_1$ decays $\alpha_{a_1} \simeq 0.12$. Hence, there is a significant loss in sensitivity of the decay spectra to the polarisation of the tau.

In order to regain the analysing power, the two polarisation states of the hadron must be separated. This can be achieved by considering the configurations of the final state pions from the hadronic decay, i.e.

$$\rho^\pm \rightarrow \pi^\pm \pi^0 \tag{3.10}$$

$$a_1^\pm \rightarrow \pi^\pm \pi^\pm \pi^\mp \tag{3.11}$$

$$a_1^\pm \rightarrow \pi^\pm \pi^0 \pi^0 \tag{3.12}$$

Figure 3.2 shows the decay angles ψ_ρ, ψ_{a_1} used to parameterise the pion configurations. For rho decays, ψ_ρ, is the angle made by the charged pion, in the rest frame of the rho, to the rho line of flight in the laboratory [43, 45]. It is given by :

$$cos\psi_\rho = \frac{m_\rho}{\sqrt{m_\rho^2 - 4m_\pi^2}} \frac{(E_{\pi^\pm} - E_{\pi^0})}{|\vec{p}_{\pi^\pm} + \vec{p}_{\pi^0}|} \tag{3.13}$$

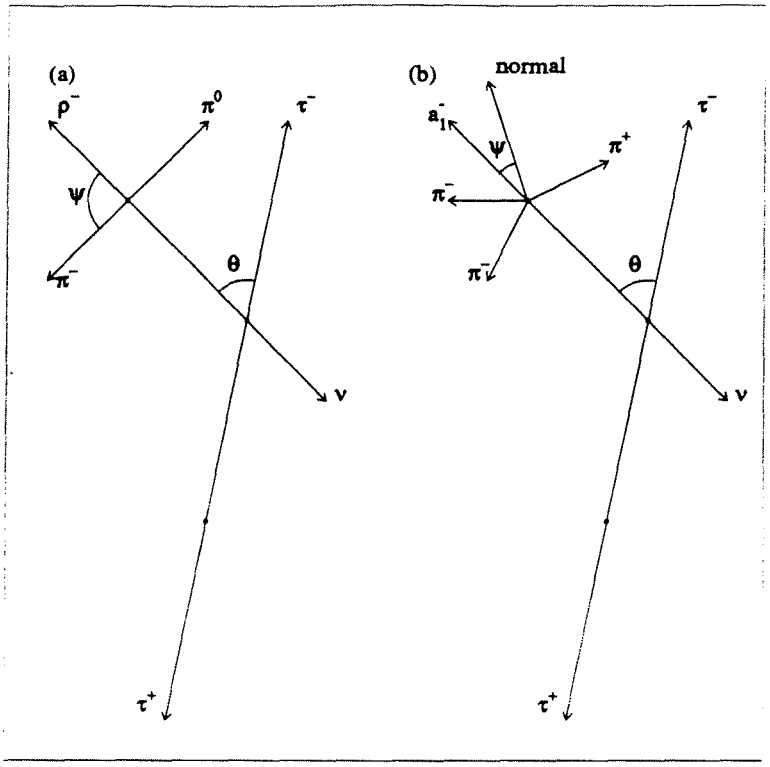

Figure 3.2: Decay angles for 2 and 3 pion final states. (a)Decay via the ρ. ψ_ρ is the angle of the 2π system in the rest frame of the ρ relative to the ρ line of flight. (b)Decay via the a_1. ψ_{a_1} is the angle between the normal to the decay plane of the 3π system in the rest frame of the a_1 and the a_1 line of flight.

For a_1 decays, the normal to the 3 pion decay plane (in the a_1 rest frame) is used such that ψ_{a_1} is the angle made by this normal to the a_1 line of flight in the laboratory frame [45]. In terms of the measured pion variables, this angle is given by:

$$cos\psi_{a_1} = \frac{8m_{a_1}^2 \vec{p}_1.(\vec{p}_2 \wedge \vec{p}_3)}{|\vec{p}_1 + \vec{p}_2 + \vec{p}_3|\sqrt{-\lambda\left(\lambda(m_{a_1}^2, m_{12}^2, m_\pi^2), \lambda(m_{a_1}^2, m_{13}^2, m_\pi^2), \lambda(m_{a_1}^2, m_{23}^2, m_\pi^2)\right)}} \tag{3.14}$$

where $\vec{p}_i$ is the measured momentum of pion i, m_{ij} is the invariant mass of pions i and j, m_π is the mass of a pion, m_{a_1} is the reconstructed mass of the a_1 and $\lambda(x,y,z) = x^2 + y^2 + z^2 - 2xy - 2yz - 2zx$.

The amplitudes for longitudinal and transverse hadron polarisation can be expressed in terms of these angles ψ_{ρ/a_1}, and included in the decay distribution given

	$h_0(cos\psi)$	$h_1(cos\psi)$
ρ decay	$2cos^2\psi_\rho$	$sin^2\psi_\rho$
a_1 decay	$sin^2\psi_{a_1}$	$\frac{1+cos^2\psi_{a_1}}{2}$

Table 3.1: Decay distributions for the pion systems from ρ and a_1 decays.

by equation 3.2, describing the overall tau decay.

Equation 3.2 expressed explicitly in the two variables $cos\theta$ and $cos\psi$, for any spin 1 hadron then becomes [42, 45]:

$$W(cos\theta, cos\psi) = \frac{3}{8(m_\tau^2 + 2m_h^2)} \left\{(1 + P_\tau)W^+(cos\theta, cos\psi) + (1 - P_\tau)W^-(cos\theta, cos\psi)\right\} \tag{3.15}$$

where

$$W^\pm(cos\theta, cos\psi) = \omega_1^\pm(cos\theta)h_1(cos\psi) + \omega_0^\pm(cos\theta)h_0(cos\psi) \tag{3.16}$$

$$\omega_0^+ = (m_\tau cos\eta cos\frac{\theta}{2} + m_h sin\eta sin\frac{\theta}{2})^2 \tag{3.17}$$

$$\omega_0^- = (m_\tau cos\eta sin\frac{\theta}{2} - m_h sin\eta cos\frac{\theta}{2})^2 \tag{3.18}$$

$$\omega_1^+ = (m_\tau sin\eta cos\frac{\theta}{2} - m_h cos\eta sin\frac{\theta}{2})^2 + m_h^2 sin^2\frac{\theta}{2} \tag{3.19}$$

$$\omega_1^- = (m_\tau sin\eta sin\frac{\theta}{2} + m_h cos\eta cos\frac{\theta}{2})^2 + m_h^2 cos^2\frac{\theta}{2} \tag{3.20}$$

The functions $h_0(cos\psi)$ and $h_1(cos\psi)$ are defined separately for ρ and a_1 decays [42, 45] as listed in table 3.1

As explained previously, the rest frame of the tau cannot be reconstructed, thus all distributions must be boosted into the laboratory frame. This means that the

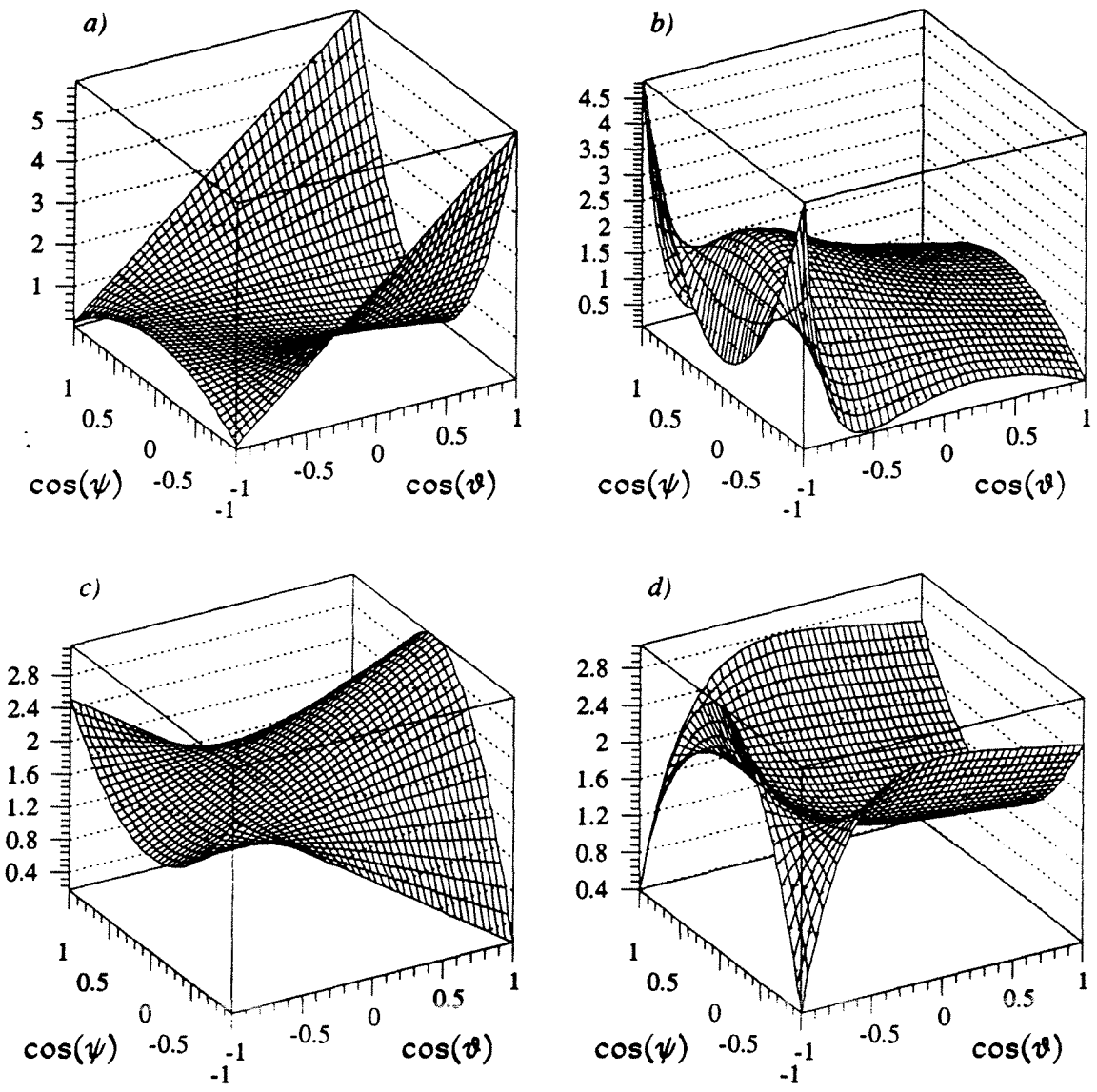

Figure 3.3: Theoretical angular distributions for $\tau^{\pm} \rightarrow \nu_{\tau}\rho^{\pm} \rightarrow \pi^{\pm}\pi^{0}$ decay, figures (a) and (b), and $\tau^{\pm} \rightarrow \nu_{\tau}a_1^{\pm} \rightarrow \pi^{\pm}\pi^{\pm}\pi^{\mp}$,decay figures (c) and (d). The distributions are also shown for the two tau helicity states; figures (a) and (c) are for P_{τ}=+1 and figures (b) and (d) are for P_{τ}=-1.

tau spin is no longer in a helicity eigenstate but has been rotated by some angle, η (Wigner rotation). In the limit $E_\tau >> m_\tau$, this angle is given by :

$$cos\eta \simeq \frac{m_\tau^2 - m_h^2 + (m_\tau^2 + m_h^2)cos\theta}{m_\tau^2 + m_h^2 + (m_\tau^2 - m_h^2)cos\theta} \tag{3.21}$$

Hence the presence of $cos\eta$ and $sin\eta$ terms in the general decay distribution given by equation 3.15.

The functions $W^{\pm}(cos\theta, cos\psi)$ are shown in figures 3.3 for $P_\tau = \pm 1$.

Using these two-dimensional distributions the sensitivity of the spin 1 hadronic decay modes to the tau polarisation becomes comparable to that for $\tau \rightarrow \nu_\tau \pi$ case [42, 45].

This theoretical understanding is included into a Monte-Carlo simulation which is then used to extract the average longitudinal polarisation of the tau using its decay into two and three pion final states. The selection of these events is described in chapter 4. The method used and the results of its application are detailed in chapter 5. Chapter 6 gives the results of the study of systematic uncertainties contributing and chapter 8 draws final conclusions and Standard Model implications of the polarisation measurement.

Chapter 4

The Data Samples.

4.1 Event Preselection.

Initially event selection involved classification of Z^0 decays into either leptonic ($Z^0 \rightarrow l^+l^-$, where l=e, μ, or τ) or hadronic ($Z^0 \rightarrow q\bar{q}$) events. The procedure made use of the tracking information from the TPC; a cut being made on the charged particle multiplicity. Attempts could have been made to identify individual tau events from the outset, but this would have introduced an inherent systematic uncertainty in the event sample subsequently analysed for specific tau decay modes. For this reason the charged multiplicity method was preferred.

In order to have accurate reconstruction of tracks genuinely from Z^0 decays minimum requirements were imposed to define a 'good' track. Tracks were required to have a momentum greater than 0.1 GeV/c derived from at least four sets of spatial coordinates measured by the TPC, which could be extrapolated to originate from within 7cm of the beam crossing point as measured along the beam direction (Z_0 distance) and within 1.5cm measured in a transverse direction from the same origin (D_0 distance).

These constraints essentially on the primary vertex, efficiently eliminate most beam-gas interactions, cosmic rays and ambiguities resulting from poorly measured coordinates. The majority of hadronic Z_0 decays were removed by restricting the total number of tracks so defined in an event to be greater than one but less than seven. The remaining low multiplicity of tracks allowed easy identification of the

jets produced for which a thrust axis was determined and the event divided into two hemispheres by a plane perpendicular to this axis. To ensure events were in regions of the detector where the kinematics could be well measured and to minimise loss of particles down the beam pipe the thrust axis polar orientation was required to be such that $|cos\theta_{thrust}| \leq 0.95$. Also, the polar angle subtended by each track at the point of closest approach to the beam crossing, with respect to the beam direction was required to be within the same fiducial region. The events which remained consisted of leptonic Z^0 decays, low multiplicity hadronic Z^0 decays, a small contribution from cosmic rays and two photon events. These last set of events are characterised by a low visible invariant mass (since most particles are lost down the beam pipe) and an unrestricted acollinearity angle. Insisting on at least one track in each hemisphere, i.e. a minimum 1 - 1 topology, along with a restricted polar range allowed better discrimination between Z_0 decays and two photon events. For events with a 1 - 1 topology the D_0 distance was required to be less than one centimetre in order to eliminate cosmic rays further. To extend the discrimination against hadronic decays of the Z^0 each constituent track within a jet had to make an angle of less than 18.2^0 to the jet axis.

The acollinearity angle is the difference between 180^0 and the opening angle between the vector sums of the track momenta in each hemisphere. Consequently, imposing a cut on this angle so that $|cos\theta_{acoll}| < 0.9$ and requiring at least one track to have a momentum greater than 3GeV/c greatly suppressed the two photon background.

The eventual sample of predominantly leptonic events was then analysed for specific tau decays.

4.2 Charged Pion Identification.

At this stage of the data selection individual charged tracks were identified to separate out the pion candidates. Almost all the confusion arose from an admixture of electrons/positrons and muons in the general lepton sample, (there was a component contribution from other hadrons such as K^*'s, but these cannot be individually identified by ALEPH.) . Thus, estimators were developed to unravel

the different leptonic and hadronic decays.

4.2.1 $e^{\pm}$ Identification

The R2 Estimator

For electron/positron - pion separation the high granularity of the ECAL was exploited. The developement of an electromagnetic shower in the ECAL is characteristically different for electrons/positrons and pions. The electromagnetic interaction of the leptons ($e^{\pm}$) means that most of their energy is deposited within the first two stacks (i.e. the first 13 radiation lengths) of the ECAL (see section 2.3. [10]) whereas the hadronic interaction of pions means that if pions interact within the ECAL at all their longitudinal energy deposition profile begins to peak towards exiting stack 3, the majority of their energy being deposited in the hadron calorimeter. This also means that the electromagnetic cascade induced by an electron/positron will have a greater transverse developement early in the ECAL than that induced by a hadron. Thus the estimator developed within the ALEPH collaboration essentially compares the energy deposited in the four towers of the ECAL closest to the extrapolated track to the measured momentum.

By extrapolating a track to each ECAL stack, the energy in the four towers closest to the extrapolation (E_4), can be found. For electrons of a given energy and momentum p>2 GeV/c, the ratio of this energy to the track momentum (i.e. X = E_4/p) has a gaussian distribution with a mean <X> just less than unity, independent of incident angle and momentum [46]. Thus, defining the variable R2, as the difference between the measured ratio X, and the mean value <X>, normalised to the standard deviation of the gaussian (measured using test beam data), a normal distribution centred on zero with a unit variance results for $e^{\pm}$.

So, for particles such as hadrons, which deposit little of their energy in the ECAL, R2 will be negative and several standard deviations from zero. Figure 4.1(a) shows the R2 estimator for one prong events passing the preselection cuts. A peak centred around zero is prominent corresponding to bhabha and $\tau \rightarrow e\nu\nu$ events. The distribution rises with decreasing values of R2, corresponding to minimum ionising particles.

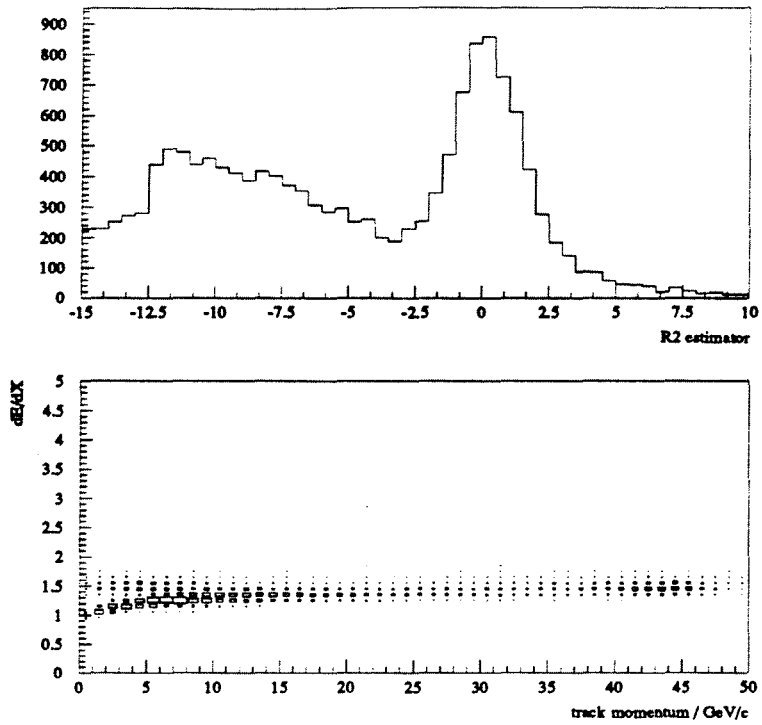

Figure 4.1: (a)The R2 estimator used for hadron - electron/positron separation. The estimator is shown for events passing the preselection cuts. (b) The dE/dX information as a function of track momentum for the same events.

Use of dE/dX for Particle Identification.

Ionisation density information (i.e. dE/dX) can be used for particle identification (see for example [1]), as different charged particles show characteristically different dE/dX curves when plotted as a function of charged particle momentum. The dE/dX information from the ALEPH TPC, for one pronged events passing the preselection described in section 4.1 is shown in figure 4.1(b). Below a momentum of approximately 5 GeV/c two bands can clearly be seen; the upper band corresponding to electrons/positrons and the lower one to pions. Above this momentum the two bands become increasingly indistinguishable. It is also interesting to note that the density of events in the band shows a marked increase at around 45 GeV/c , these are bhabha events passing the preselection cuts.

Thus, it is apparent from figure 4.1(b) that use of dE/dX information is restricted to low momentum tracks. For such cases, this information (when available!) was used to supplement the R2 estimator described above . Separation of

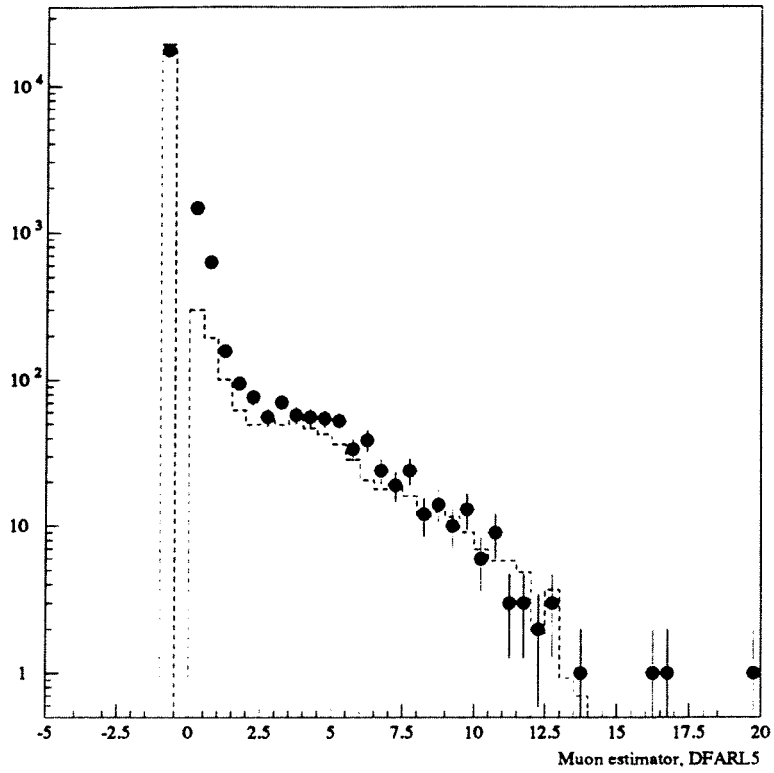

Figure 4.2: The DFARL5 estimator used for muon identification. The dashed histogram is the Monte-Carlo normalised to the real data (circles). Events at DFARL5 = -1.0 are from tracks producing no hits in the last few planes of the HCAL, corresponding to pions. The peak at DFARL5 = 0.0 is due to muons and the tail at larger values correspond to pions with a shower extending through to the last few HCAL layers.

particles was done by defining a probability in terms of the number of standard deviations the measured dE/dX was from that expected for a hypothesis of electron/positron or pion, a track being classified according to the higher probability.

4.2.2 $\mu^{\pm}$ Identification

A further source of complication, particularly for one prong events was that due to muons, from $Z^0 \rightarrow \mu^+\mu^-$ decays and from $\tau^{\pm} \rightarrow \mu^{\pm}\nu_{\mu}\nu_{\tau}$. These could be confused as rho candidates if photons were radiated at some stage of the decay process (initial state or final state radiation.), or a 3 pronged event if a photon converts. The fact that muons are highly penetrating was used to identify them. As is the case with hadrons, muons pass through the ECAL with hardly any inter-

action. Consequently it proved to be relatively easy to distinguish between muons and electrons/positrons, it was with the hadrons that the main confusion arose. Whereas muons also pass through the HCAL with little interaction, producing a well defined series of hits through the layers, hadrons produce a shower which propagates longitudinally through the HCAL layers; increasing in width transversely. Although these showers generally terminate before reaching the last few layers of the HCAL, sometimes the hadron showers late producing hits in these planes. Therefore, to accommodate all possibilities an estimator was developed based on the hits recorded in only the last 5 planes of the HCAL. If there were no hits in these planes then it was reasonably safe to assume that the track was not a muon, and the estimator was assigned a value of -1.0, (complications arise if the track passed through 'cracks' in the calorimeters, thereby leaving few HCAL hits even though it may have been a hadron.) If there were hits in these last few planes then the estimator was given the value obtained from calculating the mean distance of each HCAL cluster within a 'road' of width 40cm either side of the charged track extrapolated from the TPC through the HCAL. This mean was normalised to the approximate range expected from multiple scattering, to produce a dimensionless quantity, DFARL5. For muons this estimator will have a low value, peaking at around zero. For pions the propagation of the shower will result in larger positive values of DFARL5. Figure 4.2 shows a peak at DFARL5 = 0.0 tailing off at higher values in the manner discussed. The dashed histogram in this figure is the Monte-Carlo normalised to the real data (the circles). The disagreement between data and Monte-Carlo at around DFARL5 = 0.0 (region populated by muons) was not a problem since tracks were only selected as pion candidates if their DFARL5 value was either negative, i.e. equal to -1.0, or larger than a cut placed at around the point-of-inflexion, i.e. DFARL5$\sim$3.0 .

4.3 Neutral Pion (π^0) Reconstruction.

The tau lepton has many decay modes which involve the production of one or more neutral pion, (π^0) (branching fraction >42.9$\pm$0.6% [8]). If no attempt was made to distinguish the number present there would be a significant contribution to the

data sample from the modes not being isolated for analysis. Events with just two pions from tau decay have by conservation of charge one neutral pion. Therefore, to avoid backgrounds from dominating further analysis, it was essential to identify π^0's.

Neutral pions posed particular problems in reconstruction as the only information recorded about them was the energy deposited by the daughter photons in the ECAL. Accurate use of this information was governed by the resolution available. The centre-of-mass energies used at LEP were such that the resulting jets from tau decays were highly collimated. This complicated identification of individual photons due to overlapping of showers from neutral and charged particles. Problems from asymmetric π^0 decays, resulting in the loss of the low energy photon and a degradation in the reconstructed kinematics, also had to be addressed.

4.3.1 Photon Reconstruction.

As a starting point, energy deposits in the ECAL identified by the ALEPH reconstruction program, JULIA [32] were categorised according to the angle between the barycentre of the energy deposit and the direction of the vector sum of the charged tracks within a hemisphere. Clusters with barycentre angles less than 0.02 radians to the resultant track direction were classified as 'charged' and those further than this angle classified as 'neutral'. The composition of neutral clusters was then analysed via the energy recorded in each of the three stacks of each constituent tower.

The information from stacks 1 and 2 (Energy greater than 30MeV in stack1 and a non-zero energy in stack2 of a tower was a pre-requisite to consideration.) was combined to form a common stack. Within this new stack towers with energy greater than their nearest neighbours were regarded as being local maxima. A nearest neighbour was defined to be any tower which had an edge or, in the case of clusters within the end caps, part of an edge common to the maximal tower. This definition is that of rectangular neighbours described in figure 4.3.

Maximal towers with an energy greater than 100 MeV were deemed to be the start of photon clusters. This threshold was intended to reject signals in the ECAL

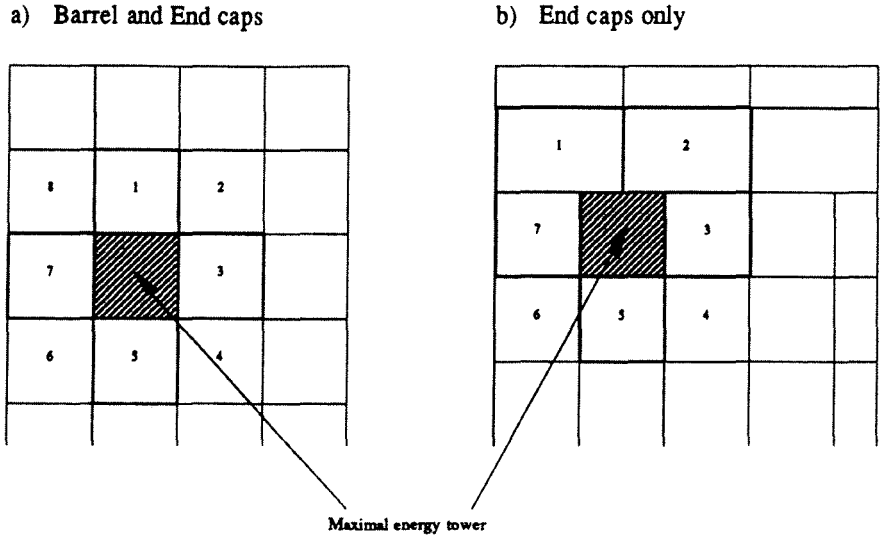

Figure 4.3: Definition of nearest neighbours. a) Towers 1,3,5 and 7 are rectangular nearest neighbours; towers 2,4,6 and 8 are diagonal nearest neighbours. b) Towers 1,2,3,5 and 7 are rectangular nearest neighbours and towers 4 and 6 are diagonal nearest neighbours

due to noise and to reduce misidentification of satellite clusters from hadronic interactions as genuine photons. The energy in all the nearest neighbours was added to the maximal tower energy and the coordinates of this tower (see section 2.11) were weighted in proportion to the energies in the surrounding towers to define the direction of the photon. Towers which were found to be the nearest neighbour of two or more local maxima had their energies shared between the maxima in proportion to the amount of energy in these maxima after summing the energy of all uncommon neighbours. Once the basis of a photon sub- cluster had been determined in this way, the total energy attributed to a reconstructed photon was estimated by dividing the total energy of the ECAL cluster in proportion to the summed energies of the local maxima.

Further cuts were then applied to differentiate 'fake' photons from genuine ones. As mentioned previously, collimation of particle jets can result in the overlapping of the charged particle and the daughter photons from the neutral pion. Therefore, to ensure that the energy deposited by the charged particle (if any) in the ECAL, including any secondary energy from the charged track impact on the

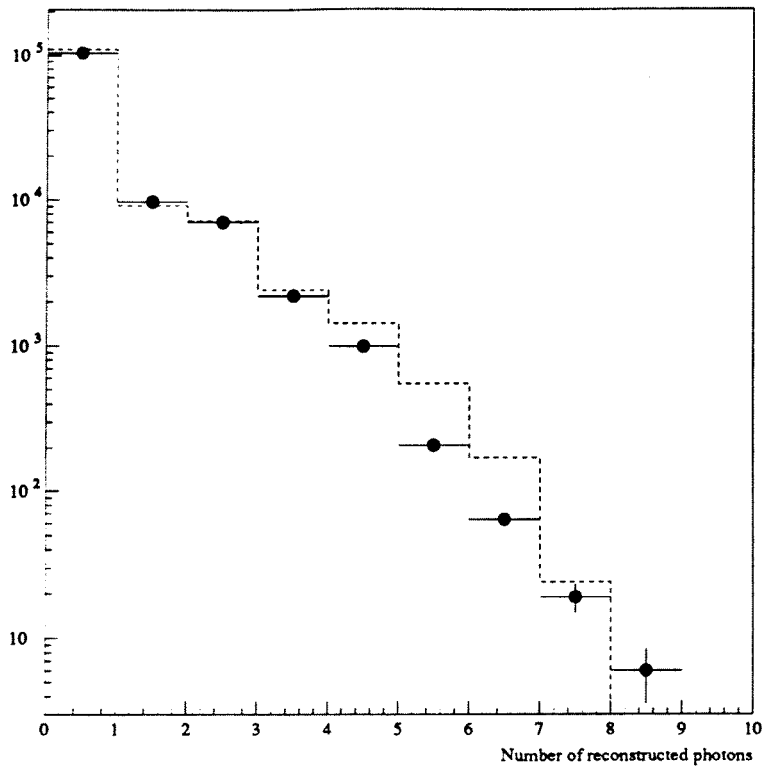

Figure 4.4: Number of reconstructed photons using the algorithm described in the text. The dashed histogram shows the Monte-Carlo normalised to the data (dots). Note the logarithmic y axis

ECAL present as a 'fake' peak within the JULIA cluster, was not mistaken for a photon, all sub-clusters were required to be further than 0.015 radians from the extrapolated charged track. The energy of any sub -cluster at an angle smaller than 0.015 radians was assumed to be due to the charged particle and was thus subtracted from the total energy of the ECAL cluster before sharing it amongst the remaining local maxima.

It is highly unlikely that a very asymmetric π^0 decay results with both photons being detected in the same ECAL cluster. Thus, for any cluster which divided into smaller sub-clusters, those maxima which had only a small fraction of the energy of the largest peak could be regarded as 'fakes' and were probably satellite or secondary clusters produced by the impact of the real photon. The limit below which a local maximum was regarded as being unreal was taken to be 10% of the energy in the largest peak.

The results of such an identification process were compared with Monte- Carlo

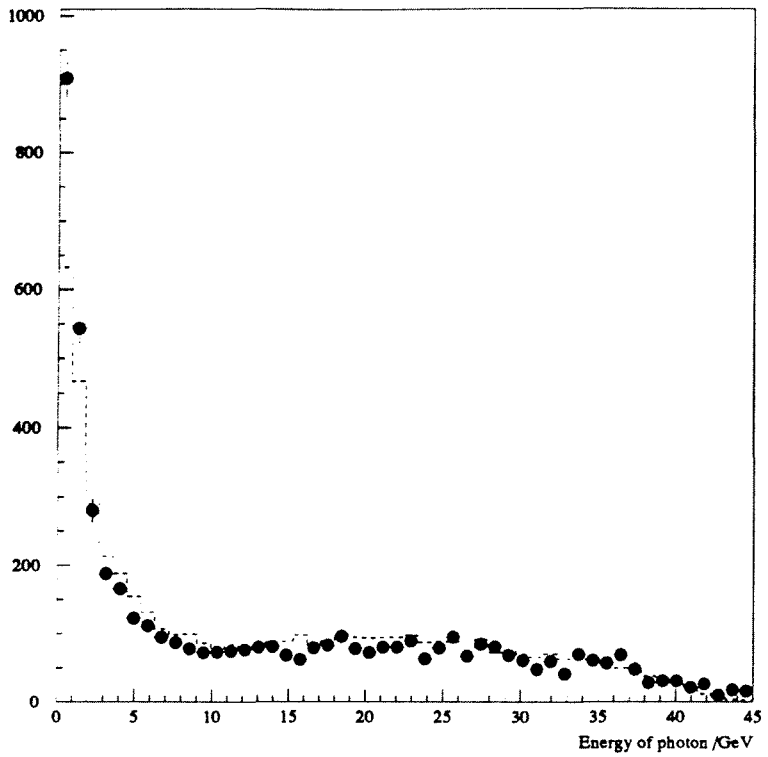

Figure 4.5: Reconstructed photon energy for one pronged hemispheres with one identified photon. The dashed histograms show the Monte-Carlo normalised to the data

data in order to estimate the validity of the method. Figure 4.4 shows the number of identified photons in real and Monte-Carlo data. There is good agreement for low photon numbers, but the discrepancy increases at higher multiplicities. This was probably due to the Monte- Carlo not simulating satellite clusters correctly, and due to incorrect branching ratios in the simulated data for events with several π^0's present. Rather than changing the Monte- Carlo, as this would be particularly difficult since branching ratios for tau decays involving several neutral pions are not known conclusively, the effects of such discrepancies were analysed in the systematic study (see chapter 6).

The reconstructed cluster energies for event hemispheres with one charged track and one and two identified photons are shown in figures 4.5 and 4.6 respectively. The histograms indicate a discrepancy at low energies between the Monte-Carlo simulated and the real data. Again, this was probably due to incorrect simulation of satellite clusters (which would characteristically have low energies.)

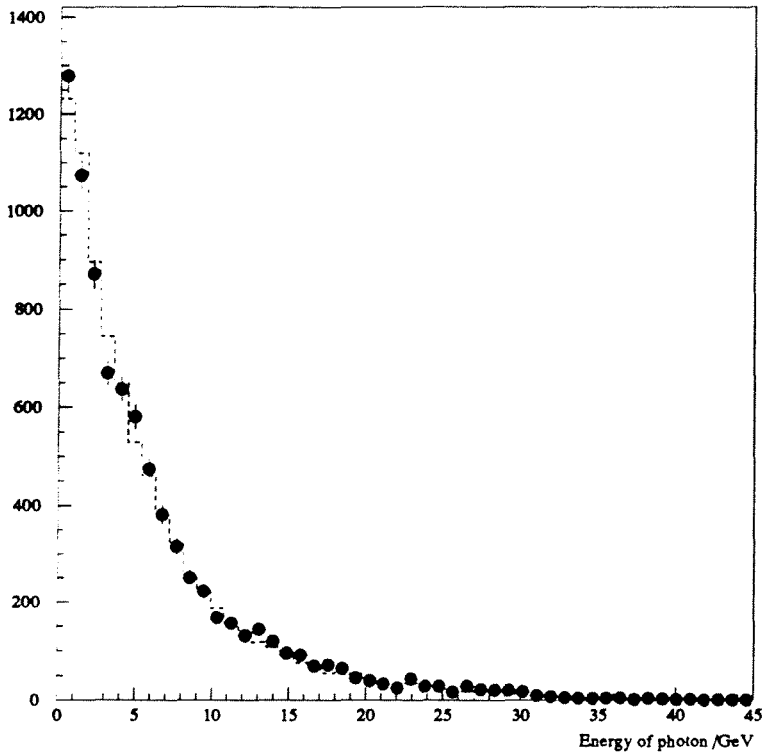

Figure 4.6: Reconstructed photon energy for one pronged hemispheres with two identified photons. The dashed histograms show the Monte-Carlo normalised to the data

4.4 The Rho Meson Sample.

The decay of a rho meson primarily into a charged and a neutral pion simplifies the topological selection of such events. The major complication arises from the detection of the neutral pion as discussed in the section 4.3.

All events in the general lepton sample described in section 4.1 with a 1-n (where n=1,3,5) topology were sampled for possible rho candidates.

In order to allow for the possiblity of converted photons, tracks which failed the D_0 and Z_0 cuts described in section 4.1 (classified as 'bad' tracks), were also considered. Hemispheres with a total of three charged tracks (one 'good' and two 'bad') were analysed for converted photons. The two 'bad' tracks were required to be consistent with an e^+e^- pair (using the estimators of section 4.2.1) and the third a hadron. The materialisation vertex of the e^+e^- candidate tracks and the kinematics of the possible parent photon were required to be such that the reconstructed mass was less than 100 MeV, the distance in the XY plane between

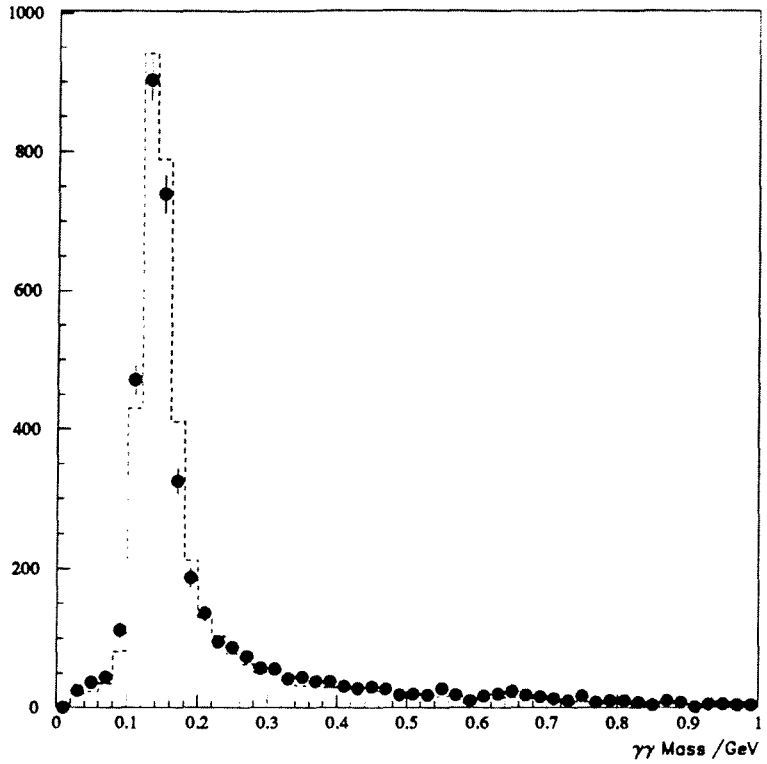

Figure 4.7: Two sub-cluster invariant mass distribution. The dashed histogram shows the Monte Carlo normalised to the real data.

the two tracks at the closest approach to the materialisation point was less than 1.0cm, the separation along z of the tracks from the same point to be less than 1.0cm and the polar radius at the materialisation point to be greater than 5.0cm [33]. Whenever these criteria were satisfied the combined properties of the e^+e^- tracks were subsequently treated as those of a photon.

Due to the complicated structure of the overlap regions, [10] (see figure 2.1), there is a severe reduction in resolution, therefore hemispheres with neutral energy detected by the ECAL in these regions were rejected.

Where a hemisphere with only one track was accompanied by exactly two reconstructed photons within a cone of 0.5 radians around the charged track, the invariant mass of the photons was required to be in the range $0.08 < M_{\gamma\gamma} < 0.20$ GeV. Figure 4.7 shows the two photon mass spectrum. A peak around the π^0 mass is clearly visible and in good agreement with the Monte-Carlo simulation. This agreement also indicates that the discrepancy in the reconstructed photon energies for hemispheres with two identified sub-clusters between Monte-Carlo simulation

and the real data, (figure 4.6), does not have a significant effect on the reconstruction of the π^0. For π^0 energies above the range 8 - 14 GeV (depending on the polar angle of the π^0 within ALEPH) the two daughter photons become increasingly more difficult to resolve as the energy of the parent is such that the photons are highly collimated and cannot be separated within the single cluster produced in the ECAL. The projective nature of the towers comprising the ECAL, means that slightly higher energy π^0's can be resolved near the regions where the ECAL barrel and end-caps overlap, hence the upper π^0 energy limit of 14 GeV.

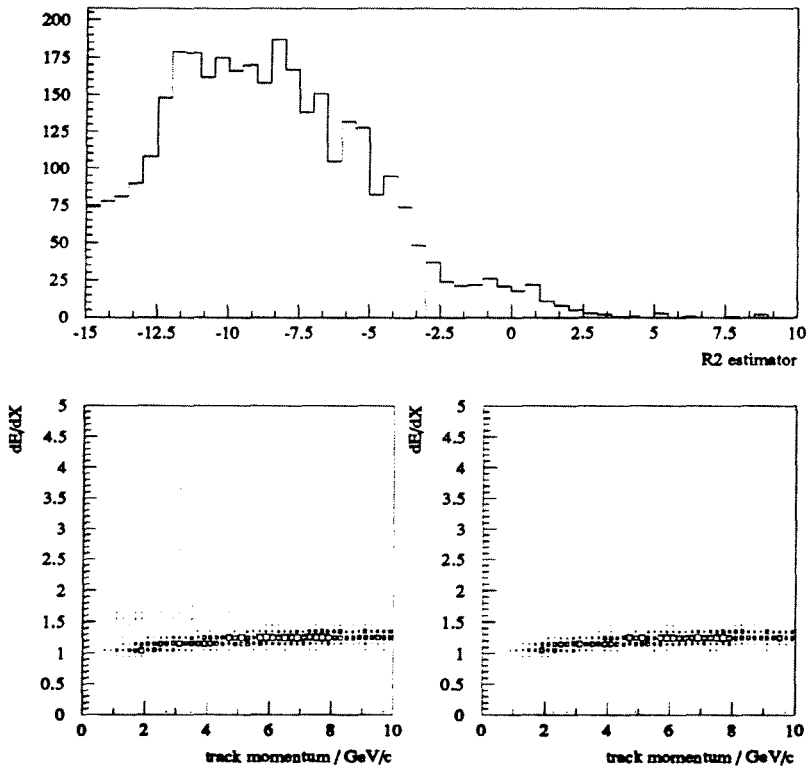

Figure 4.8: (a)(upper) R2 estimator for one pronged hemispheres after photon reconstruction cuts described in section 4.4. (b)(lower left) dE/dX versus track momentum plot for the same events as in figure (a). (c)(lower right) dE/dX versus track momentum plot after requiring tracks have R2$\leq$-3.0.

Therefore, to ensure such cases were not rejected and to reduce the acceptance of low energy π^0 decays resulting in the loss of one photon, hemispheres with only one reconstructed photon candidate were only accepted if the energy of the sub-cluster was greater than 3 GeV. This cut had the added effect that the discrepancy in the reconstructed photon energy for single cluster hemispheres observed between

Monte-Carlo and real data (see figure 4.5) was avoided.

Figure 4.8(a) shows the R2 estimator for hemispheres after the photon reconstruction cuts described above have been applied. Compared to figure 4.1(a) there is a dramatic reduction in the peak at zero corresponding to misidentified electrons/positrons. This is due to the reconstruction of the photons effectively tagging the charged track to be a pion. However, a small excess can still be seen around R2=0 (probably due to radiative $\tau \rightarrow e\nu\nu\gamma$ decays) thus, to eliminate misidentified electrons/positrons further, the charged track was required to have R$\leq$-3.0. The dE/dX information as a function of momentum, for the events in figure 4.8(a) is shown in figure 4.8(b). A band corresponding to the electron/positron excess is clearly apparent above the pion band. The same distribution is plotted again in figure 4.8(c) after the R2 cut has been applied. All the events in the electron/positron region of figure 4.8(b) have been removed and therefore there was not any need to use the dE/dX information in identifying the rho sample.

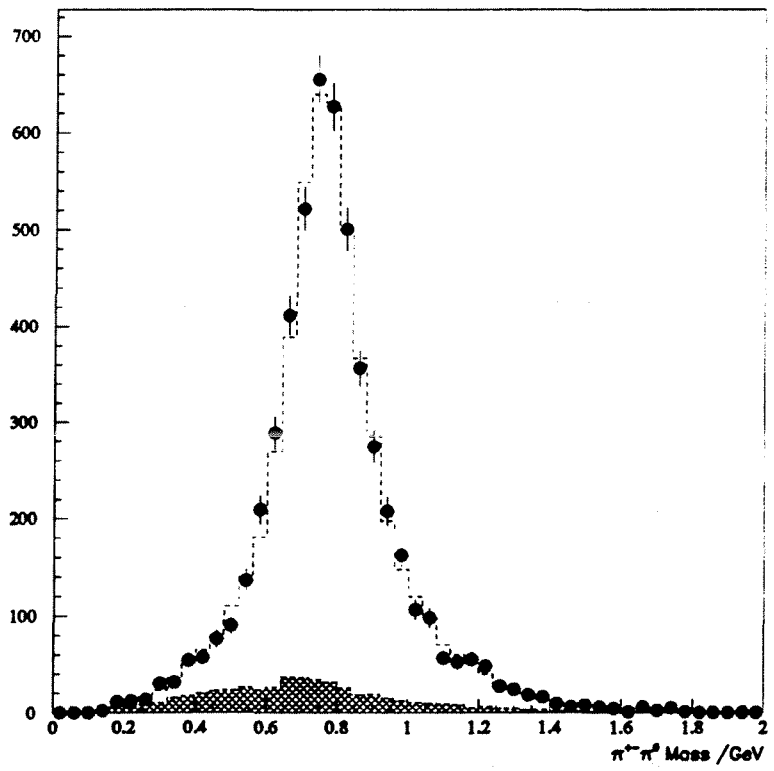

Figure 4.9: $\pi^{\pm}\pi^{0}$ invariant mass distribution. The dashed histogram shows the Monte Carlo normalised to the real data and the shaded plot shows the tau background.

In addition to these electron/positron rejection cuts, the charged tracks had to have the muon rejection estimator (see section 4.2.2 .2) such that 0.0>DFARL5>3.0.

The invariant mass of the charged track and the neutral pion candidate is shown in figure 4.9, a prominent peak is obvious around the rho resonance, again there is very good agreement with the Monte-Carlo simulation. The Monte-Carlo estimated tau background is also indicated in figure 4.9. The composition of this background is discussed in section 4.6. Due to the asymmetric distribution of this background around the rho peak the final sample was selected with a $\pi^{\pm}\pi^{0}$ invariant mass in the range $0.5 < M_{\pi^{\pm}\pi^{0}} < 1.2$ GeV.

As a final check against hadronic Z^0 decays and misidentified bhabha or $\mu^+\mu^-$ events, the hemisphere opposite the rho candidate was required to have an invariant mass less than 2.0 GeV and for cases with only one track in this hemisphere the momentum had to be less than 40 GeV/c and the ratio of the energy measured by the wire planes within the ECAL to the beam energy was to be less than 0.9.

The final sample left for the polarisation analysis consisted of 4593 rho candidates of which 10.4% was background (Both tau and non-tau decays. See section 4.6 for discussion.). The overall selection efficiency of this sample determined from Monte-Carlo data was 39.8%. Of the 4593 rho candidate hemispheres 51% had a fully resolved π^0 i.e. two identified sub-clusters, and 49% had both photons merged into a single cluster.

4.5 The a_1 Meson Sample.

All events which passed the preselection described in section 4.1 were sampled for three charged pion candidates. Topologically this may seem trivial, but there are a variety of interaction processes which can leave three tracks in the TPC. Of these, probably the most difficult to distinguish are those events which have three charged pions accompanied by some number of π^0's.

Each 3 prong candidate hemisphere was scanned for photons in a cone of half-angle 45^0 around the resultant charged track direction, using the photon reconstruction algorithm described in section 4.3.1. If any photons were identified then the hemisphere was rejected.

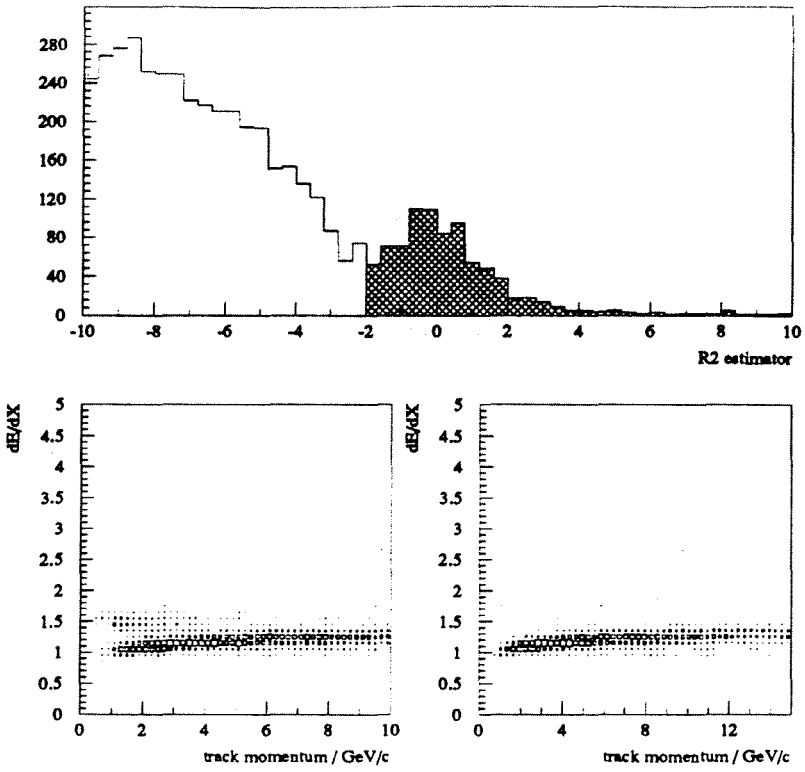

Figure 4.10: (a)(upper) R2 estimator for three pronged hemispheres after photon rejection. (b)(lower left) dE/dX versus track momentum plot for the same events as in figure (a). (c)(lower right) dE/dX versus track momentum plot after requiring tracks have R2$\leq$-2.0.

Also, as mentioned previously, photons radiated at some stage of the Z^0 decay process can convert to produce e^+e^- pairs, if the final decay product was a single charged particle, then this situation superficially appears to be a 3 pronged event. Conversion of photons from the decay of a π^0 can also make a one prong event (e.g. a tau decay to a rho meson) emerge as a 3 prong candidate.

To reduce these backgrounds electrons/positrons were again identified using the R2 estimator and where necessary and available the dE/dX information from the TPC, described in section 4.2.1. The R2 estimator for the three tracks in hemispheres satisfying the photon rejection requirement is shown in figure 4.10(a). Again, the peak at zero indicates the presence of electrons/positrons being included in the sample (most probably due to converted photons). Therefore, tracks were required to have an R2 value of less than or equal to -2.0. The dE/dX versus track momentum plot for events before this R2 cut (i.e. all events in figure 4.10(a)) is

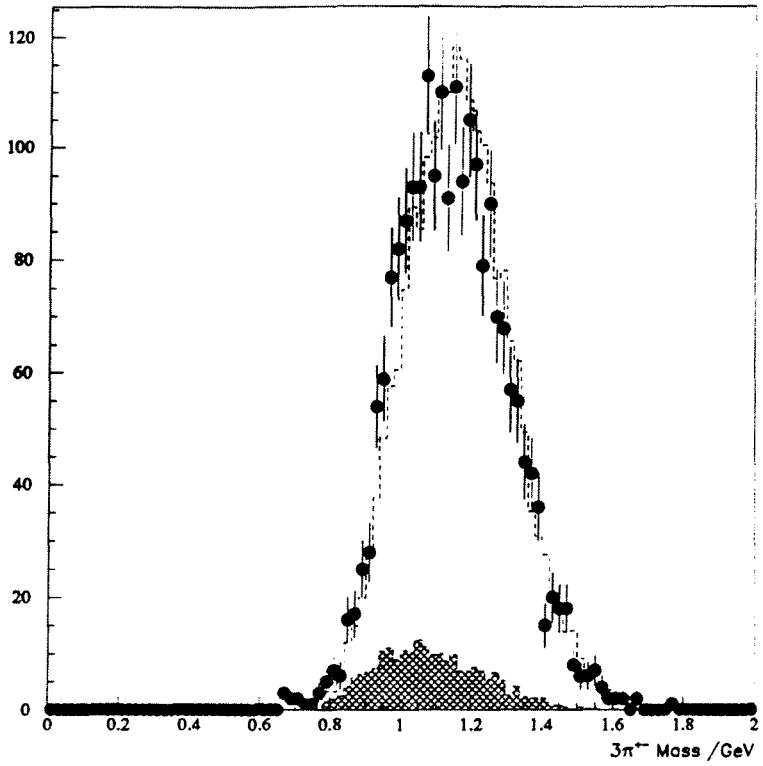

Figure 4.11: $\pi^{\pm}\pi^{\mp}\pi^{\pm}$ invariant mass distribution. The dashed histogram shows the Monte Carlo normalised to the real data and the shaded plot shows the tau background.

shown in figure 4.10(b). The two bands corresponding to electron/positrons and pions are distinctly apparent. The same plot for events surviving the R2 cut is shown in figure 4.10(c), although there is a reduction in the density of events in the $e^{\pm}$ band, some still remain. Thus, for tracks with momenta less than 3 GeV/c the ionisation density information was used as described in section 4.2.1.

If any of the three charged tracks failed the electron/positron cuts described above, the whole hemisphere was rejected.

The remaining three charged track invariant mass spectrum is shown in figure 4.11. A broad peak consistent with the a_1 resonance is seen which is in reasonable agreement with the Monte-Carlo. The width of the Monte-Carlo peak is slightly narrower than that of the data, but it is consistent within the determinations of the a_1 width [8]. Since the a_1 is known [47]-[51] to decay predominantly into three pions via a $\rho^0\pi^{\pm}$ intermediate state, one combination of the two $\pi^{\pm}\pi^{\mp}$ invariant masses should exhibit a ρ^0 peak, whilst the other should have a general phase

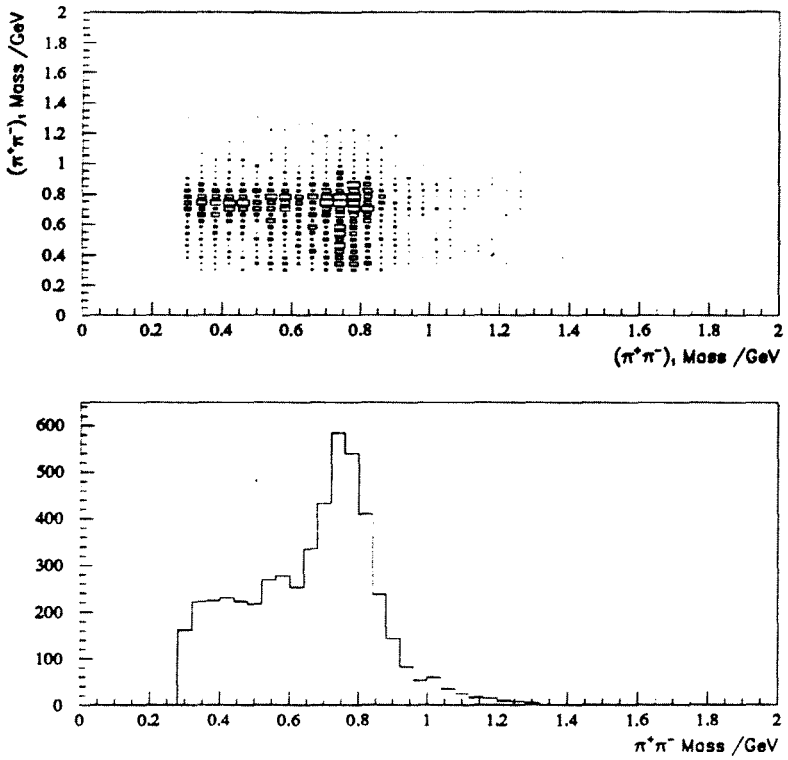

Figure 4.12: (a)(upper) Dalitz plot for the three prong data. (b)(lower) The two $\pi^{\pm}\pi^{\mp}$ combinations showing a clear peak at the ρ^0 mass

space distribution (assuming nothing 'exotic' occurred!). Figure 4.12(b) shows the two possible combinations and indeed there is a prominant peak at the expected mass. When these two combinations are plotted in the form of a Dalitz plot, bands in the regions of the ρ^0 can be clearly seen (figure 4.12(a)). Now, assuming that the decay of an a_1 meson into three pions without an intermediate resonance state has a small branching fraction (if it occurs at all!), requiring at least one of the $\pi^{\pm}\pi^{\mp}$ combinations to have an invariant mass in the range $0.6 < M_{\pi\pi} < 0.9$ GeV further reduced the background. Events which fail this cut were consistent with being those where a π^0 was present but the photons were not identified by the reconstruction algorithm.

The sample remaining for the polarisation analysis consisted of 2129 a_1 candidates of which 10.8% was background as determined from Monte-Carlo (see section 4.6). The overall selection efficiency of this sample determined from Monte-Carlo data was 51.5%.

The details of both the rho and a_1 samples are summarised in table 4.4.

4.6 Backgrounds to the Data Samples.

Any series of cuts devised to select a particular decay mode will inevitably allow some background events into the final sample. The extent to which these background modes contribute can in most cases only be determined from Monte-Carlo data where the generated mode is known (see chapter 2).

The backgrounds to the rho and a_1 samples (defined in sections 4.4 and 4.5) determined from Monte-Carlo data are tabulated in tables 4.1, 4.2 and 4.3, and discussed in the following sections.

4.6.1 Backgrounds from Tau Decays.

Table 4.1 shows that the major background to the rho sample was from $\pi^{\pm}2\pi^0$ and $\pi^{\pm}3\pi^0$ decays of the tau itself, (i.e. 73.41% of the overall tau decay background). Similarly the largest background contribution to the a_1 sample was from $3\pi^{\pm}\pi^0$ decays of the tau (i.e. 85.51% of the overall tau decay background). These components to both samples emphasises the difficulty in identifying neutral energy in a highly collimated jet environment. In the case of the multi-π^0 background to the rho sample the photons from one or more of the π^0's were not identified, either due to largely asymmetric π^0 decays resulting in the loss of the low energy photons or due to overlapping of photons into the same cluster, or of course a combination of the two possibilities.

The four pion background ($3\pi^{\pm}\pi^0$) to the a_1 sample was most probably due to overlapping of the neutral pion with the charged pions within the narrow cone defined by the jet.

Leptonic decays appear in the backgrounds most probably due to radiation of photons during the decay process. If the photon converts early then this would appear as a 3 pronged event and a background to the a_1 sample, otherwise it could appear as a rho event.

Also present as a background to the rho sample, were events with three or more charged pions in the same hemisphere.These were either disguised as conversions or some of the charged particles were lost down the beam pipe. The latter also explains the presence of large multiplicity charged pion hemispheres in the a_1

tau backgrounds to the rho sample	
Mode $\tau \rightarrow \nu_\tau +$	fraction of total
$\pi^\pm$ nπ^0, n=2,3	73.41%
K^*	18.46%
$\geq 3\pi^\pm$ nπ^0, n$\geq$0	3.38%
π,$K^\pm$	2.84%
lepton (e,μ)	1.91%

Table 4.1: Background contributions to the rho sample from other tau decay modes. The percentages shown are fractions of the overall tau background, i.e. 9.6%.

sample.

Although the decay of a tau lepton into kaons is Cabibbo suppressed, there is a small but definite branching ratio; (1.68±0.24)% for $\tau \rightarrow K\nu_\tau + \geq 0$ neutrals and (1.43±0.17)% for $\tau \rightarrow K^*\nu_\tau + \geq 0$ neutrals [8]. Since kaons subsequently decay into various combinations of charged and neutral pions it is easy to understand how these decays appear in the backgrounds of both the rho and a_1 samples.

4.6.2 Backgrounds from Non-tau Decays.

The possible backgrounds arising from non-tau decays are from $Z^0 \rightarrow q\bar{q}$, $Z^0 \rightarrow e^+e^-$, $Z^0 \rightarrow \mu^+\mu^-$, and $e^+e^- \rightarrow \gamma\gamma$ events. The extent to which these were present in the rho and a_1 samples was again determined by running the event selection algorithm detailed in sections 4.1 - 4.5 on Monte-Carlo events of the various types of decay. Table 4.3 shows the breakdown of these backgrounds.

When the rho and a_1 selection criteria were applied separately to 32000 $Z^0 \rightarrow q\bar{q}$, 30000 $Z^0 \rightarrow e^+e^-$, 10000 $Z^0 \rightarrow \mu^+\mu^-$, and 70000 $e^+e^- \rightarrow \gamma\gamma$ events, only one $Z^0 \rightarrow q\bar{q}$ event was selected by the rho reconstruction algorithm. No other

tau backgrounds to the a_1 sample	
Mode $\tau \rightarrow \nu_\tau +$	fraction of total
$3\pi^{\pm}\pi^0$	85.51%
K^*	8.14%
$> 4\pi^{\pm,0}$	4.83%
$\pi^{\pm}$ nπ^0, n=1,2	1.40%
lepton (e,μ)	0.13%
π,$K^{\pm}$	negligible

Table 4.2: Background contributions to the a_1 sample from other tau decay modes. The percentages shown are fractions of the overall tau background, i.e. 10.8%.

non-tau backgrounds		
	rho sample	a_1 sample
$Z^0 \rightarrow q\bar{q}$	0.8%	<0.14%, 95% C.L.
$Z^0 \rightarrow e^+e^-$	<0.06%, 95% C.L.	<0.14%, 95% C.L.
$Z^0 \rightarrow \mu^+\mu^-$	<0.06%, 95% C.L.	<0.14%, 95% C.L.
$e^+e^- \rightarrow \gamma\gamma$	<0.06%, 95% C.L.	<0.14%, 95% C.L.

Table 4.3: Background contributions from non-tau decay modes. The percentages are fractions of the overall data samples for the respective modes.

events were selected by either the rho or a_1 identification routines. When this one $Z^0 \rightarrow q\bar{q}$ event is scaled to the luminosity of Z^0 events analysed in the real data, it represents a non-tau background of 0.8% to the rho sample. The other non-tau backgrounds are negligibe. The upper limits shown in table 4.3(for both the rho and a_1 samples), are the number of events which could be observed with a statistical fluctuation compatible with zero at the 95% confidence limit.

4.7 $\tau \rightarrow \rho\nu_\tau$ and $\tau \rightarrow a_1\nu_\tau$ Branching Ratios.

As a consistency check and in order to get an idea of the quality of the selected data, the branching ratios for the decay modes $\tau \rightarrow \rho\nu_\tau$ and $\tau \rightarrow a_1\nu_\tau$ are calculated.

The branching ratio for mode i is given by :

$$BR_i = \frac{N_i(1-B)}{N_\tau}\frac{1}{\varepsilon_i} \tag{4.1}$$

where N_i is the number of identified hemispheres of mode i in the real data.

B is the background fraction from both misidentified tau and non-tau decays.

ε_i is the efficiency for selecting hemispheres of mode i. This includes all geometrical, detector and kinematical effects.

N_τ is the total number of tau hemispheres (i.e. twice the number of events) in the real data.

The total number of tau events was calculated from the total luminosity of events and the cross-sections for tau production at the various energy points around the Z^0 pole measured by the ALEPH collaboration [28]. The values inserted for the parameters in equation 4.1 to calculate the branching ratios are listed in table 4.4. The values for the branching ratios obtained are :

$$BR(\tau \rightarrow \rho\nu_\tau) = 22.18\% \pm 0.68(\textit{statistical})$$

$$BR(\tau \rightarrow a_1\nu_\tau) = 7.91\% \pm 0.31(\textit{statistical})$$

	rho sample	a_1 sample
number of candidate hemispheres, N_i	4593	2129
tau background	9.6%	10.8%
non-tau background	0.8%	negl.
total background, B	10.4%	10.8%
number of tau events, N_τ	46626±627	46626±627
Monte-Carlo branching ratio	22.55%	7.20%
Selection efficiency	39.8%	51.5%

Table 4.4: Summary of the data samples.

These values are in reasonable agreement with others published recently [8],[17], [18],[52]-[54] and [66],[67]. Thus there appears to be no indication of inconsistencies in the Monte Carlo which could produce large systematic effects in the polarisation measurements.

4.8 Examples of Tau Events.

Figures 4.13 and 4.14 show two typical tau events produced from Z^0 decays, displayed using the DALI event display package . In each of these figures the main picture shows an XY section (see section 2.11) through Aleph. The upper right-hand picture is a section through Aleph in the RZ plane for the same event and the lower right-hand picture shows a three dimensional projection of the TPC (see section 2.4) with the positions of the recorded hits and the reconstructed tracks.

In figure 4.13 the tau decay producing the single pronged jet shows a charged hadron passing through the ECAL with very little interaction before being stopped in the first few layers of the HCAL. This corresponds to a minimum ionising particle and is probably a pion (although no attempts are made to distinguish it from a

kaon). Near to this track is an energy deposit in the ECAL, the magnitude of which is indicated by the histogram plotted on the outer perimeter of the ECAL. Since, this deposit does not lie on the extrapolation of the charged track, it is probably due to a neutral particle such as a π^0. Thus, this hemisphere would reconstruct as a $\tau \rightarrow \rho\nu_\tau$ candidate.

The opposite hemisphere shows three charged tracks in the TPC, which are probably pions. However, here there is also an energy deposit in the ECAL which lies along the extrapolation of the three charged tracks. This energy cluster could be due to one or more neutral particles (e.g. π^0's) or it could be due to the overlap of energy deposits due to the charged tracks, conspiring to produce a large energy cluster. Hence, this hemisphere would require detailed analysis to distinguish it between $\tau^\pm \rightarrow a_1^\pm \nu_\tau$ and $\tau^\pm \rightarrow \pi^\pm\pi^\pm\pi^\mp\pi^0\nu_\tau$ candidate.

Figure 4.14 shows single charged tracks in both hemispheres; both depositing a very small amount of energy in the ECAL. These are minimum ionising particle candidates. The particles may be differentiated using the recorded hit patterns in the HCAL; i.e. one particle is stopped within the first few layers of the HCAL (therefore probably a charged pion), whereas the other continues to pass straight through the whole detector (therefore probably a muon). Thus, the two hemispheres are $\tau \rightarrow \pi\nu_\tau$ and $\tau \rightarrow \mu\nu_\tau\bar{\nu}_\mu$ candidates.

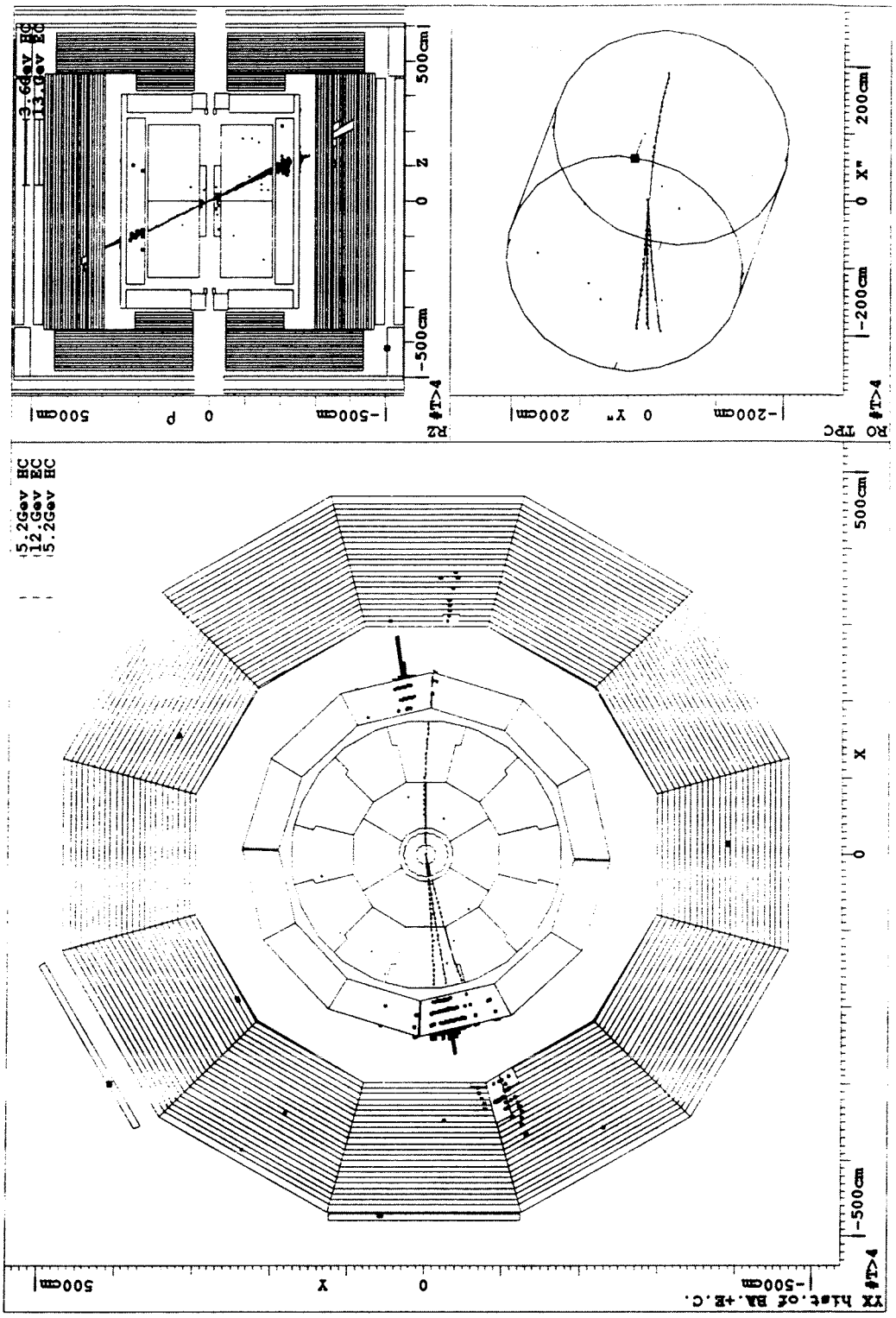

Figure 4.13: The single pronged hemisphere of this event is a $\tau^{\pm} \rightarrow \rho^{\pm}\nu_{\tau} \rightarrow \pi^{\pm}\pi^{0}\nu_{\tau}$ candidate. The three pronged hemisphere could be $\tau^{\pm} \rightarrow a_1^{\pm}\nu_{\tau} \rightarrow \pi^{\pm}\pi^{\pm}\pi^{\mp}\nu_{\tau}$, However the energy cluster in the ECAL would indicate that it is more probably $\tau^{\pm} \rightarrow \pi^{\pm}\pi^{\pm}\pi^{\mp}\pi^{0}\nu_{\tau}$.

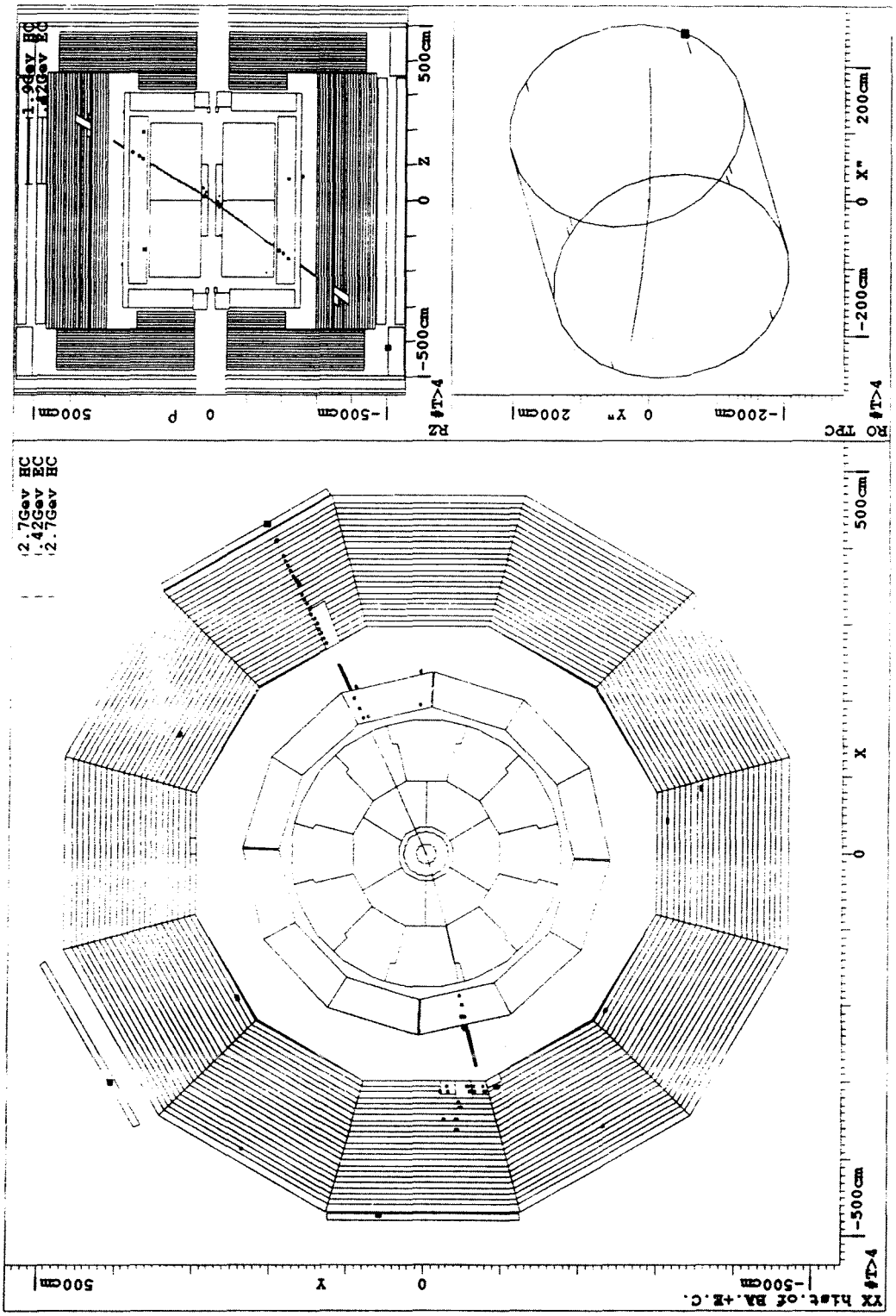

Figure 4.14: Both hemispheres of this event indicate the presence of a minimum ionising particle. However, the hemisphere where the particle passes straight through the HCAL is probably a $\tau \rightarrow \mu\nu_\tau\bar{\nu}_\mu$ event and the hemisphere where the particle is stopped within the HCAL is probably a $\tau \rightarrow \pi\nu_\tau$ event.

Chapter 5

The Polarisation Measurements.

5.1 The Fitting Method.

Since the helicity of each Monte-Carlo simulated tau event is recorded, the polarisation, P_τ, can be measured by fitting a linear combination of Monte-Carlo reconstructed distributions (in any polarisation variable) generated with positive and negative helicities to that obtained from the real data, with the polarisation as a free parameter.

The advantage in this method of using Monte-Carlo reconstructed distributions was that all QED initial and final state bremsstrahlung effects, background contributions and other apparatus effects were immediately corrected for by the Monte-Carlo generation and reconstruction process.

Thus a reconstructed distribution can be analysed in terms of its helicity components. To see how this can be done consider a two dimensional distribution reconstructed from real data (where the variables in the two dimensions are not yet specified). If the helicity of each event was known then the probability of an event of a tau decay mode k appearing in bin ij, in terms of the helicity contributions, is given by:

$$P_{ij} = \frac{N_{ij}^{+} + N_{ij}^{-}}{N_{tot.}^{+} + N_{tot.}^{-}} \tag{5.1}$$

where $N_{ij}^{\pm}$ is the number of real data events of mode k reconstructed with helic-

ity = ± 1 in bin ij, and $N^{\pm}_{tot.}$ is the total number of real data events of mode k reconstructed with helicity = ± 1.

The terms $N^{\pm}_{ij}$ and $N^{\pm}_{tot.}$ in equation 5.1 need to be related to the original number of events present before reconstruction in order to get the correct polarisation value. Thus, if initially there are N_τ tau events, then of these $N_\tau.BR_k$ will be of mode k (where BR_k is the branching fraction for mode k). If fraction x have positive helicity, then $x.N_\tau.BR_k$ will be the number of events of mode k with helicity = +1 originally present. Conversely, $(1-x).N_\tau.BR_k$ will be the number of events originally present with helicity = -1. Of course all of these events will not be reconstructed due to detection and identification inefficiencies. Thus, the number $N^{\pm}_{ij}$ can be written in the following way:

$$N^{\pm}_{ij} = \begin{pmatrix} \text{number of} \\ \text{events of mode} \\ k, \text{ with helicity} \\ = \pm 1 \text{ originally} \\ \text{present.} \end{pmatrix} \times \begin{pmatrix} \text{probability} \\ \text{of detecting a} \\ \text{mode } k \text{ event} \\ \text{in bin } ij \text{ with} \\ \text{helicity} = \pm 1 \end{pmatrix} \tag{5.2}$$

thus,

$$N^{+}_{ij} = (xN_\tau BR_k) \cdot \left(\varepsilon_\tau \frac{M^{+}_{rec.ij}}{M^{+}_{gen.}} \right) \tag{5.3}$$

and,

$$N^{-}_{ij} = ((1-x)N_\tau BR_k) \cdot \left(\varepsilon_\tau \frac{M^{-}_{rec.ij}}{M^{-}_{gen.}} \right) \tag{5.4}$$

where ε_τ is the efficiency for selecting a tau event, $M^{\pm}_{rec.ij}$ is the number of real data events correctly reconstructed with helicity = ± 1 in bin ij and $M^{\pm}_{gen.}$ is the total number of helicity = ± 1 events originally produced in the tau decays. Now, since ε_τ, $M^{\pm}_{rec.ij}$ and $M^{\pm}_{gen.}$ cannot be obtained from the real data (otherwise the analysis would be trivial!), they are determined from Monte-Carlo simulation in which the properties of the tau decays before reconstruction (i.e. at generation)

are known. P_{ij} then becomes the expected probability, $P_{ij}^{expec.}$ from the present theoretical understanding.

Substituting (5.3) and (5.4) into (5.1) and rearranging gives :

$$P_{ij}^{expec.} = \frac{xD_{ij}^{+}A^{+} + (1-x)D_{ij}^{-}A^{-}}{xA^{+} + (1-x)A^{-}} \tag{5.5}$$

where $D_{ij}^{\pm}$ and $A^{\pm}$ are determined from Monte- Carlo and defined by:

$$D_{ij}^{\pm} = \frac{M_{rec.ij}^{\pm}}{M_{rec.tot.}^{\pm}} \quad \text{and} \quad A^{\pm} = \frac{M_{rec.tot.}^{\pm}}{M_{gen.}^{\pm}} \tag{5.6}$$

From equations 5.6 it is apparent that $D_{ij}^{\pm}$ are the bin entries in the Monte-Carlo reconstructed distributions for helicity $= \pm 1$ normalised to unity and $A^{\pm}$ are the average acceptances for the two helicity states.

Equation 5.5 can be simplified further by introducing a change of variable such that :

$$x^{'} = \frac{xA^{+}}{xA^{+} + (1-x)A^{-}} \tag{5.7}$$

Then immediately we have :

$$P_{ij}^{expec.} = x^{'}D_{ij}^{+} + (1-x^{'})D_{ij}^{-} \tag{5.8}$$

Here, $x^{'}$ ranges from zero to one, just as x does.

Of course it is the fraction x which is related to the polarisation, P_{τ}. This is obvious from the definition of P_{τ}, i.e.

$$P_{\tau} = \frac{N_{gen.}^{+} - N_{gen.}^{-}}{N_{gen.}^{+} + N_{gen.}^{-}} = 2x - 1 \tag{5.9}$$

In terms of $x^{'}$ this becomes :

$$P_{\tau} = \frac{x^{'}a^{+} - (1 - x^{'})a^{-}}{x^{'}a^{+} + (1 - x^{'})a^{-}} \tag{5.10}$$

where $a^{\pm} = 1/A^{\pm}$.

The Monte-Carlo probability given by equation 5.8 determines the expected event distribution in the variables chosen. Fitting this Monte- Carlo profile to the equivalent real data distribution (normalised to one) gives a value for x', which when substituted into equation 5.10 yields a measured value for the average longitudinal polarisation of the tau. It should be noted that expression 5.8 is completely independent of the number of dimensions, and therefore applies to distributions in any number of variables.

Before going on to describe the results of implementing this method, the next section briefly discusses the importance of the acceptance, since it plays an important role throughout.

5.2 Acceptances.

It is important to know how any detection system followed by an event selection algorithm modifies the event distribution in any particular parameter, such as polar angle, track momentum etc. If either the detector or selection algorithm preferentially selects certain types of event over others then this would introduce a bias in the data sample which could have serious implications on the analysis being performed and would have to be corrected for. Also, it is important to know how efficiently the detection and event selection procedures work.

The above can be quantified by the *acceptance*, which is merely the ratio of the number of events of interest correctly reconstructed to the number originally generated. The acceptance in this form is of interest since it immediately gives the average selection efficiency, and indeed enters explicitly into the present analysis via equations 5.6. However, more information can be gained by displaying the acceptance as a function of various parameters such as the decay angles θ_{ρ/a_1} and

ψ_{ρ/a_1} (see chapter 3), or the variable Y, used for the polarisation measurement from the rho sample (see section 5.6).

As the definition suggests, the acceptance is a quantity determined from Monte-Carlo simulated data, thus, for it to be an accurate measure of the real acceptance very good Monte-Carlo simulation is necessary. The quality of the Monte-Carlo can be checked, as always, by comparing Monte -Carlo reconstructed distributions with those from the real data. Good agreement will immediately suggest that the acceptance is an accurate measure of the real value, as there is no reason to believe that the detector and the selection algorithm will manipulate the original data differently for Monte-Carlo and real data contriving to produce the same reconstructed distributions.

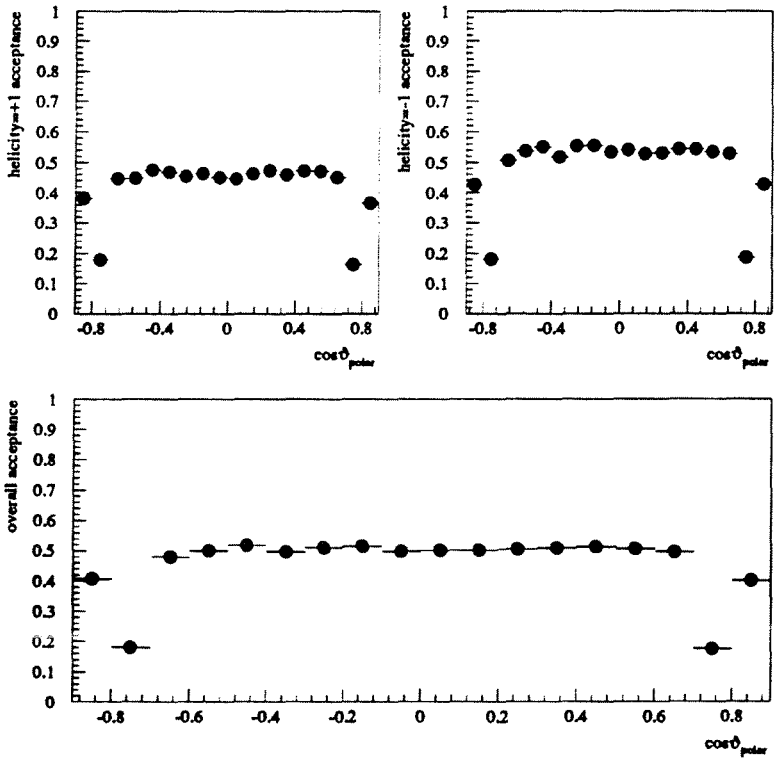

Figure 5.1: Acceptance as a function of polar angle for the rho sample. The upper left hand figure shows the variation in acceptance for events with helicity = +1, the upper right hand figure shows the variation for helicity = -1 events and the lower distribution is the overall acceptance.

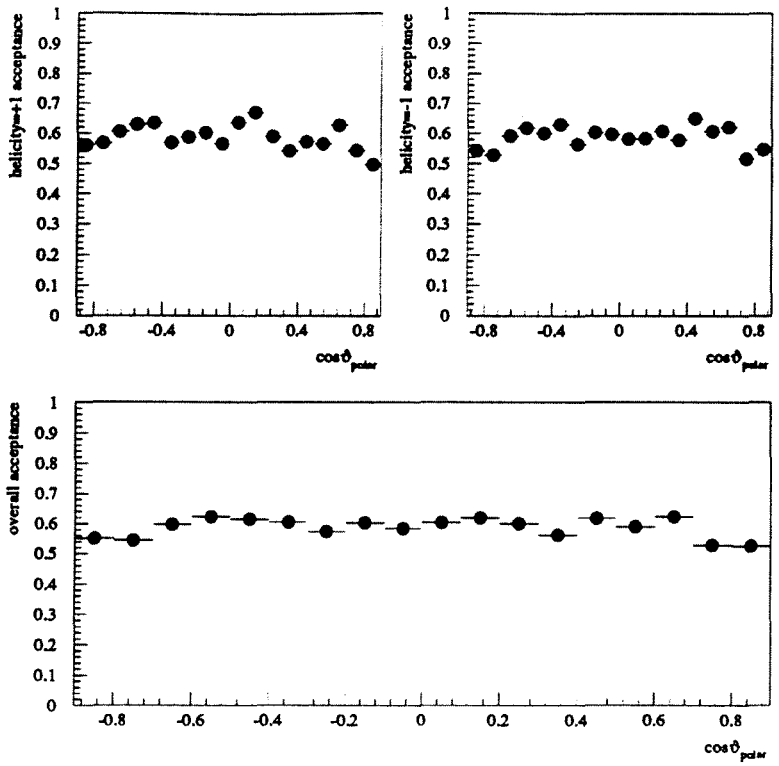

Figure 5.2: Acceptance as a function of polar angle for the a_1 sample. The upper left hand figure shows the variation in acceptance for events with helicity = +1, the upper right hand figure shows the variation for helicity = -1 events and the lower distribution is the overall acceptance.

5.2.1 Acceptance as a Function of Polar Angle.

The ALEPH detection system is symmetric in polar angle, θ_{polar} (see section 2.11), therefore it is reasonable to expect the acceptance of events for both rho and a_1 samples also to be symmetric in this angle. This in fact was the case as shown by figures 5.1 and 5.2.

In both of these figures the upper two distributions are for helicity = +1 (top left) and helicity = -1 (top right), the lower distribution shows the overall acceptance. For the rho sample (figure 5.1) there is a sharp decrease in acceptance for $|cos\theta_{polar}| \simeq 0.7$, this corresponds to the regions of the detector where the barrel and end-caps overlap. As was explained earlier, one pronged hemispheres with neutral energy in these regions were rejected (see section 4.3). The same is not true for the a_1 sample (see figure 5.2), since in this case it was not necessary to reconstruct the neutral energy into specific π^0's.

5.3 Polarisation Variables.

In chapter 3 it was explained how the sensitivity of the decay spectra from spin 1 hadronic products, to the tau polarisation, needs to be regained by reconstructing the spin configuration of the intermediate resonance state, i.e. whether the rho or a_1 was produced with a longitudinal or transverse spin configuration (see figure 3.2). It was also shown that this can be done in terms of the decay angles ψ_ρ and ψ_{a_1} defined in chapter 3 (angle definition diagram). Then the cosines of the two decay angles θ_{ρ/a_1} and ψ_{ρ/a_1} (see 3.2), allows reconstruction of spectra in two dimensions and thus provides the maximum information on the tau polarisation.

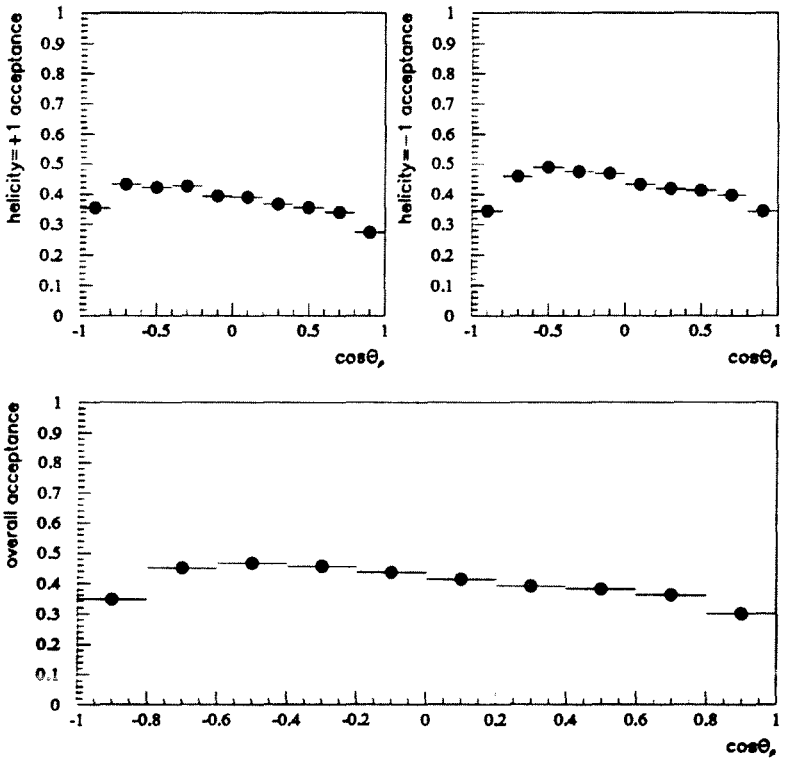

Figure 5.3: Acceptance as a function of decay angle $cos\theta_\rho$ for the rho sample. The upper left hand figure shows the variation in acceptance for events with helicity = +1, the upper right hand figure shows the variation for helicity = -1 events and the lower distribution is the overall acceptance.

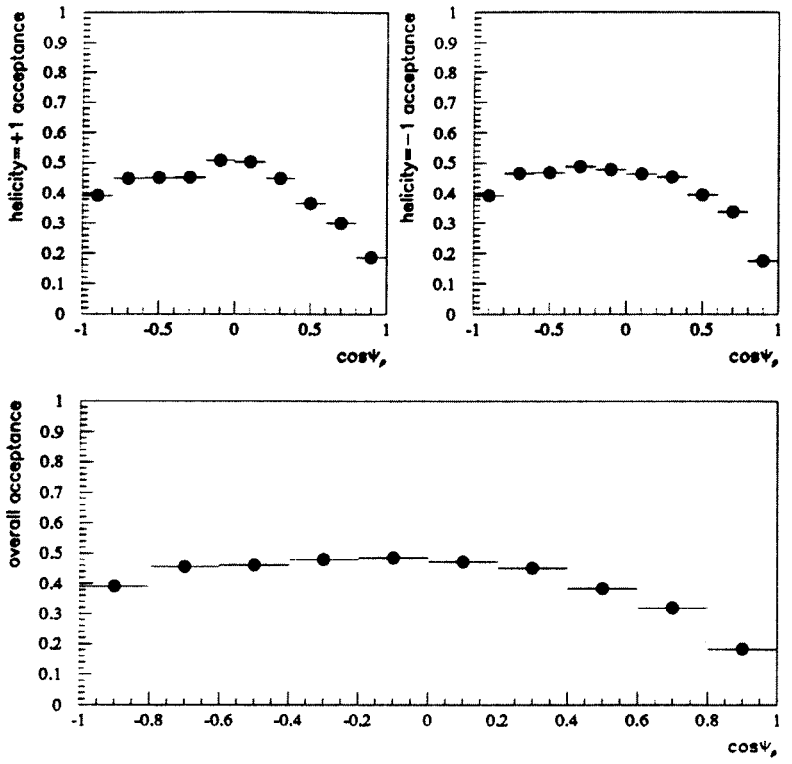

Figure 5.4: Acceptance as a function of decay angle $cos\psi_\rho$ for the rho sample. The upper left hand figure shows the variation in acceptance for events with helicity = +1, the upper right hand figure shows the variation for helicity = -1 events and the lower distribution is the overall acceptance.

5.3.1 Acceptances for the Decay Angles, $cos\theta_{\rho/a_1}$ and $cos\psi_{\rho/a_1}$.

Rho Sample Acceptances.

The acceptance as functions of the rho meson decay angles $cos\theta_\rho$ and $cos\psi_\rho$ (see figure 3.2 for definition of these angles) are shown in figures 5.3 and 5.4 respectively. The upper two distributions in both figures correspond to helicity = +1 (upper left) and helicity = -1 (upper right) events. They both show a similar trend over the $cos\theta_\rho$ and $cos\psi_\rho$ ranges.

The overall acceptance (shown in the lower distribution of figure 5.3) decreases with increasing $cos\theta_\rho$. Equation 3.5 indicates that at large $cos\theta_\rho$ values the energy of the rho meson is approximately the same as the energy of the initial tau from which it was produced. Thus, a highly energetic rho will produce a highly collimated jet in the final state. So the showers from the neutral and charged pions are

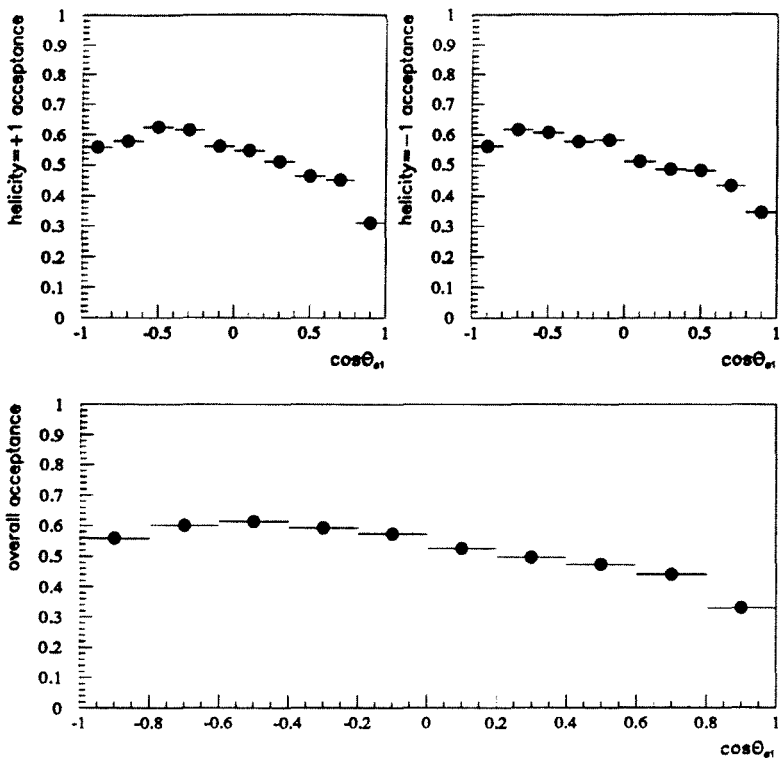

Figure 5.5: Acceptance as a function of decay angle $cos\theta_{a_1}$ for the a_1 sample. The upper left hand figure shows the variation in acceptance for events with helicity = +1, the upper right hand figure shows the variation for helicity = -1 events and the lower distribution is the overall acceptance.

greatly overlapped in the ECAL, hampering neutral pion identification and hence the drop in acceptance. At the other extreme, i.e. as $cos\theta_\rho$ tends to -1, the energy of the rho reaches only 41% of the energy of the initial tau and so the problem of overlapping electromagnetic showers has a lesser effect on particle identification. However, in this limit the rho has the lowest fraction of the tau energy, so effects due to photon losses from low energy π^0's have an increased effect and hence the observed reduction in acceptance.

a_1 Sample Acceptances.

The acceptance as functions of the a_1 meson decay angles $cos\theta_{a_1}$ and $cos\psi_{a_1}$ (see figure 3.2 for angle definitions) are shown in figures 5.5 and 5.6 respectively. Again the upper two distributions in both these figures correspond to helicity = + 1 (upper left) and helicity = -1 (upper right) events and the lower distributions

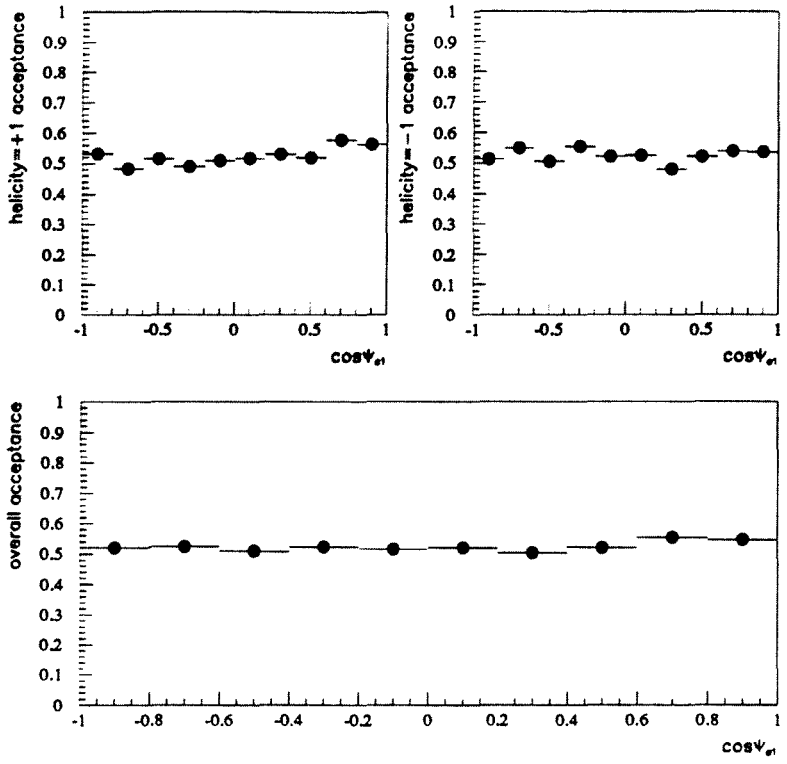

Figure 5.6: Acceptance as a function of decay angle $cos\psi_{a_1}$ for the a_1 sample. The upper left hand figure shows the variation in acceptance for events with helicity = +1, the upper right hand figure shows the variation for helicity = -1 events and the lower distribution is the overall acceptance.

are the overall acceptances. The acceptances for the two helicities show exactly the same trends for the respective decay angles. The acceptance across the $cos\psi_{a_1}$ range (figure 5.6) is flat within statistical fluctuations, with the same mean value for the two helicities. But for the $cos\theta_{a_1}$ distributions (figure 5.5) the acceptance decreases with increasing $cos\theta_{a_1}$ in a similar fashion to figure 5.3 for the rho sample. This can again be understood from equation 3.5, which indicates that for $cos\theta_{a_1} \simeq 1$ the energy of the a_1 is close to that of the initial tau. This means that the final pion tracks produced by an energetic a_1 will have on average, a large radius of curvature making the three tracks closer together. This then results in a decrease of track resolution within the TPC as a result of ambiguities from shared TPC hits. Again at the other extreme of $cos\theta_{a_1} \simeq -1$, the energy of the a_1 approaches only 41% of the energy of the initial tau, thus ambiguities from TPC track co-ordinates are less severe.

Hence, using distributions in $cos\psi_{\rho/a_1}$ and $cos\theta_{\rho/a_1}$, the polarisation values obtained using the method described in section 5.1 were :

$$\text{from rho sample :} \quad P_\tau = -0.096 \pm 0.037(\textit{statistical})$$

$$\text{from } a_1 \text{ sample :} \quad P_\tau = -0.067 \pm 0.113(\textit{statistical})$$

The uncertainties given above include effects from both Monte- Carlo statistics and real data, and from the acceptances calculated from the Monte-Carlo data.

5.4 Finding the Best Fit.

When comparing the Monte-Carlo expected probability (given by equation 5.8) with that from the real data i.e. the real data distributions normalised to one, to determine the best value of x', two possibilities for comparison were available; either minimising chi squared, χ^2, or maximising likelihood. The first method tends to give erroneous values of χ^2 when the fluctuation in the number of entries between adjacent bins is comparable to the number of entries in these bins (this occurs in sparsely populated areas of the distributions). On the other hand, the likelihood method, which takes the product of probabilities from each bin, is weighted by the more heavily populated areas of the distributions, making it less susceptible to statistical fluctuations. For this reason the likelihood method was preferred when fitting the $cos\theta/cos\psi$ distributions. The maximisation was performed using the MINUIT software package [55]. All subsequent fits described in the following sections also used MINUIT.

5.5 Problems with the Two Dimensional Fits.

With any distribution produced from limited statistics, effects due to the binning of data into histograms can become significant and therefore need to be studied. By repeating the fitting procedure outlined above with differing numbers of bins in the $cos\theta/cos\psi$ histograms it was found that fluctuations in the polarisation

result from the rho sample were well within one statistical standard deviation (i.e. 0.037). But, for the a_1 sample, a variation in binning produced largely differing polarisation values, in many cases the fluctuations being much larger than one statistical standard deviation (i.e. 0.113), thus casting doubt on the above result.

In order to suppress these effects due to binning, the number of bins needs to be optimised (or ideally, the need for binning removed altogether), such that the underlying structure of the distribution is preserved while each bin remains reasonably populated. For the rho and a_1 channels this was made possible by further consideration of the theoretical energy spectra of the final state pions. The resulting distributions are discussed in the following sections.

5.6 Alternative Fit for the Rho Channel.

The theoretical distributions for the charged pion spectrum from the rho decay, in terms of the ratio of the pion energy to the rho energy, indicate that transversely polarised rho's tend to prefer equal division of the rho energy between the two decay pions, while longitudinal rho's lead to a largely asymmetric $\pi^{\pm}\pi^0$ energy distribution [40]. Since sensitivity can be regained by distinguishing these final state pion spin configurations, it has been shown [40] that a variable in terms of the difference in energy between the two pions from the rho decay normalised to the tau energy E_τ, is a good polarisation analyser. i.e.

$$Y = \frac{|E_{\pi^\pm} - E_{\pi^0}|}{E_\tau} \tag{5.11}$$

In this variable the energy of the tau, (E_τ) is approximated by the beam energy, (E_{beam}). Figure 5.7 shows Monte-Carlo generated events for taus with helicities of ± 1. These plots show significantly different distributions from which the sensitivity of this Y parameter is apparent. This figure also shows that the expected distributions for the two helicity states tend to have only a few events with high Y values. Therefore, to allow a chi squared minimisation fit to be performed, without any loss in sensitivity, the last bin was not included in the fits.

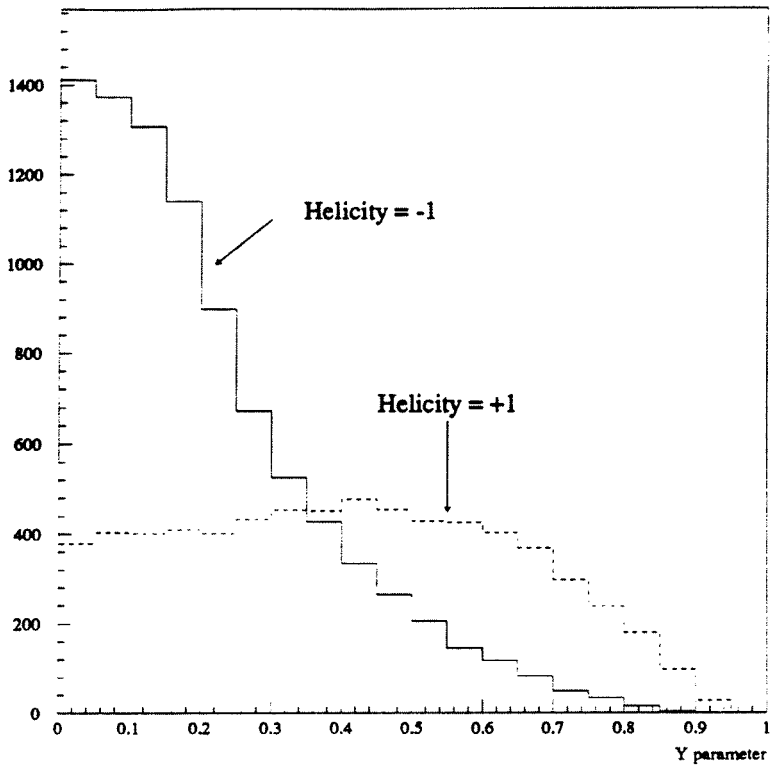

Figure 5.7: Y parameter for Monte-Carlo generated events.

5.6.1 Y Parameter Acceptance.

Figure 5.8 shows the acceptance as a function of the Y polarisation parameter used for the rho sample. The upper two figures correspond to the acceptances for helicity = +1 (upper left) and helicity = -1 (upper right). They both show a similar trend over the Y parameter range, but there is a slight difference in normalisation making the average acceptance for helicity = -1 slightly higher than that for helicity = +1 .

The lower distribution of figure 5.8 shows the overall acceptance. It can be seen that the acceptance decreases with an increasing Y value. Since the Y parameter is the difference in energies between the charged and neutral pions normalised to the energy of the corresponding tau (approximated by the beam energy) (equation 5.11), a large Y value corresponds to very asymmetric pion energies. A low energy neutral pion would produce at least one low energy photon which would probably escape identification even if it did appear within the restricted cone around the initial charged track direction. Conversely, a low energy charged pion would have a large curvature within the tracking detectors and the shower profile produced

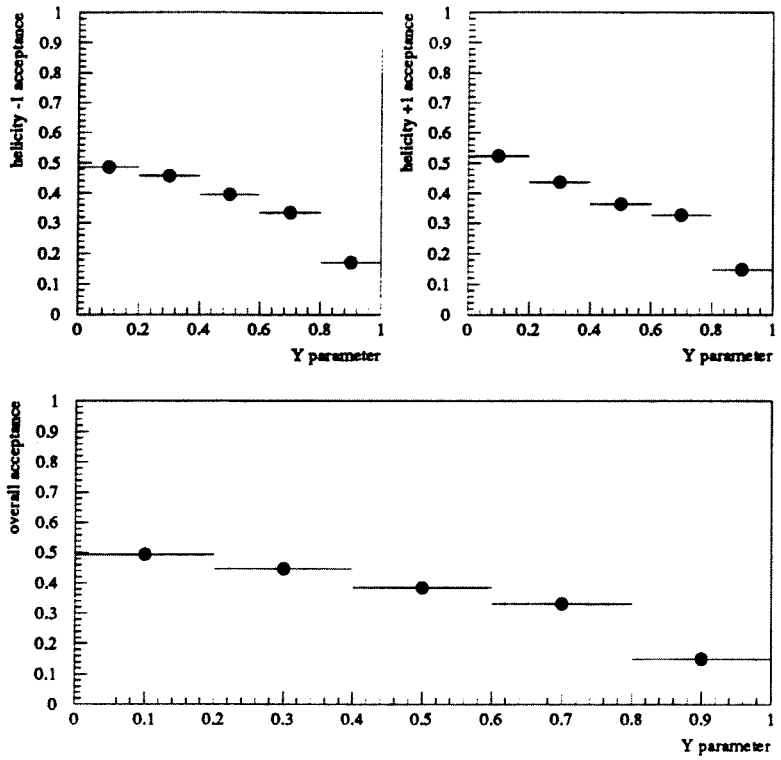

Figure 5.8: Acceptance as a function of the Y polarisation parameter for the rho sample. The upper left hand figure shows the variation in acceptance for events with helicity = +1, the upper right hand figure shows the variation for helicity = -1 events and the lower distribution is the overall acceptance.

within the calorimeters would be less like that of a minimum ionising particle, i.e. would correspond to a situation where the pion identification was poor (see section 4.2).

These factors result in a drop in acceptance at high Y values.

The polarisation obtained by using equations 5.8 and 5.10 with $D^{\pm}_{mc_i} \equiv Y^{\pm}_{mc_i}$ to fit the real data was :

$$P_\tau = -0.098 \pm 0.037(\textit{statistical}) \tag{5.12}$$

The uncertainty given above is the statistical uncertainty due to the real data and the Monte-Carlo. The χ^2 resulting was 18.7 for 18 degrees of freedom, indicating the quality of the fit. Figure 5.9 shows this result graphically, where the

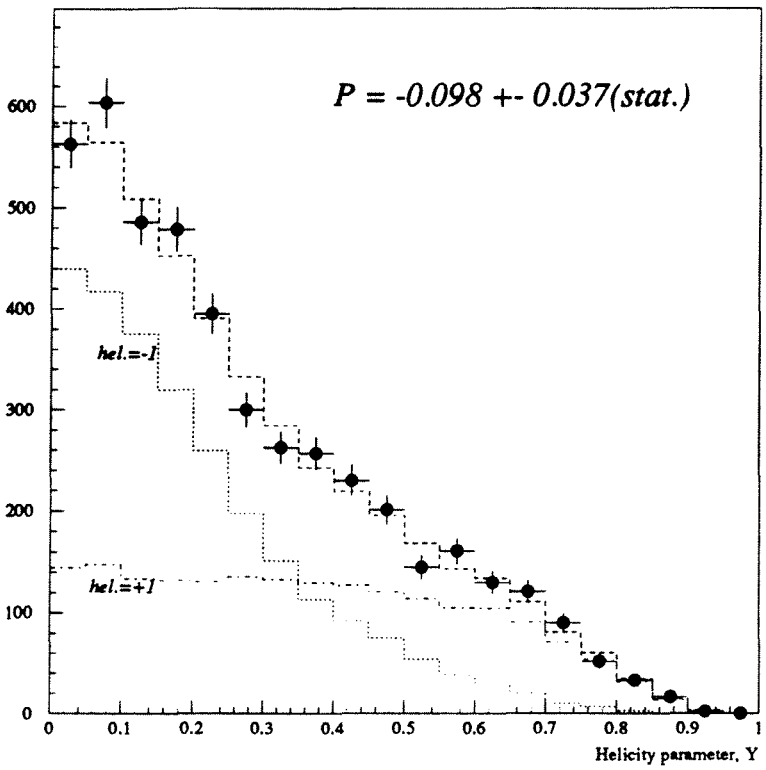

Figure 5.9: Y parameter fit result for the rho sample. The χ^2 for the fit was 18.7 for 18 degrees of freedom. The points correspond to the real data and the dashed lines are the results of fitting the Monte-Carlo data. The contributions from the individual helicity states to the overall fit are also shown.

contributions from the individual helicity states are also shown.

When the fits were repeated for different numbers of bins in the Y parameter range, the fluctuations observed were much smaller than the statistical standard deviation (i.e. 0.037) and also smaller than the fluctuations observed for the two dimensional $cos\theta/cos\psi$ fit. It is interesting to note that by using the Y parameter, a result of equal sensitivity compared to the $cos\theta/cos\psi$ fit is obtained, [40] with the added stability from binning only in one dimension. Therefore, this value obtained from the one dimensional fit was used as the final result from this channel.

5.7 Alternative Fits for the a_1 Channel.

The presence of three pions in the final state requires a more complicated projection of the two variables $cos\theta_{a_1}$ and $cos\psi_{a_1}$, in order to reduce effects from binning

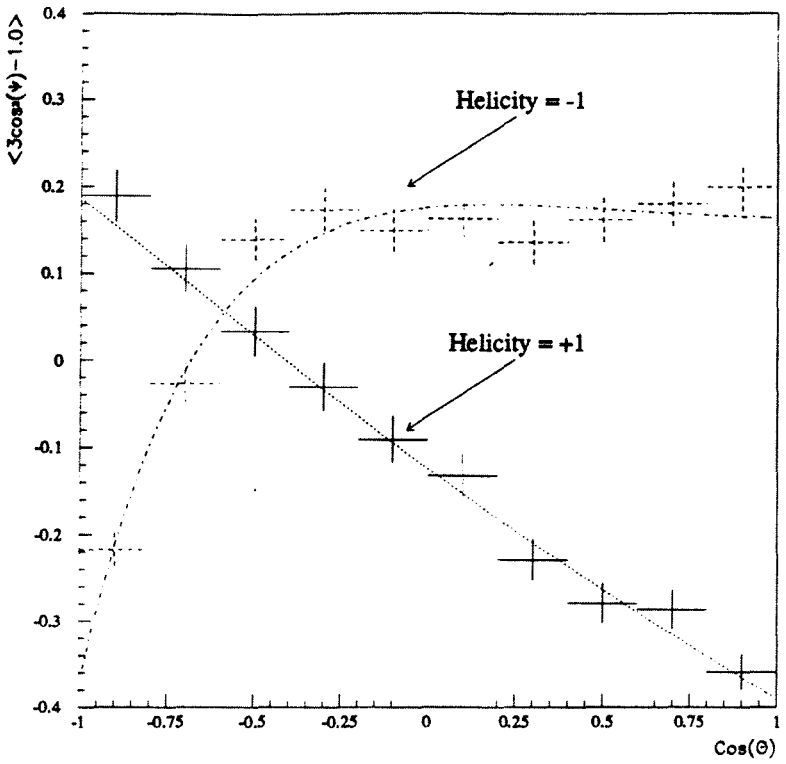

Figure 5.10: $< 3cos^2\psi - 1 >$ vs $cos\theta$ plots for Monte-Carlo generated a_1 events. The curves shown are the results of fitting the theoretical amplitudes.

while at the same time retaining sensitivity. It has been shown [42] that the moment $< 3cos^2\psi_{a_1} - 1 >$ projected as a function of $cos\theta_{a_1}$ has the desired effects. Figure 5.10 shows distributions in these variables for Monte-Carlo events generated (i.e. before reconstruction) with the two different helicity states. The sensitivity to the polarisation is clear from the two distinct distributions. The curves in this figure are the results of fitting the theoretical amplitudes. The polarisation values obtained were; +0.962±0.043 and -0.980±0.040 for events generated with helicity = +1 and helicity = -1 respectively.

In this instance a trivial application of equations 5.8 and 5.10 is not possible in the fitting procedure. This is apparent from the steps leading up to these equations. Consider each of the j $cos\theta$ bins of the real data distribution in turn. The moment in the jth bin is given by:

$$\bar{M}_j = \frac{\sum_i N_{ij}\omega_i}{N_j} = \frac{\sum_i (N_{ij}^+ + N_{ij}^-)\omega_i}{(N_j^+ + N_j^-)} \tag{5.13}$$

where the summation is over all $\omega_i = (3cos^2\psi - 1)_i$ values; N_{ij} is the number of reconstructed events in the $ijth$ bin and $N_j^{\pm}$ are the numbers of reconstructed events with helicity = ± 1 in the jth $cos\theta$ bin. The $N_{ij}^{\pm}$ terms are given by equations 5.3 and 5.4 and the $N_j^{\pm}$ terms are easily obtained from the same expressions by integration over $cos\psi$. As previously, $N_{ij}^{\pm}$ and $N_j^{\pm}$ as given by equations 5.3 and 5.4 cannot be obtained from the real data and are therefore again determined from Monte-Carlo simulation. $\bar{M}_j$ then becomes the expected moment in bin j, $\bar{M}_j^{expec.}$. Substituting these into expression 5.13 and rearranging in a similar fashion to the steps leading to equation 5.5 gives :

$$\bar{M}_j^{expec.} = \frac{x\bar{\Omega}_{rec.j}^{+}A_j^{+} + (1-x)\bar{\Omega}_{rec.j}^{-}A_j^{-}}{xA_j^{+} + (1-x)A_j^{-}} \tag{5.14}$$

where $\bar{\Omega}_{rec.j}^{\pm}$ and $A_j^{\pm}$ are determined from Monte-Carlo and defined by :

$$\bar{\Omega}_{rec.j}^{\pm} = \frac{\sum_i M_{rec.j}^{\pm}\omega_i}{M_{rec.j}^{\pm}} \quad \text{and} \quad A_j^{\pm} = \frac{M_{rec.j}^{\pm}}{M_{gen.}^{\pm}} \tag{5.15}$$

Thus, it is apparent that the acceptance terms $A_j^{\pm}$ now have an explicit dependence on $cos\theta$. Hence a change of variable as in equation 5.8 is not possible. Equation 5.14 now gives the expected $< 3cos^2\psi - 1 >$ values as a function of $cos\theta$, which are used to fit the equivalent moment distribution obtained from the real data to give a value for x. The polarisation value is then simply given by substituting x into equation 5.9. Minimising χ^2 using the MINUIT package to perform the fit resulted in a polarisation value of :

$$P_\tau = -0.005 \pm 0.123(statistical) \tag{5.16}$$

with a χ^2 of 14.4 for 9 degrees of freedom. The statistical uncertainty quoted above again includes contributions from both Monte- Carlo and real data statistics. This

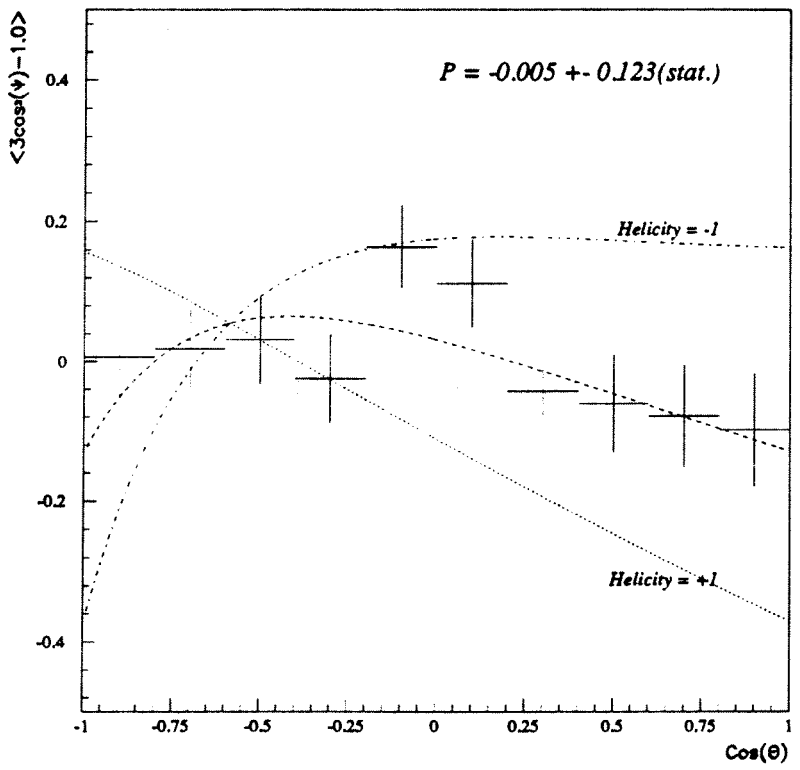

Figure 5.11: $< 3cos^2\psi - 1 >$ vs $cos\theta$ fit result for a_1 sample. The dashed line is the result of fitting a combination of Monte-Carlo reconstructed helicity $= \pm 1$ events to the real data (the points with error bars). The contributions of the individual helicity states are also shown.

result is shown in figure 5.11. Also shown are the Monte-Carlo reconstructed helicity = ± 1 curves contributing to the overall fit.

Of course, this result is not entirely independent of binning effects. To study the effect of these on the result, the fits were repeated with various numbers of bins. It was found that the large fluctuations observed in the two dimensional fits were greatly reduced, becoming smaller than one statistical standard deviation (i.e. 0.123).

However, it has been shown that a totally binning independent polarisation measurement can be obtained [42]. This is done in terms of the three moments, $< cos\theta_{a_1} >$, $< 3cos^2\psi_{a_1} - 1 >$ and $< cos\theta_{a_1}(3cos^2\psi_{a_1} - 1) >$. Following the same line of argument leading to equation 5.8, consider each of the three moments in turn (i.e. k=1,2,3 respectively), then if the helicity of each real data event is known, the measured moment value from the real data can be expressed as :

$$< M_k^{data} > = \frac{\sum_i N_i \omega_{ki}}{N_{tot.}} = \frac{\sum_i (N_i^+ + N_i^-)\omega_{ki}}{(N_{tot.}^+ + N_{tot.}^-)} \tag{5.17}$$

where the summation is over all reconstructed real data events . This expression is the same as equation 5.13, except that equation 5.17 is no longer divided into j $cos\theta$ bins. The $N_i^{\pm}$ are again given by equations 5.3 and 5.4 (summed over the second index j), as are the $N_{tot.}^{\pm}$ terms (summed over both indices i and j), and the ω_k terms are :

$$\omega_k \equiv \begin{cases} cos\theta \\ 3cos^2\psi - 1 \\ cos\theta(3cos^2\psi - 1) \end{cases} \tag{5.18}$$

As with the previous polarisation analyses $N_i^{\pm}$ and $N_{tot.}^{\pm}$ as given by equations 5.3 and 5.4, cannot be determined from the real data and thus Monte-Carlo simulated values must be used. Substituting for $N_i^{\pm}$ and $N_{tot.}^{\pm}$ into 5.17 and continuing the steps leading to equation 5.8 gives the expected values of the three moments as :

moment	Monte-Carlo rec. helicity = +1	Monte-Carlo rec. helicity = -1	Data
$< cos\theta >$	-0.076 ±0.535	-0.121 ±0.533	-0.081 ±0.536
$< 3cos^2\psi - 1 >$	-0.095 ±0.860	+0.093 ±0.917	+0.017 ±0.902
$< cos\theta(3cos^2\psi - 1) >$	-0.069 ±0.467	+0.041 ±0.487	-0.015 ±0.477

Table 5.1: Moments values for Monte-Carlo reconstructed and real data events.

$$< M_k^{expec.} >= x' D_k^+ + (1 - x') D_k^- \tag{5.19}$$

where $D_k^{\pm}$ are determined from Monte-Carlo and given by:

$$< M_k^{expec.} >= \frac{\sum_i M_{rec.i}^{\pm} \omega_{ki}}{M_{rec.tot.}^{\pm}} \tag{5.20}$$

x' is related to the polarisation by equation 5.10.

The calculated values for the moments as given by equation 5.20 are given in table 5.1 for both the Monte-Carlo reconstructed helicity = ± 1 events and for the real data.

The value of x' which results in the best fit of the Monte-Carlo moments to the real data moments was determined by performing a χ^2 minimisation using the values in table 5.1. Equation 5.10 then gives the polarisation value from this method to be :

$$P_\tau = -0.010 \pm 0.145(statistical) \tag{5.21}$$

Again, the statistical uncertainty quoted above includes both Monte-Carlo and real data statistics. As expected there is a significant loss in sensitivity; apparent from the larger uncertainty compared to the result from the $< 3cos^2\psi_{a_1} - 1 >$ versus $cos\theta_{a_1}$ moment projection. However, this increase (i.e. 0.022) was in fact smaller than the fluctuations observed in the $< 3cos^2\psi_{a_1} - 1 >$ versus $cos\theta_{a_1}$ moment fit as a result of varying the number of bins. For this reason the polarisation value obtained from this fit was taken as the final result from this channel.

Chapter 6

Systematic Study.

Any investigation into the possible sources of systematic uncertainties contributing to an experimental measurement will inevitably involve varying quantities essential to the mesurement and observing the fluctuations in the result of interest. Statistical analyses pose particular problems in that varying any selection cut necessary to define the final data sample will produce a different set of data. Consequently it must be distinguished whether any variation in the final result is due to a statistical fluctuation or due to a genuine systematic effect inherent in the analysis method. Of course, a pessimistic approach could be taken (as was for the analysis presented in this thesis) where any change observed is assigned as an upper limit to a systematic effect.

The possible sources of systematic uncertainty were investigated for both the rho and a_1 samples. The results of the study are discussed in the following sections and summarised in tables 6.3 and 6.4.

6.1 Sources of Systematic Uncertainty.

The algorithm used for photon identification was common to both the rho and a_1 samples, therefore the systematics from this process are discussed first before continuing to analyse the individual cuts unique to each decay mode in the subsequent sections.

6.1.1 (i) Photon Reconstruction Systematic Effects.

In attempting to identify photons using the algorithm of section 4.3.1, a minimum energy of 100 MeV was required for a storey to be classified as the starting point of a photon candidate. The aim of this threshold was to avoid confusing genuine photon clusters with 'fake' signals in the ECAL due to noise or satellites from hadronic interactions etc. These 'fake' clusters tend to appear randomly throughout the calorimeters with random 'energies' and so are difficult to simulate precisely. Evidence for a possible discrepancy between Monte -Carlo generated 'fake' clusters and those observed in real data is shown in figures 4.5 and 4.6. Here, for low energy values, there is a marked difference in the number of reconstructed photons; more clusters being identified in the real data sample than the Monte-Carlo. To search for a systematic effect, this energy threshold of 100 MeV was varied to 250 MeV and the fits repeated for both rho and a_1 samples .

Also, to avoid misidentifying clusters due to the charged track as photons, any reconstructed sub-cluster was required to be at least 15 mrads from the extrapolated charged track. At the other extreme, all identified photons were required to be constrained within a cone of 0.5 radians for the rho sample and 0.79 radians for the a_1 sample. A larger range was allowed for the a_1's due to the higher particle multiplicity in the final state producing wider jets. An upper limit on the angular range for photon acceptance was imposed again to reduce risk of misidentifying 'fakes' due to noise etc.. The lower limit on the angle range was changed to 30 mrads for both samples and the upper limit varied within suitable bounds.

The combined effect of these variations in energy threshold and angular ranges produced a shift of $|\Delta P| \sim 0.013$ for the rho sample and $|\Delta P| \sim 0.05$ for the a_1 sample.

In the clustering algorithm used, towers which had a common face (or part of a face) to the maximal tower (see fig.4.3) were regarded as nearest neighbours. This represents a quantisation of the photon energy with the assumption that more energy is likely to propagate into neighbouring towers via a common face. Therefore summing the energies in these towers with the energy in the central tower will account for the majority of the energy of the original photon. A slightly

different quantisation can be achieved by changing the definition of a 'nearest neighbour', and thus any systematic bias introduced can be observed. Hence, the definition of nearest neighbour was changed to include all 'diagonal neighbours' to a maximal tower; the definitions of these towers are shown in figure 4.3. The change in the polarisation values induced in this way was $|\Delta P| \sim 0.010$ and $|\Delta P| \sim 0.003$ for the rho and a_1 samples respectively. A larger uncertainty results for the rho sample since photon identification subsequently leads to specific reconstruction of a π^0, whereas for the a_1 sample it was merely necessary to identify the presence of genuine neutral energy.

6.1.2 Systematics for the Polarisation Measurement from the Rho Sample.

(a) π^0 Reconstruction.

In reconstructing π^0's the largest systematic was from situations where a π^0 produced only one neutral cluster in the ECAL. Here, a possible bias in the data could be due to the Monte-Carlo simulating photon 'losses' (where 'losses' includes merging of photons into single clusters) incorrectly. The hard cut at 3 GeV (above which single clusters were assumed to have two unresolved photons from the π^0), was varied between 2 GeV and 4 GeV. A shift of $|\Delta P| \sim 0.018$ was observed which was assigned as a systematic from this cut.

The invariant mass of exactly two reconstructed photons was required to be within the range $0.08 < M_{\gamma\gamma} < 0.20$ GeV. Although figure 4.7 shows very good agreement between Monte-Carlo and real data, the reconstruction was analysed further by comparing the $\gamma\gamma$ mass spectra for various π^0 energy ranges. The observed peaks were parameterised by fitting gaussians to both Monte-Carlo and real data samples separately.

Figure 6.1 show the results of this procedure. The figures indicate very good agreement between Monte-Carlo and real data. The upper figure shows that the mean value of the fitted gaussian to the mass spectra was reasonably constant up to a reconstructed π^0 energy of approximately 8 GeV. Above this energy the mean mass value progressively increases with increasing π^0 energy. This can be under-

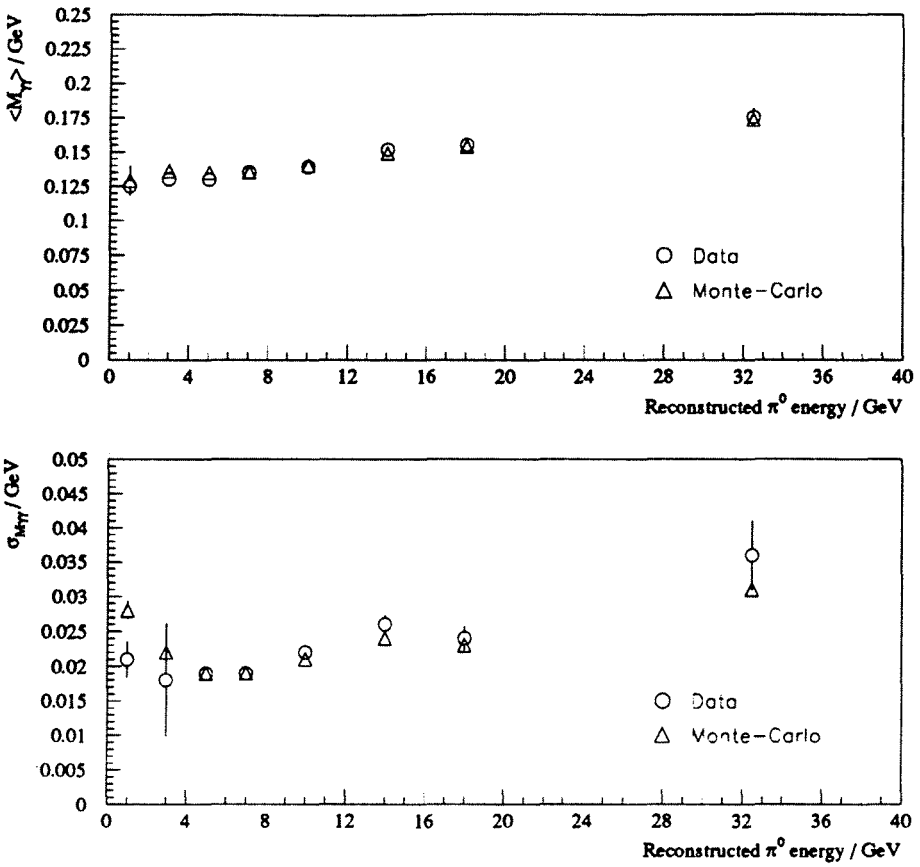

Figure 6.1: Results of parameterising two sub-cluster mass spectra for various π^0 energy ranges by fitting gaussians to the reconstructed peaks. The upper figure shows the variation in the mean value of each gaussian and the lower figure shows the corresponding width.

stood in terms of the minimum energy of 30MeV required in stack1 of each tower (see section 4.3.1), before consideration as part of a genuine photon. The energy deposited by a photon will be highest in the ECAL towers at the point of impact of the photon on the calorimeter. As the electromagnetic shower propagates through the ECAL layers, the energy recorded in neighbouring towers will decrease transversely from the initial photon direction. Eventually, the energy in the peripheral towers will become less than the thresholds imposed by the reconstruction algorithm. Since the energy thresholds are the same for all π^0 energies, they will represent a larger fraction of low energy π^0's than high energy π^0's. Consequently, the energy attributed to a reconstructed photon will have a more significant 'cut-off' on low energy π^0's. Hence the observed increase in the reconstructed π^0 mass.

It should be noted that this increase is within the π^0 mass range used for rho event selection, i.e. $0.08 < M_{\gamma\gamma} < 0.20$ GeV.

The widths of the fitted gaussians are shown in the lower distribution of figure 6.1. At low π^0 energies the fits suffer from poor statistics, due to factors such as the loss of a low energy photon, consequently the fitted gaussian width reaches a minimum between π^0 energies of 4 and 8 GeV, again consistent with the ECAL granular resolution available.

To study the effect of any systematic difference from the $\gamma\gamma$ mass acceptance, the mass range was defined in terms of the number of standard deviations of the fitted gaussian for each π^0 energy range, and varied within reasonable limits. The observed change in the polarisation value of $|\Delta P| \sim 0.003$ was taken as a systematic uncertainty.

(b) Charged Pion and Conversion Identification.

To identify charged pions as described in section 4.2 the electron/ positron discriminator, R2 was required to be less than or equal to -3.0 and the muon discriminator, DFARL5 to be in the range, 0.0>DFARL5>3.0. To estimate the systematic bias these cuts were varied. Obviously a large variation in the cuts will result in a large change in the final measurement, therefore variations which were considered suitable for each cut individually were applied.

Figure 4.1(a) shows a clear minimum at around R2$\sim$-3.0, whereas the minimum in figure 4.8(a) is closer to R2$\sim$-2.0. To study the effect of this estimator the R2 cut was varied around this minimum in the range -4.0$\leq$R2$\leq$-2.0.

Figure 4.2 shows the DFARL5 estimator after the preselection of section 4.1. Although the deviation in the distribution for DFARL5>0.0 is not as distinct as the minimum in the R2 distribution, a point-of-inflexion can be seen at around DFARL5$\sim$2.5. Tracks with DFARL5<0.0 (i.e. DFARL5 = -1.0), had no hits in the last 5 planes of the HCAL and therefore no shower could be parameterised. Thus, the effect of this muon estimator was observed by varying the upper limit of the DFARL5 range between 2.0 and 4.0.

In reconstructing converted photons, electrons and positrons needed to be iden-

tified. Three pronged hemispheres were required to have exactly two tracks consistent with an electron and a positron with the third a pion. The R2 estimator was again utilised to determine this. In addition the constraints imposed on the possible conversion were such that :

- the e^+e^- reconstructed mass was less than 100 MeV,
- the distance in the XY plane between e^+e^- tracks at the closest approach to the materialisation point was less than 1.0 cm,
- the separation along the Z axis of the e^+e^- tracks extrapolated to the materialisation point was less than 1.0 cm,
- the polar radius at the materialisation point was greater than 5.0 cm.

The R2 estimator was varied as described earlier. The cuts listed above were varied within the following limits :

- e^+e^- mass cut : 50 MeV - 20 MeV
- distance in XY plane : 0.5 cm - 1.5 cm
- distance along Z axis : 0.5 cm - 1.5 cm
- polar radius : 4.0 cm - 6.0 cm

These variations produced an overall change in the polarisation of $|\Delta P| \sim 0.008$, which was assigned as a systematic uncertainty. The breakdown of this value in terms of the individual changes is shown in table 6.1.

(c) Rho Reconstruction.

Once the π^0 had been identified it was combined with the charged pion and a cut placed around the rho peak (see figure 4.9). To estimate any effect of imposing a limitation on the charged/neutral pion invariant mass, the acceptance range (default, $0.5 < M_{\pi^\pm\pi^0} < 1.2$ GeV) was varied such that $(0.4 - 0.6) < M_{\pi^\pm\pi^0} <$

cut	systematic
$e^{\pm}$ rejection using R2 estimator	0.006
$\mu^{\pm}$ rejection using DFARL5 estimator	0.005
conversion identification	0.002

Table 6.1: Systematic uncertainties from charged pion and conversion identification for rho sample.

$(1.1 - 1.3)$ GeV. An upper limit on the possible systematic error was then taken to be $|\Delta P| \sim 0.012$

The final check against hadronic Z^0 decays, misidentified bhabha's and $\mu^+\mu^-$ events was to examine the hemisphere opposite the rho candidate. This hemisphere was required to have a total invariant mass less than 2.0 GeV. For one pronged hemispheres the ratio of the measured energy by the ECAL wire planes to the beam energy was required to be less than 0.9 and the track momentum less than 40 GeV. These were all varied and the changes considered as contributions to the systematic uncertainty are included in table 6.3.

6.1.3 Systematics for the Polarisation Measurement from the a_1 Sample.

(a) Photon/π^0 Reconstruction.

In contrast to the rho sample, only the presence of neutral energy within the ECAL needed to be positively identified to reject backgrounds from 3 pronged events with any number of π^0's, to the a_1 sample. Therefore the systematic uncertainty determined in section 6.1.1 due to the photon reconstruction process covered the systematic possibilities from neutral particle rejection and no further considerations were needed.

cut	systematic
$e^{\pm}$ rejection using R2 estimator	0.003
$e^{\pm}$ rejection using dE/dX	0.005

Table 6.2: Systematic uncertainties from charged pion identification for a_1 sample.

(b) Charged Pion Identification.

Electrons/positrons were identified and rejected as described in section 4.2.1 using the R2 estimator and in this case it was also necessary to use dE/dX information. In the same manner as described in section 6.1.2 for the rho sample, the R2 estimator was varied around the central value through the range -3.0≤R2≤-1.0, in order to study its effect on the polarisation value.

Where dE/dX ionisation information was used, a track was classified according to the larger probablility assuming it to be either an electron/positron or a pion (see section 4.2.1). Any systematic bias introduced by incorrect dE/dX information would appear as an incorrect probability for the corresponding particle hypothesis. Therefore, to estimate systematic effects, instead of classifying a track as that due to an electron/positron if

$$\text{probability(electron)} > \text{probability(pion)}$$

an electron/positron was identified if

$$\text{probability(electron)} > 1.2\ \text{probability(pion)}$$

and then if

$$\text{probability(electron)} > 0.8\ \text{probability(pion)}$$

In addition to these variations the momentum limit below which dE/dX information was used (default, 3GeV/c) was varied in the range 2 GeV/c<p<4GeV/c. The changes in the polarisation result are shown in table 6.2.

(c) Final a_1 Sample.

The final a_1 sample was defined assuming the decay proceeds entirely via a $\rho^0\pi^\pm$ intermediate state, the default mass range for the ρ^0 being $0.6 < M_{\pi\pi} < 0.9$ GeV. These limits were varied in the range

$$(0.55 - 0.65) < M_{\pi\pi} < (0.85 - 0.95)$$

producing a change in the polarisation value of $|\Delta P| \sim 0.033$.

6.1.4 Monte-Carlo Branching Ratios.

As discussed in chapter 4 it is necessary to understand the background modes contributing to the data samples and to ensure that there is correct simulation in the Monte-Carlo data sample. The majority of the backgrounds contributing to both the ρ and a_1 samples were from tau decays (see section 4.6). The branching ratios inserted into the Monte-Carlo generation procedure were taken from the world averages quoted by the Particle Data Group [8]. However, these values have recently been questioned by several collaborations including ALEPH [17, 18, 54] and therefore it was necessary to assign a systematic uncertainty due to these branching ratios.

The procedure adopted was to separate the background modes individually from the non-background mode within the Monte-Carlo, scaling the background before recombining it with the non-background sample and then repeating the analysis. For both the ρ and a_1 samples the backgrounds were scaled by a conservative 50%, producing changes in the polarisation values of 0.002 and 0.003 respectively.

6.1.5 Energy and Momentum Calibrations.

Although the calibrations of the TPC and the ECAL were accurately known [10] any inconsistency between the Monte-Carlo and real data still needed to be investigated. This was done by separately scaling all ECAL energies and track momenta in the Monte-Carlo only by $\pm 0.2\%$. The changes induced in the polarisation value by such a procedure are listed in tables 6.3 and 6.4.

6.1.6 Further Check on Clustering Method.

The sources of systematic uncertainty discussed above (sections 6.1.1 - 6.1.5) cover all the major contributors to the overall value. However, it can be seen from tables 6.3 and 6.4 that the largest contributions to the systematic uncertainty comes from the clustering algorithm used to identify neutral energies from photons, (i.e. ± 0.024 for the ρ sample and ± 0.050 for the a_1 sample). This has also been the case for previous analyses of this type [56].

The validity of the clustering method was therefore further cross examined by comparing the polarisation values obtained using a different clustering algorithm altogether. The main aspects of this method are outlined in the following section.

The 'Gampek' Clustering Algorithm.

Here, again the neutral clusters identified in the ECAL by the ALEPH reconstruction program JULIA [32] were analysed in terms of the constituent towers. The essential difference between this technique and that described in section 4.3.1 was in the way the energy in an ECAL tower was assigned to a photon sub-cluster.

The definition of a nearest neighbour used in this algorithm was that adjacent towers must have a common face (or part of a face). This is the definition of 'rectangular neighbours' shown in figure 4.3 . Each of the three stacks of the ECAL were considered in turn. Firstly, local energy maxima were identified within stack 1. A storey was regarded as a local maximum if it had energy greater than all its nearest neighbours and its own energy was greater than 75 MeV. This tower was also required to be further than 2 cm from any charged track extrapolated to this stack. Once the local maxima had been identified the storeys surrounding them were in turn assigned to its neighbouring local maximum or storey (already assigned to a local maximum), with the highest energy. This was continued until all the storeys of stack 1 were assigned.

All the storeys of stack 2 were then considered. Here, storeys immediately behind an assigned storey in stack 1 were assigned to the same maximum as that of the storey in stack 1. Any remaining isolated storeys in stack 2 were considered as new local maxima, and the start of another photon sub-cluster if it had an

energy greater than 150 MeV and was further than 3 cm from tracks extrapolated to stack 2.

This procedure was finally applied to all the storeys in stack 3. Here, all remaining, unassigned storeys were considered to be the start of new photon sub-clusters if they had an energy greater than 200 MeV and was further than 4 cm from the extrapolated charged tracks.

The energy in maximal storeys which were closer to the charged tracks than the distances given above, and all other storeys assigned to them remained unassigned and were considered as due to the impact of the charged track.

Photons reconstructed in this way were then finally required to have a minimum energy of 250 MeV in stacks 1 and 2 (summed). Also, for one pronged hemispheres, the distance of the photon sub-cluster barycentre from the charged track extrapolated to stack 1 had to be greater than 2 cm. For three pronged hemispheres the distance of the photon sub-cluster barycentre had to be further than 4 cm from the resultant direction of the three charged tracks.

The Estimated Systematic Uncertainty.

The data samples defined by this alternative method will essentially be very different to the samples described in sections 4.1 - 4.5, although there will be a certain degree of overlap.

The changes in the polarisation values observed were :

$$\text{from rho sample :} \quad \Delta P = -0.006 \pm 0.017$$

$$\text{from } a_1 \text{ sample :} \quad \Delta P = -0.074 \pm 0.087$$

The uncertainties quoted are the statistical fluctuations expected from the difference in data samples. These changes are assigned as a further uncertainty due to the clustering algorithm, although the changes are within the expected statistical fluctuations.

Systematic	
MC branching ratios	0.002
Clustering:	
Energy threshold and angular range for cluster acceptance	0.013
Single cluster π^0 energy limit	0.018
Definition of nearest neighbours	0.010
π^0 mass range	0.003
ρ mass range	0.012
Charged pion identification	0.011
Momentum calibration	0.003
Ecal energy calibration	0.001
GAMPEK clustering	0.006

Table 6.3: Systematic uncertainties for the polarisation measurement from the rho sample.

6.2 The Overall Results

The results of the systematic study tabulated in tables 6.3 and 6.4, were combined in quadrature to produce the following overall results for the average longitudinal polarisation of the tau lepton :

from two pion final state : $P_\tau = -0.098 \pm 0.037(statistical) \pm 0.030(systematic)$

from three pion final state : $P_\tau = -0.010 \pm 0.145(statistical) \pm 0.098(systematic)$

Systematic	
MC branching ratios	0.003
Clustering:	
Energy threshold and angular range for cluster acceptance	0.050
Definition of nearest neighbours	0.003
Electron rejection	0.006
$\pi^{\pm}\pi^{\mp}$ mass range	0.033
Momentum calibration	0.003
Ecal energy calibration	0.001
GAMPEK clustering	0.074

Table 6.4: Systematic uncertainties for the polarisation measurement from the a_1 sample.

Chapter 7

The Polarisation Dependence on Polar Angle.

The polarisation results measured in the chapters 5 and 6 are those which are obtained when averaging over the polar angle, θ_{polar} . It has been shown [23, 57] that the polarisation in fact has a polar dependence described by :

$$P(cos\theta_{polar}) = \frac{P_\tau + P_Z \frac{2cos\theta}{1+cos^2\theta}}{1 + P_\tau P_Z \frac{2cos\theta}{1+cos^2\theta}} \tag{7.1}$$

where $P_\tau = -2v_\tau a_\tau/(v_\tau^2 + a_\tau^2)$ is the polarisation of the taus originating from an unpolarised Z^o and $P_Z = -2v_e a_e/(v_e^2 + a_e^2)$ is the polarisation of the Z^o from unpolarised beams. (This is equivalent to P_e in equation 1.124. Note the sign difference between equations 7.1 and 1.124 arises from the definition 1.119.) The angle θ in equation 7.1 is the angle of the τ^- with respect to the e^- in each event. The above expression is in fact only true at the Z^0 resonance, but studies have shown [23, 57] that at energies away from the Z^0 pole there is only a slight change in the polarisation .

To investigate this dependence the rho sample described in sections 4.4 was divided into several $cos\theta_{polar}$ bins and the Y parameter fit of section 5.6 carried out. (The two dimensional fit and the a_1 data sample suffer from a lack of statistics in each polar angle range and thus were not used.). The results of the fits are shown in figure 7.1. These were then fit to equation 7.1 assuming universality of

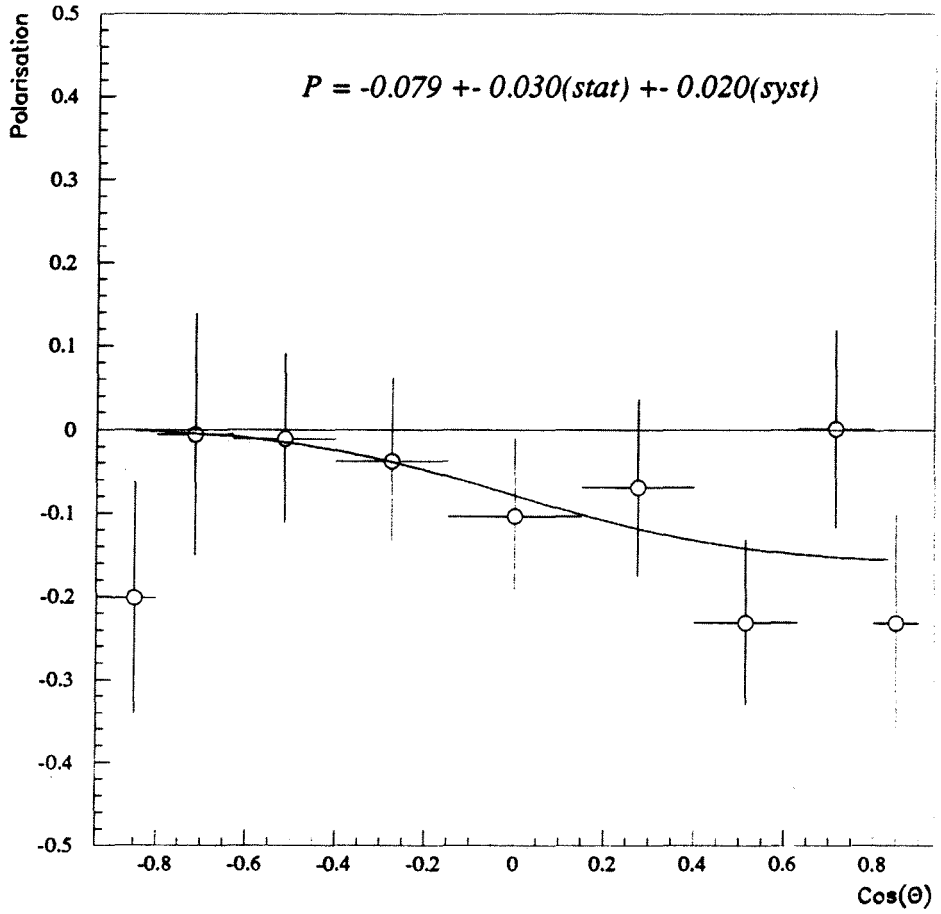

Figure 7.1: Polarisation versus cos θ_{polar}. The solid curve is a fit of equation 7.1 assuming lepton universality.

the Z^0 couplings to leptons, i.e. $P_\tau = P_Z = P_l$, the parameter varied in the fitting procedure. The fit resulted in a polarisation of

$$P_\tau = -0.079 \pm 0.030(statistical) \pm 0.020(systematic) \qquad (7.2)$$

Figure 7.1 shows this result graphically. The systematic uncertainty was determined by varying the polarisation measured in each $cos\theta_{polar}$ bin by the systematic uncertainty deduced from the analysis where the polarisation is averaged over all polar angles, (i.e. ± 0.030) described in chapter 6. The nature of equation 7.1 is such that at low $cos\theta_{polar}$ it is constrained to polarisation values close to zero (it is bound to exactly zero for $cos\theta_{polar}$ = -1) , when lepton universality is assumed. Consequently points at low $cos\theta_{polar}$ in the fit (i.e. the 'backward' direction) con-

tribute less to the overall result in that they are only permitted a very restricted variation during the fitting process. So, when the average value of the fitted curve is calculated to give P_l as the final result, the uncertainty is obtained essentially from only those points in the 'forward' direction (i.e. $cos\theta_{polar} \geq 0$). But , since these are averaged over the whole $cos\theta_{polar}$ range the uncertainties obtained from this method (both statistical and systematic) are smaller than those from the previous results of chapter 6.

By not assuming lepton universality, i.e. P_τ not necessarily the same as P_Z, a two parameter fit could be performed over the $cos\theta_{polar}$ range. This would allow separate measurements of the electron and tau couplings. However, for the data presented in this thesis, the point at $cos\theta_{polar}$ = -0.9 in figure 7.1 no longer becomes insignificant as was the case previously. This point in fact has quite a severe effect producing a rather poor two parameter fit. A larger data sample would improve the result and provide more information on the electron and tau couplings to the Z^0.

Chapter 8

Conclusions.

In this thesis, in excess of 48,000 tau events obtained from e^+e^- annihilations, during 1989 - 1991 data taking by the Aleph experiment have been analysed to provide measurements of the average longitudinal polarisation of the tau lepton, $< P_\tau >$.

A non-zero polarisation value is expected within the Standard Model due to the inequality of the Z^0 couplings to left- and right-handed leptons, i.e. due to parity violation arising from the chiral nature of the theory.

The average polarisation values measured in this thesis are given in table 8.1. Also listed in this table are the effective vector and axial vector coupling constants ($\hat{v}_\tau$ and $\hat{a}_\tau$ respectively) in the improved Born approximation calculated from :

$$< P_\tau >= \frac{-2(\hat{v}_\tau/\hat{a}_\tau)}{1+(\hat{v}_\tau/\hat{a}_\tau)^2} \tag{8.1}$$

and the effective weak mixing angle $sin^2\bar{\theta}_W$, calculated from :

$$\frac{\hat{v}_\tau}{\hat{a}_\tau} = 1 - 4sin^2\bar{\theta}_W \tag{8.2}$$

Table 8.1 also shows the values for the couplings, $\hat{v}_\tau$ and $\hat{a}_\tau$ obtained by combining equation 8.2 with :

	This Thesis			Aleph Results	
	(1) Rho sample	(2) a_1 sample	(3) Rho sample polar fit.	(4) Combined channels	(5) Combined channels polar fit.
P_τ	-0.098 $\pm$0.048	-0.010 $\pm$0.175	-0.079 $\pm$0.036	-0.144 $\pm$0.023	-0.135 $\pm$0. 017
$\frac{\hat{v}_\tau}{\hat{a}_\tau}$	+0.049 $\pm$0.024	+0.005 $\pm$0.088	+0.040 $\pm$0.018	+0.073 $\pm$0.012	+0.068 $\pm$0.009
$\hat{v}_\tau$	-0.025 $\pm$0.012	-0.003 $\pm$0.044	-0.020 $\pm$0.009	-0.037 $\pm$ 0.006	-0.034 $\pm$0.005
$\hat{a}_\tau$	-0.503 $\pm$0.002	-0.504 $\pm$0.011	-0.503 $\pm$0.002	-0.503 $\pm$0.002	-0.503 $\pm$0.002
$sin^2\bar{\theta}_W$	0.2377 $\pm$0.0060	0.2488 $\pm$0.0219	0.2401 $\pm$0.0045	0.2318 $\pm$0.0030	0.2330 $\pm$0.0022

Table 8.1: Values for the effective vector and axial vector couplings and the effective weak mixing angle, $sin^2\bar{\theta}_W$ calculated from the polarisation measurements in this thesis (columns (1), (2)and (3)), and the values obtained by Aleph from a weighted average of five tau decay modes and three different analysis techniques [56] (columns (4) and (5)). Columns (3) and (5) are the results of fitting the polar dependence of the polarisation assuming lepton universality.

$$\Gamma_\tau = \frac{G_F M_Z^3}{6\pi\sqrt{2}}(\hat{v}_\tau^2 + \hat{a}_\tau^2) \tag{8.3}$$

where, G_F is the Fermi constant, M_Z the mass of the Z^0 ($M_Z = 91.187 \pm 0.009$ GeV), and Γ_τ the partial width for Z^0 decays to taus ($\Gamma_\tau = 84.22 \pm 0.48$ MeV). Both M_Z and Γ_τ are the values measured by the Aleph collaboration [58]. It should be noted here that despite the sign ambiguity arising from the quadratic dependence of $\hat{a}_\tau$ in equation 8.3, it is taken to be negative, consistent with other measurements from Aleph [28] and from neutrino- electron scattering experiments [59].

Of the measurements presented in this thesis, parity violation in $e^+e^- \rightarrow Z^0 \rightarrow \tau^+\tau^-$ decay is apparent from the non-zero polarisation value obtained using the rho sample. This is not conclusive from the measurement using the a_1 sample, where the polarisation result is consistent with being zero.

The polarisation measurements obtained by Aleph are also listed in table 8.1. The combined channel result is a weighted average using results from tau decays into the five channels, $\tau \rightarrow e\bar{\nu}_e\nu_\tau$, $\tau \rightarrow \mu\bar{\nu}_\mu\nu_\tau$, $\tau \rightarrow \pi\nu_\tau$, $\tau \rightarrow \rho\nu_\tau$ and $\tau \rightarrow a_1\nu_\tau$ [60]. In this analysis a more sophisticated particle identification method was adopted in conjunction with three different analysis techniques. These include an analysis based on kinematical cuts similar to that presented here; an acollinearity method where the polarisation is inferred from the angular correlations of the decay products of the two taus in an event; and a neural network method [60, 61]. However, the result (listed as number (4) in table 8.1) is consistent with those in this thesis within one standard deviation.

The value of P_τ obtained from its variation with $cos\theta_{polar}$ (and assuming lepton universality) is listed as result (3) in table 8.1, and the corresponding Aleph result is entry (5). The agreement between the two is slightly worse than the comparison of averaged measurements (entries (1), (2) and (4)), with the Aleph result lying within 1.6σ of the result in this thesis. However, since the data samples used in the Aleph analysis and this thesis are very different (i.e. the Aleph result involves several different decay modes), the value obtained here is acceptable.

The values for the axial-vector coupling $\hat{a}_\tau \equiv a_\tau(M_Z^2)$ listed in table 8.1 are consistent with the Standard Model value of approximately 0.5 (See table 1.2. Note that this value is at the Born-level and does not include any radiative corrections.)

A comparison of effective weak mixing angle measurements is shown in figure 8.1. This figure shows that the three values of $sin^2\bar{\theta}_W$ measured in this thesis (results (1),(2) and (3)) are consistent with results derived from the tau polarisation by the other LEP experiments (results (6) - (8) inclusive [65] - [67]). Also in this figure are values measured from the forward-backward asymmetry, (values (9) - (12) inclusive [68] - [70]). These are also in agreement with those of this thesis. Data point (13) is the first result from the SLD collaboration at the SLAC linear collider [72] , where $sin^2\bar{\theta}_W$ was derived from a measurement of the left-right asymmetry resulting from polarised e^+e^- beams. Their result is in very good agreement with those of this thesis. Finally, a comparison of $sin^2\bar{\theta}_W$ obtained from $b\bar{b}$ asymmetry (data point (14) in figure 8.1, [28]) is of interest since this analysis requires consideration of higher order diagrams involving virtual production of the top quark, which does not enter in the other asymmetry measurements. A consistency in $sin^2\bar{\theta}_W$ values further enhances the validity of the Standard Model as the theory which describes matter and its interactions .

8.1 Implications of $sin^2\bar{\theta}_W$ on the Top Quark and Higgs Boson Masses.

The masses of the top quark and the Higgs boson enter into the calculation of $sin^2\bar{\theta}_W$ via higher order radiative corrections [24], of the form given by equations 1.129 - 1.132. The Higgs mass dependence is logarithmic and small within the Standard Model [72].

The variation of $sin^2\bar{\theta}_W$ as a function of top quark mass, M_{top} is shown in figure 8.2 for the range 60< M_{Higgs} <1000 GeV [73] [1]. Also shown in this figure is the average value of $sin^2\bar{\theta}_W$ from figure 8.1. The intersection of the two bands

[1] This variation of $sin^2\bar{\theta}_W$ as a function of M_{top} can be generated using the *ZFITTER* program [74]

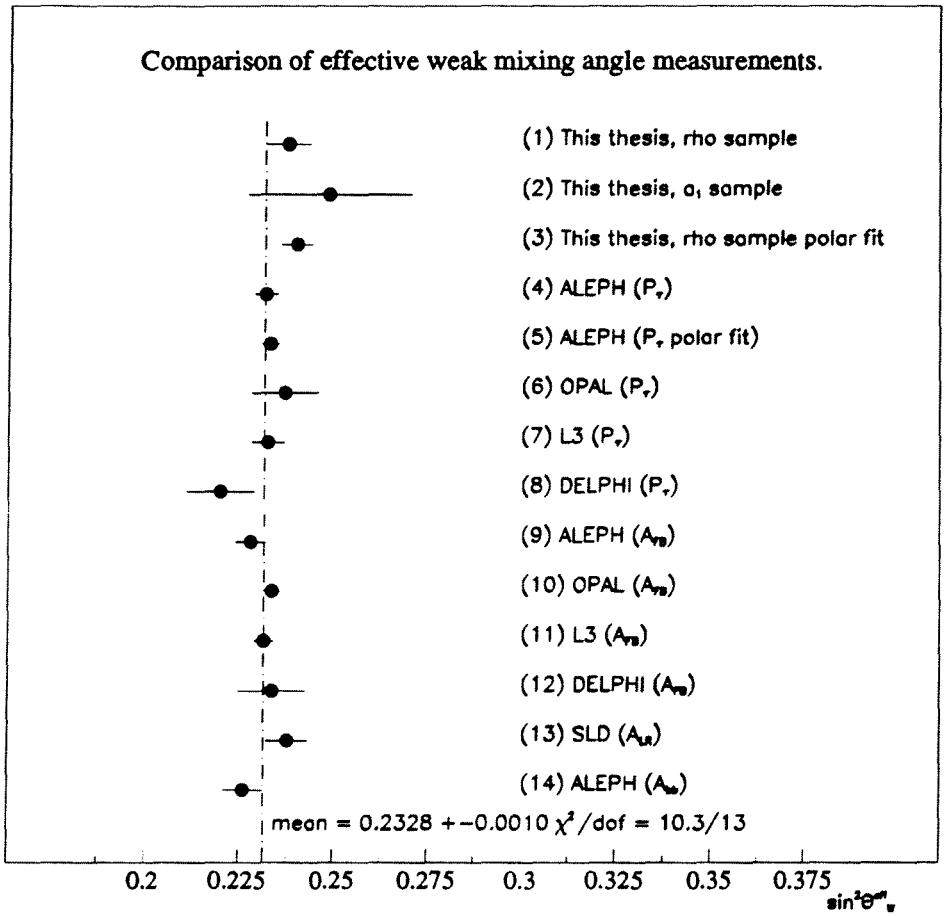

Figure 8.1: Comparison of effective weak mixing angle measurements. Each measurement is labelled with the collaboration which carried out the analysis. The measurement from which the value for $sin^2\bar{\theta}_W$ was derived is indicated in brackets, i.e. P_τ: tau polarisation, A_{FB}: forward-backward asymmetry, A_{LR}: left-right polarisation asymmetry for polarised beams, A_{bb}: $b\bar{b}$ asymmetry. The figure shows a consistency of results between those measured in this thesis and other measurements.

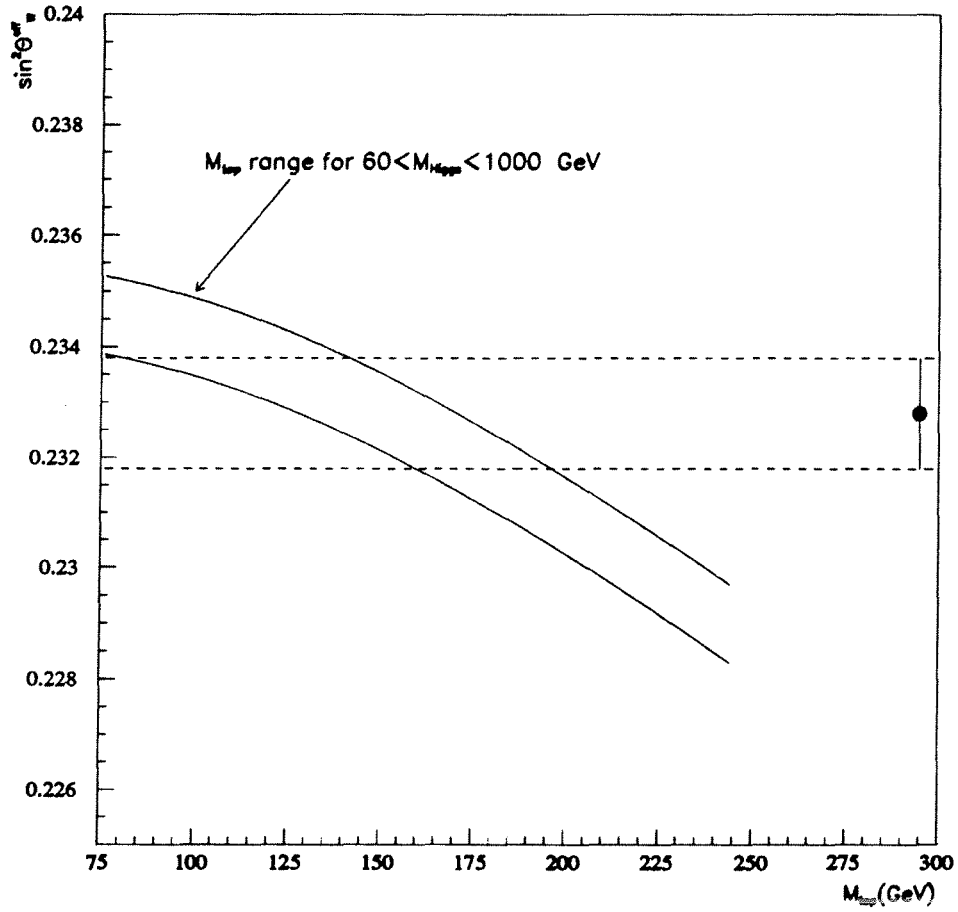

Figure 8.2: Variation of $sin^2\bar{\theta}_W$ as a function of M_{top} for M_{Higgs} in the range 60 - 1000 GeV. The data point is the weighted average value of $sin^2\bar{\theta}_W$ values shown in figure 8.1.

indicates a top quark mass in the range 80< M_{top} <190 GeV. This is consistent with the value recently determined by ALEPH [72], i.e.

$$M_{top} = 156^{+22+17}_{-25-22 Higgs}. \tag{8.4}$$

This is also in agreement with a global analysis of LEP and other precision electroweak data performed by Ellis and Fogli [75], which restricts the top quark mass to 92< M_{top} <147 GeV.

Figure 8.2 indicates how the constraint on M_{top} and M_{Higgs} will improve (in the absence of direct detection of the top quark) with a reduction in the uncertainty in $sin^2\bar{\theta}_W$. This of course will occur with the accumulation of more data.

To summarise, the measured average longitudinal polarisation of the tau lepton gives a value for the effective weak mixing angle of $sin^2\bar{\theta}_W = 0.2377 \pm 0.0060$. Since this is compatible with other measures of $sin^2\bar{\theta}_W$ it provides a good check of the Standard Electroweak Model. Also, this measurement indicates that the mass of the, as yet unseen top quark should be ~150 GeV within the Standard Model.

Appendix A

Properties of the Tau Lepton

The main properties of the tau lepton as given by the Particle Data Group are as listed in the table below.

PROPERTIES OF THE TAU LEPTON.	
mass	$1784.1\ ^{+2.7}_{-3.6}$ MeV
mean lifetime, τ	$(0.305 \pm 0.006)\times10^{-12}$ s
$c\tau$	91.4 μm
Michel parameter, ρ	0.727 ± 0.033
BRANCHING RATIOS (%) :	
Topological one prong :	85.82 ± 0.25
$\tau^- \rightarrow \mu^- \bar{\nu}_\mu \nu_\tau$	17.58 ± 0.27
$\tau^- \rightarrow e^- \bar{\nu}_e \nu_\tau$	17.93 ± 0.26
$\tau^- \rightarrow \pi^- \nu_\tau$	11.6 ± 0.4
$\tau^- \rightarrow \pi^- \pi^0 \nu_\tau$	24.0 ± 0.6
$\tau^- \rightarrow h^- 2\pi^0 \nu_\tau$	10.3 ± 0.9
$\tau^- \rightarrow h^- \geq 3\pi^0 \nu_\tau$	2.7 ± 0.9
Topological three prong :	14.06 ± 0.25
$\tau^- \rightarrow h^- h^- h^+ \nu_\tau$	8.4 ± 0.4
$\tau^- \rightarrow \pi^- \pi^- \pi^+ \nu_\tau$	5.6 ± 0.7
$\tau^- \rightarrow \pi^- \rho^0 \nu_\tau$	5.4 ± 1.7
$\tau^- \rightarrow \pi^- \pi^- \pi^+$ non-$\rho(770)^0 \nu_\tau$	<1.4 CL=95%
Topological five prong :	$(1.11 \pm 0.24)\times10^{-3}$
Topological seven prong :	$<1.9\times10^{-4}$ CL=90%

Table A.1: Tau Lepton particle properties.

References

[1] 'Introduction to High Energy Physics', D.H.Perkins, Addison-Wesley Publishing Co. Inc., third edition, (1987).

[2] 'The Feynman Lectures on Physics, vol. II', R.P.Feynman, Addison-Wesley Publishing Co. Inc., (1964).

[3] 'Quarks and Leptons: an Introductory Course in Modern Particle Physics', F.Halzen and A.D.Martin, John Wiley and Sons, (1984).

[4] 'Quantum Field Theory', F.Mandl and G.Shaw, John Wiley and Sons, (1984).

[5] 'E.Fermi, Z.Phys.88, 161 (1934).

[6] C.N.Yang and R.L.Mills, Phys. Rev. 96 (1954) 191;
R.Shaw, Cambridge Ph.D. thesis (1954) unpublished.

[7] 'Proceedings of the school for Young High Energy Physicists', RAL-91-036.

[8] 'Review of Particle Properties', Phys. Rev. D45, part 2, (1992).

[9] 'Large Electron Positron Storage Ring Technical Notebook ', CERN Publication, November 1989.

[10] 'The Aleph Handbook', ed. W.Blum, (The Aleph Collaboration), ALEPH 89-77, NOTE 89-03;
'ALEPH: A detector for electron-positron annihilations at LEP', D¿Decamp et al., (The Aleph Collaboration), Nucl. Instr. Methods A294, 121 (1990) .
'ALEPH in numbers', D.Schlatter and G.Redlinger, ALEPH internal report (1990).
'ALEPH in 1991', R.Settles, ALEPH 92-68, PHYSIC 92-59 (1992).

[11] 'Electroweak Parameters of the Z^0 resonance and the Standard Model', The LEP Collaborations: ALEPH, DELPHI, L3 and OPAL, Phys. Lett. B276 (1992) 247-253.

[12] M.L.Perl et al., (MARK I), Phys. Rev. Lett. 35 (1975) 1489.

[13] 'Measurement of the Mass of the τ Lepton', SLAC- PUB-5870, BEPC-EP-92-01, (1992).

[14] 'Calculation of exclusive decay modes of the tau', F.J. Gilman and S.H.Rhie, Phys. Rev. D31 no.5 (1984) 1066.

[15] 'Hadronic τ decay, pion radiative decay, and pion polarizability', T.N.Truong, Phys. Rev. D30 no.7 (1984) 1509.

[16] 'τ Decays: The Solution to a Longstanding Problem?' , C.Kiesling (Max Planck Institute), MPI-PAE/Exp.E1.206 (1989).

[17] 'Exclusive τ Decays with the CELLO Detector at PETRA', H.J.Behrend et al., (The CELLO Collaboration), Z. Phys. C- Particles and Fields 46, 537 (1990).

[18] 'Measurement of exclusive one-prong and inclusive three prong branching ratios of the τ lepton', H.Albrecht et al., (The ARGUS Collaboration), Z. Phys. C-Particles and Fields 53. 367-374 (1992) .

[19] 'The Physics of the τ Lepton', B.C.Barish and R. Stroynowski, Phys. Rep. 157, no.1 (1988) 1-62, North-Holland, Amsterdam.

[20] H.Albrecht et al., (The ARGUS Collaboration), Phys. Lett. B202 (1988) 149.

[21] T.Kinoshita and A.Sirlin, Phys. Rev. 107 (1957) 593; 108 (1957) 844;
C.Bouchiat and L.Michel, Phys. Rev. 106 (1957) 170.

[22] W.Bacino et al., (DELCO), Phys. Rev. Lett. 42 (1979) 749;
S.Behrends et al., (CLEO), Phys. Rev. D32 (1985) 2468;
W.T.Ford et al., (MAC), Phys. Rev. D36 (1987) 1971;

H.Janssen et al., (CRYSTAL BALL), Phys. Lett. B228 (1989) 273;
H.Albrecht et al., (ARGUS), Phys. Lett. B246 (1990) 278.

[23] 'The Tau Polarisation Measurement', S.Jadach and Z.Was, CERN 89-08 Yellow Report 'Z Physics at LEP1, volume 1', (1989).

[24] 'Electroweak Radiative Corrections for Z^0 Physics' , M.Consoli and W.Hollik, CERN 89-08 Yellow Report 'Z Physics at LEP1, volume 1', (1989).
'Δr, or the Relation Between the Electroweak Couplings and the Weak Vector Bosons', C.Burgers and F.Jegerlehner, CERN 89-08 Yellow Report 'Z Physics at LEP1, volume 1', (1989).

[25] 'Radiative Corrections to the Z^0 Resonance', J.P. Alexander, G.Bonvicini, P.J.Drell and R.Frey, Phys. Rev. D37, 56 (1988);
'Monte Carlos for Electroweak Physics', R.Kleiss, CERN 89-08 Yellow Report 'Z Physics at LEP1, volume 1', (1989).

[26] M.Nuttall, Ph.D Thesis, Lancaster University (1992), RALT-132.

[27] 'First Observation of Transverse Beam Polarisation in LEP', The LEP Polarisation Collaboration, Phys. Lett. B270 (1991), 97.

[28] 'Improved Measurements of Electroweak Parameters from Z Decays into Fermions', D.Decamp et al., (The Aleph Collaboration), Z. Phys. C-Particles and Fields 53, 1-20 (1992).

[29] 'TPC 90, A Test Model for the ALeph Time Projection Chamber', S.R.Amendolia et al., Nucl. Instr. Methods A252 (1986) 392.

[30] 'The Field Mapping System for the Aleph and Delphi Magnets', D.Lehm et al., ALEPH 87-55, NOTE 87-10 (1987);
'The Field in the Aleph Magnet', L.Bauerdick et al., ALEPH 88-034, NOTE 88-005 (1988).

[31] 'The BOS System Dynamic Memory Management, second updated printing, FORTRAN77 version', V.Blobel, DESY Internal Report, DESY R1-88 -01 (1988).

[32] 'JULIA User's and Programmer's Guide', J.Knobloch, ALEPH 90-115, SOFTWR 90-011 (1990).

[33] 'ALPHA- ALEPH Physics Analysis Package User's Guide', H. Albrecht and E.Blucher, ALEPH 91-127, SOFTWR 91-004 (1991).

[34] 'GEANT3 User Guide', R.Brun et al., CERN/DD 84-1, CERN software documentation, September 1987.

[35] T.Sjöstrad, Comp. Phys. Comm. 27, 243 (1982);
T.Sjöstrad, Comp. Phys. Comm. 28, 229 (1983);
M.Bengstsson and T.Sjöstrad, Comp. Phys. Comm. 43, 367 (1987).

[36] 'Physics at HERA, volume 3, Monte Carlo generators', ed. W.Buchmüller and G.Ingelman, DESY Laboratories (1992).

[37] 'KORALB Version 2.1. An Upgrade with the TAUOLA Library of τ Decays', S.Jadach and Z.Was, Comp. Phys. Comm. 64, 267 (1991);
'TAUOLA - a Library of Monte Carlo Programs to Simulate Decays of Polarised τ Leptons', S.Jadach, J.H.Kühn and Z.Was, Comp. Phys. Comm. 64, 275 (1991).

[38] Monte Carlo Group, 'Z Physics at LEP1, volume 3: Event Generators and Software', CERN 89-08 Yellow Report, (1989).

[39] 'Decay Correlations of Heavy Leptons in $e^+e^- \rightarrow l^+l^-$', Y.S.Tsai, Phys. Rev. D4, (1971) 2821.

[40] 'τ Polarisation Measurements at LEP and SLC', K. Hagiwara, A.D.Martin and D.Zeppenfeld, Phys. Lett. B235, 198(1990).

[41] 'Tau Physics', A.Pich, CERN-TH.6237/91 (1991).

[42] 'Tau decays as Polarisation Analysers', A.Rougé, Workshop on Tau Lepton Physics, Orsay, 24-27 September 1990.

[43] J.E.Augustin and G.Goggi, Proceedings of the LEP Summer Study 1978, CERN report 79-01, volume 2, 483 (1979).

[44] 'τ Polarisation Measurement in the $\tau \rightarrow \rho\nu$ Decay Mode', A.Rougé, ALEPH 88-15 (1988) .

[45] 'Systematics of Angular and Polarisation Distributions in Three-Body Decays', S.M.Berman and M.Jacob, Phys. Rev. 139 4B (1965) 1023.

[46] 'Heavy flavour production in Z decays', D.Decamp et al., (The ALEPH Collaboration), Phys. Lett. B244 no.3,4 (1990) 561.

[47] 'τ Decays to pions', J.H.Kühn and A.Santamaria, Z. Phys. C-Particles and Fields 48, 445-452 (1990).

[48] 'The a_1 in τ decay', N.Isgur, C.Morningstar and C.Reader, Phys. Rev. D39 no.5 (1989) 1357.

[49] 'Measurements of Tau Decays to Three Pions', H.R.Band et al., (The MAC Collaboration), Phys. Lett. B2 (1987) 297.

[50] 'Measurements of Tau Decays into Three Charged Pions', H. Albrecht et al., (The ARGUS Collaboration), Z. Phys. C-Particles and Fields 33, 7-12 (1986).

[51] 'Measuring Hadronic Currents and Weak Coupling Constants in $\tau \rightarrow \nu 3\pi$', M.Feindt, DESY 90-036, (1990).

[52] 'Measurement of the branching ratios for the decays $\tau \rightarrow h\pi^0\nu$ and $\tau \rightarrow h\pi^0\pi^0\nu$', D.Antreasyan et al., (The CRYSTAL BALL collaboration), SLAC-PUB-5403, DESY 91-001, HEN-334 (1990).

[53] 'Measurement of the Decay $\tau^- \rightarrow \rho^-\nu_\tau$', H.Albrecht et al., (The ARGUS Collaboration), DESY 92-082 (1992).

[54] 'Measurement of Tau Branching Ratios', D.Decamp et al., (The ALEPH Collaboration), CERN/91-186 (1991).

[55] 'MINUIT Function Analysis Minimisation and Error Analysis', F.James and M.Roos, CERN library documentation, December 1989 .

[56] D.Decamp et al., The ALEPH Collaboration, Z. Phys. C53, 1 (1991).
D.Decamp et al., The ALEPH Collaboration, Phys. Lett. B265, 430 (1991).

[57] 'An Update of Tau Polarisation in the Pion Channel', S.W. Snow, ALEPH 92-13, PHYSIC 92-11, (1992).

[58] 'Electroweak Parameters from Z Decays for the Dallas Conference', (The ALEPH Collaboration), ALEPH 92-124, PHYSIC 92-113, (1992).

[59] K.Abe et al., Phys. Rev. Lett. 62 (1989) 1709;
D.Geirgat et al., (The CHARM II Collaboration), Phys. Lett. B259 (1991) 499;
J.Dorenbosch et al., (The CHARM Collaboration), Z. Phys. C-Particles and Fields 41 (1989) 567;
R.C.Allen et al., Phys. Rev. Lett. 64 (1990) 1330.

[60] 'Measurement of the Tau Polarisation at the Z Resonance' , D.Decamp et al., The ALEPH Collaboration, CERN-PPE/93-39 (1993) (submitted to Z.Phys.C).

[61] 'Particle Identification for Tau Physics in ALEPH Using a Neural Network', J.Conway, J.Harton, M.Schmitt and M.Walsh, (University of Wisconsin), ALEPH 92-56, PHYSIC 92-49 (1992).

[62] 'Measurement of the Tau Lepton Lifetime', D.Decamp et al. , (The ALEPH Collaboration), CERN-PPE/92-003 (1992).

[63] 'Limit for the Tau Neutrino Mass using $\tau \rightarrow \pi^-\pi^-\pi^+\pi^0\nu_\tau$', U.Stiegler (I.N.F.N. Sezione di Trieste, Italy), ALEPH 91-69, PHYSIC 91-62 (1991).

[64] 'Upper limit on the Tau Neutrino Mass from $\tau^\pm \rightarrow 5\pi^\pm(\pi^0)\nu_\tau$ Decays', J.Raab and L.A.T.Bauerdick, ALEPH 91-121, PHYSIC 91-108, (1991).

[65] 'A measurement of τ polarisation in Z^0 decays', The L3 Collaboration, CERN-PPE/92-132 (1992).
Adeva et al., (The L3 Collaboration), Phys. Lett. B294, 466 (1992).

[66] Aarnio et al., (The Delphi Collaboration), Z. Phys. C-Particles and Fields C55, 555 (1992).
'A study of the decays of the τ lepton produced on the Z^0 resonance at LEP', Aarnio et al., (The Delphi Collaboration) , CERN-PPE 92/60 (1992).

[67] 'Measurement of the branching ratios and polarisation from τ decays at LEP', Alexander et al., (The OPAL Collaboration), Phys. Lett. B266, 201 (1991).

[68] 'Measurement of electroweak parameters from hadronic and leptonic decays of the Z^0', Adeva et al., (The L3 Collaboration), Z. Phys. C-Particles and Fields 51, (1991) 179.

[69] 'Determination of the Z resonance parameters and couplings from its hadronic decays', Aarnio et al., (The Delphi Collaboration), Nucl. Phys. B367, 511, (1991).

[70] 'Measurement of the Z^0 line shape parameters and the electroweak couplings of charged leptons', Alexander et al., (The OPAL Collaboration), Z. Phys. C-Particles and Fields 52, (1991) 175.

[71] 'First Measurement of the left-right Z Cross-section Asymmetry in polarised e^+e^- collisons at the SLC.' (The SLD Collaboration), SLAC-PUB-6034 (1993).

[72] 'Update of Electroweak Parameters from Z Decays', D.Buskulic et al., (The ALEPH Collaboration) CERN-PPE/93-40 (1993) (submitted to Z.Phys.C).

[73] 'LEP Physics: A Review', Talk given at the 1993 Institute of Physics HEP Conference, Glasgow University. A.A.Carter, (QMWC University of London).

[74] 'ZFITTER: An Analytical Program for Fermion Pair Production in e^+e^- Annihilation', D.Bardin et al., CERN-TH. 6443/92 (1992).

[75] J.Ellis, G.L.Fogli and E.Lisi, Phys. Lett. B274 (1992) 456.